弾性梁を持つ歩行型圧電リニアアクチュエータの性能と操作機能に関する研究

博士学位論文

Study on the performance and operation function of walking-type piezoelectric linear actuator with compliant mechanism

2023 年 9 月

室蘭工業大学 大学院
工学研究科 博士後期課程
工学専攻 先端情報電子工学コース

YUN　HAO

指導教員
青柳 学 教授

要旨

精密位置決め分野の急速な発展に伴い，高精度、高速応答、大ストロークの特徴を持つ圧電アクチュエータへの需要が増加している。過去数十年にわたり，様々な非共振型圧電アクチュエータが登場し，バイオ技術，光学機器，マイクロ/ナノ位置決めプラットフォーム，半導体技術など，多くの産業分野で応用に成功している。しかし，既存の非共振圧電アクチュエータにはまだ限界がある。例えば，半導体製造におけるリソグラフィプロセスのモニタリングに使用される走査型電子顕微鏡（SEM）のアパーチャーの駆動など，(1）大きなストロークを伴う低速駆動，(2）逆方向に動作しない，(3）高い位置決め分解能，が要求される特定の精密位置決めアプリケーションにおいて，既存の圧電アクチュエータでは十分とは言えない。本研究の目的は，既存の圧電アクチュエータの限界を克服し，SEM の光学系におけるアパーチャープレートの駆動要件や，その他の精密位置決め分野に対応できる新しい圧電リニアアクチュエータの開発である。

まず、平行配列のデュアルステータを用いた両側駆動の歩行型圧電リニアアクチュエータを提案した。単一ステータの駆動脚の動作原理と楕円軌道を解析した。試作・実験の結果，アクチュエータが逆方向に動作する問題があることがわかった。

次に、両側駆動の歩行型圧電リニアアクチュエータの逆方向への動作を解決するため，三角形のコンプライアンス機構を持つシンプルなステータ構造を開発した（片側駆動）。また、x 方向および y 方向のダイナミックモデルを構築し，片側駆動圧電アクチュエータの出力特性を評価した。

最後に、片側駆動圧電アクチュエータを試作し，複数の実験からシミュレーションとの比較を行った。その結果、ダイナミックモデルの実現可能性が実証された。実験結果から，アクチュエータは広い速度範囲，逆方向に動作しないステッピング，高精度な位置決めの優れた複合性能を実現した。したがって，走査型電子顕微鏡の対物レンズのアパーチャープレートの駆動の可能性が示された。

Abstract

With the rapid development of the precision positioning field, the demand for piezoelectric actuators with high accuracy, quick response, and large stroke is increasing. Various non-resonant piezoelectric actuators have emerged in recent decades and have been applied successfully in many industrial fields, such as biological technology, optical instruments, micro/nano positioning platforms, and semiconductor technologies. However, existing non-resonant piezoelectric actuators still have limitations. They cannot be used in some specific precision positioning applications requiring (1) a low speed with a large stroke, (2) no backward motion, and (3) high positioning resolution, such as the driving of the aperture of a scanning electron microscope (SEM) used to monitor lithography process in semiconductor manufacturing. This research aims to develop a new type of piezoelectric linear actuator to overcome the limitations of the existing piezoelectric actuators and meet the driving requirements of the aperture plate in the optical system of SEM and other precision positioning fields.

First, a dual-side drive walking-type piezoelectric linear actuator with the parallel-arrangement dual stator was proposed. The operating principles and elliptical trajectory of the driving feet of a single-stator design were analyzed. A prototype was fabricated for the experimental evaluation; the results indicate that the actuator has a problem with backward motion.

Then, to solve the backward motion of the dual-side drive walking-type piezoelectric linear actuator, a simple stator structure with triangular-compliant mechanisms was further developed (single-side drive). Dynamic models in the *x*- and *y*-directions were established to evaluate the output characteristics of the single-side drive piezoelectric actuator.

Finally, a prototype of the single-side drive piezoelectric actuator was manufactured, and a series of experiments were carried out for comparison with simulation results. As a result, the feasibility of the dynamic models was verified. The experimental results indicate that the actuator realizes superior multiple performances of a wide range of velocity, stepping without backward motion, and high-precision positioning. Therefore, the possibility of driving the objective lens aperture plate in scanning electron microscopes was implied.

Contents

1. Introduction

1.1 Research background and significance

Semiconductor manufacturing technology is the foundation of the modern electronic industry, and its development plays a crucial role in driving the advancement of electronic and information technology [1]. With the continuous development of semiconductor materials and process technology, the manufacturing process of semiconductor devices is constantly updated and improved, resulting in significant improvements in performance, cost, and reliability of semiconductor devices, while photolithography is a crucial process in semiconductor manufacturing that is used to create tiny structures on the surface of a semiconductor chip, such as transistors, capacitors, and interconnects [2]. To improve the quality and performance of photolithography products, a Scanning Electron Microscope (SEM) is commonly used to monitor the photolithography process, such as pattern inspection and quality control, monitoring of the etching and cleaning process, and so on.

The schematic diagram of the SEM and the aperture prototype is shown in Fig. 1-1. In the optical system of SEM, the aperture plate plays an important role as an optical element. It is a metal plate with apertures of different sizes, usually located between the condenser lens and the objective lens in the lens system. By driving the aperture plate to position apertures of various sizes in the path of the electron beam, the angle and size of the electron beam can be constrained, thereby adjusting the resolution and depth of imaging. The driving of the aperture plate often needs to meet the following specific driving requirements: (1) Low speed with a large stroke, (2) High-precision positioning, (3) stepping without backward motion, (4) Less wear.

In recent years, with rapid development in precision positioning and driving fields, piezoelectric actuators have attracted many researchers due to their merits of high accuracy, quick response, large stroke, and no magnetic interference [3-6]. They have been widely used in precision positioning and driving fields, such as semiconductor manufacturing technology, biological technology [7,8], optical instruments [9], micro/nano manipulation [10-12], and ultra-precision machining [13]. Thus, piezoelectric actuators can also be expected to be used to drive aperture plates in SEM. However, there are some problems with existing piezoelectric actuators, such as heating and wear problems, fallback phenomenon, complex control systems, and so on that prevent them from being used for aperture driving. Therefore, piezoelectric actuators still need to be improved.

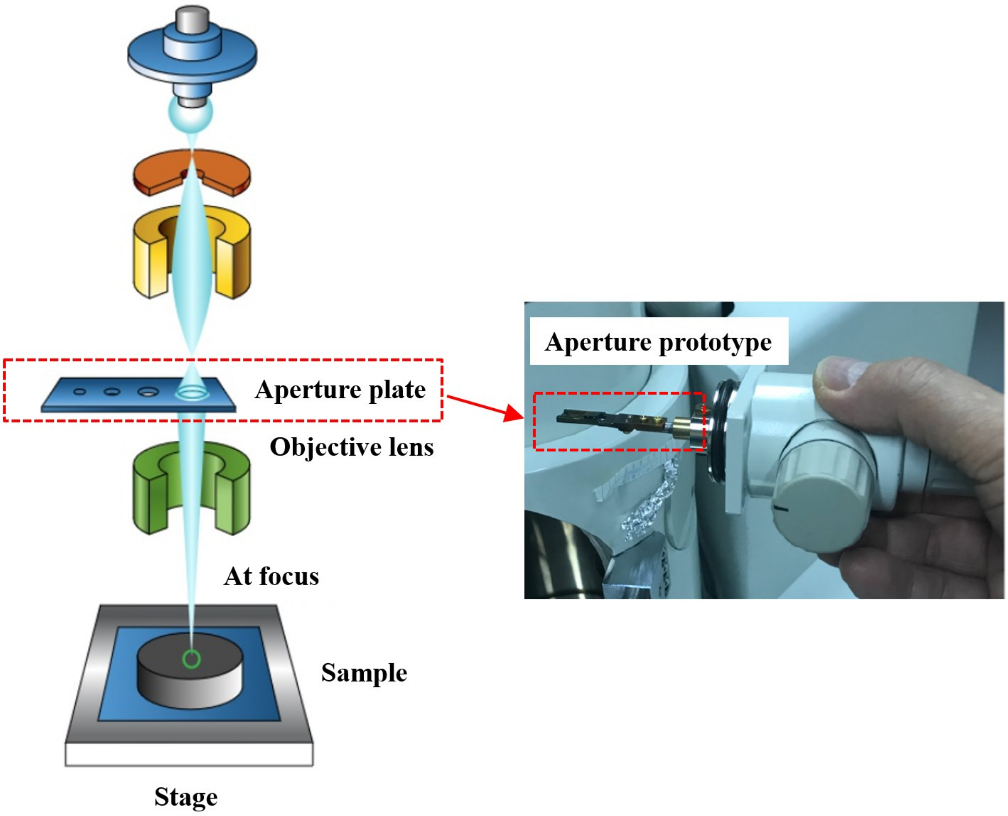

Fig. 1-1. Schematic diagram of the SEM and the aperture prototype.

1.2 Research status of piezoelectric actuator

A piezoelectric actuator is a driving device that converts electrical energy into mechanical energy using the inverse piezoelectric effect of piezoelectric materials [14-19]. The inverse piezoelectric effect is the phenomenon where a piezoelectric ceramic can generate periodic micro-vibrations when an AC voltage is applied. Piezoelectric actuators utilize a designed mechanical structure to convert this micro-vibration into macroscopic linear or rotational motion. Piezoelectric actuators can be classified as resonant and non-resonant types based on different vibration conditions.

1.2.1 Resonant-type piezoelectric actuators

Resonant-type piezoelectric actuators are also known as ultrasonic motors. The working principle of the ultrasonic motor is that the stator can generate elliptical movement through modal coupling at the ultrasonic resonant frequency, and when the rotor contacts the slider by a preload, a large stroke motion will be achieved relying on friction force. Resonant piezoelectric actuators are mainly divided into the traveling wave motor (TWM) and the standing wave motor (SWM).

Japanese scholar Sashida first proposed a disk-type rotary TWM in 1982, as shown in Fig .1-2 (a). This motor makes use of the fact that when a traveling wave propagates along a finite elastic body, the surface particles perform an elliptical motion [20]. It thus spurred many proposals on the use of various modes of vibrations, e.g. longitudinal, flexural or torsional, to obtain an elliptical motion. Dong et al. proposed a rotary TWM with a vibrating rotor and stator [21], as shown in Fig. 1-2(b). Axial bending modes with nine wavelengths of the stator and rotor were generated with the piezoelectric plates bonded on the metal disk, and the motor achieved a speed of 30 rpm and a torque of 0.75 N·m. Chen et al. proposed a rotary TWM utilizing a radial bending mode of a thick ring [22], as shown in Fig. 1-2(c). PZT stacks and block springs are nested alternately into 40 slots cut into the ring's outer surface to generate a traveling wave. The motor achieves maximum speed and torque of 146 r/min and 1.0 N·m, respectively.

A traveling-wave linear motor was first proposed by Sashida at the same time as the rotary motor [23], as shown in Fig. 1-3(a). An 8 mm diameter brass beam and two ultrasonic transducers were used. The two transducers were attached to both ends in order to excite a flexural wave with one transducer and to receive the wave with the other one. In 1985, Kurosawa et al. developed a second prototype of linear TWM [24], as shown in Fig .1-3(b). The object of the prototype was high speed and high power; the target speed was 1m/s. Murai et al. developed a hollow cylindrical linear TWM without an extra linear guide [25] shown in Fig. 1-3(c), the stator consists of a metal pipe and PZT tubes installed at both ends of the metal pipe. The measured results indicated that the average speed of the 8.5g slider was 7.9 mm/s.

In 1992, Kurosawa et al. started to study linear traveling surface acoustic wave ultrasonic motor (SAW USM) and made their first motor with two degrees of freedom [26], as shown in Fig. 1-4. Its stator was made of crystal $LiNbO_3$. The planar motion of the slider was obtained by two orthogonal SAWs excited by IDT. However, due to the high process requirements of this ultrasonic motor, it has not yet been applied.

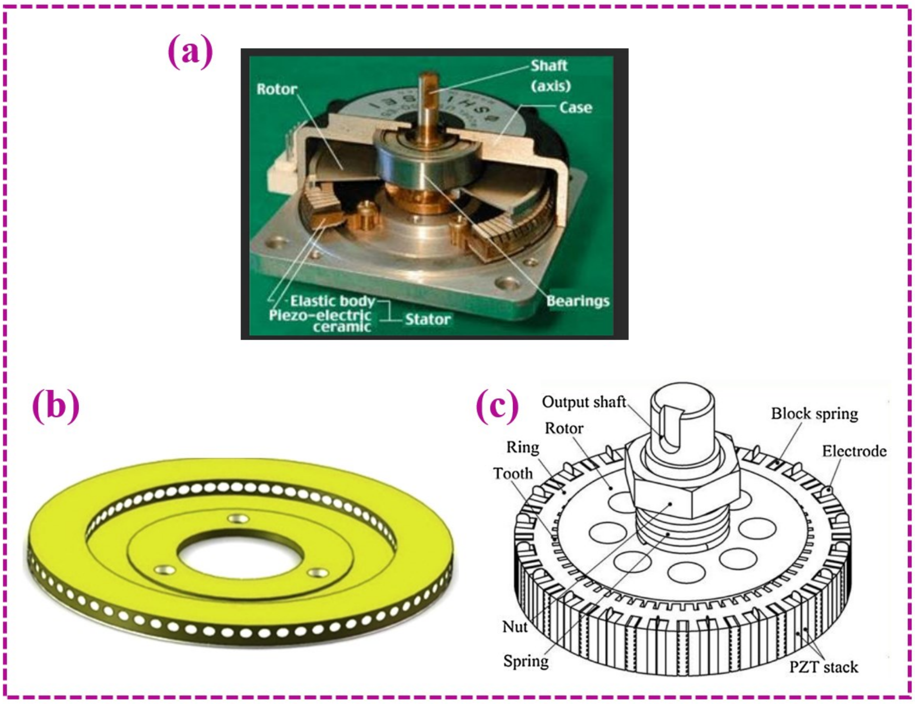

Fig. 1-2. Rotary traveling wave motors. (a) TWM by Sashida [20], (b) TWM by Dong et al. [21], and (c) TWM by Chen et al. [22].

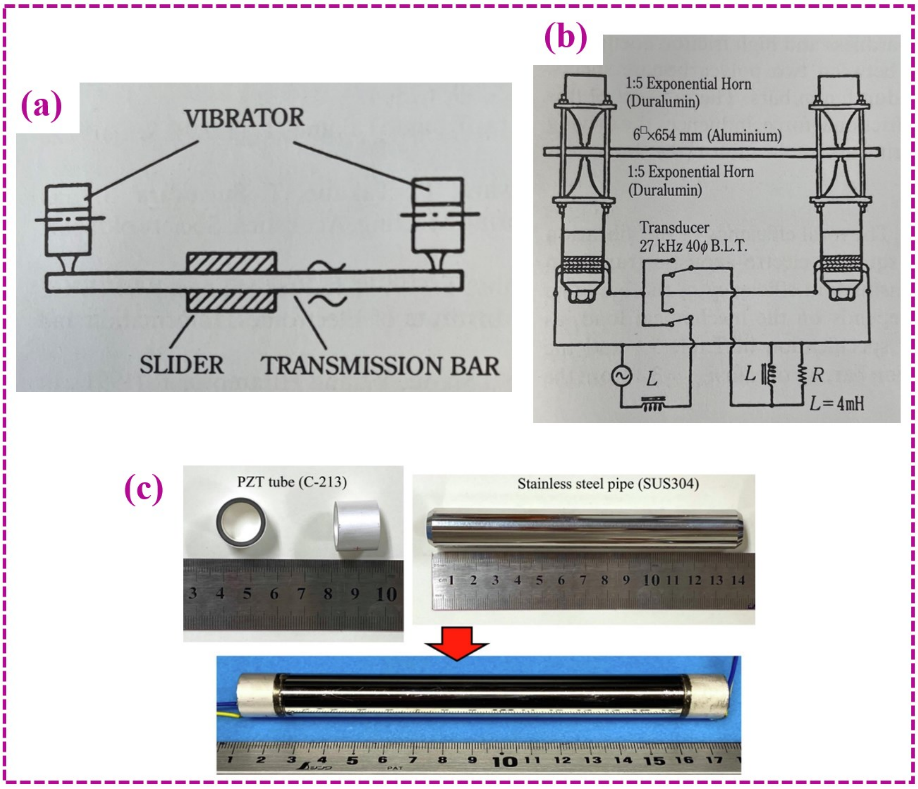

Fig. 1-3. Linear traveling wave motors. (a) TWM by Sashida [23], (b) TWM by Kurosawa et al. [24], and (c) TWM by Murai et al. [25].

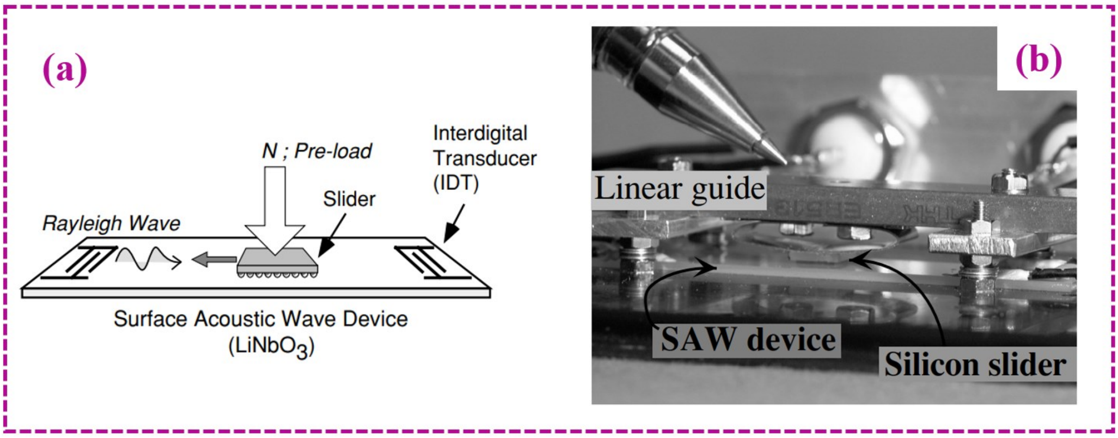

Fig. 1-4. SAW USM by Kurosawa et al. [26]. (a) Working principle and (b) prototype.

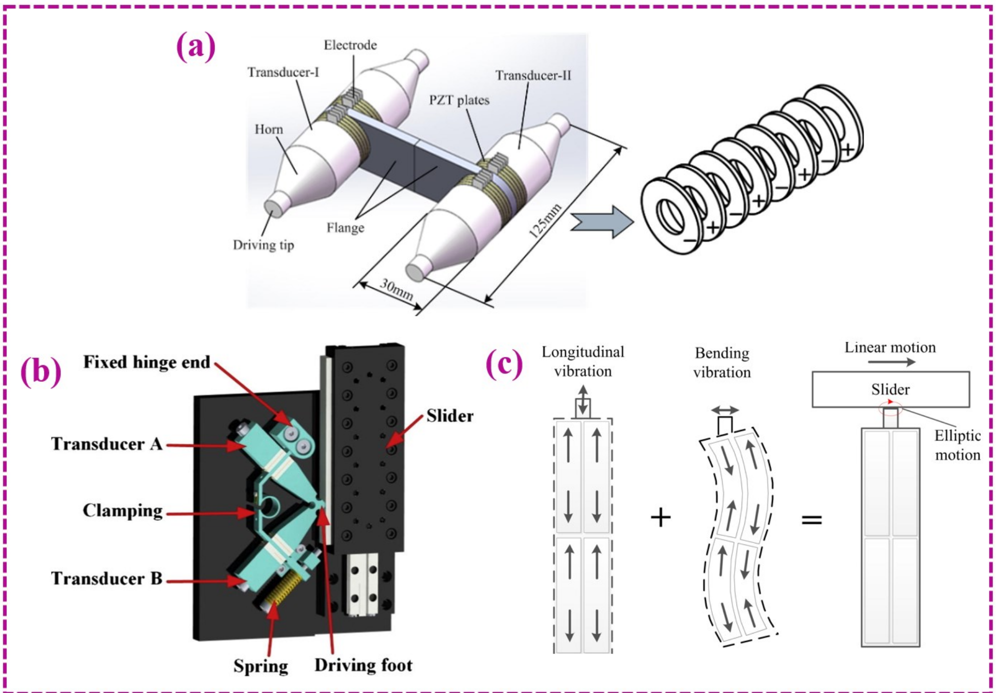

Fig. 1-5. Standing wave motors. (a) SWM by Liu et al. [28], (b) SWM by Jian et al. [29], and (c) SWM by Li et al. [30].

As for the SWM, the elliptical motion of the driving foot is obtained by exciting a standing wave in the stator. Tomikawa et al. developed a linear SWM using a double-mode piezoelectric ceramic vibrator in 1992 [27]; rectangular plate vibrator of the first longitudinal and second bending modes is utilized. Liu et al. proposed a bi-directional SWM based on two sandwich-type transducers [28]. The maximum speed and thrust are

244 mm/s and 9.8 N, respectively, as shown in Fig. 1-5(a). Fig. 1-5(b) described a V-type linear SWM with a no-load speed of 1.4 m/s and a maximal thrust of 43 N for a gravimeter developed by Jian et al. [29]. Li et al. combined the longitudinal and bending modes of the stator to drive the slider and proposed a novel friction model [30], as shown in Fig. 1-5(c).

It can be seen that the resonant piezoelectric actuators can achieve high-speed motion and large thrust.

1.2.2 Non-resonant type piezoelectric actuators

Different from resonant type piezoelectric actuators, non-resonant piezoelectric actuators generally adopt a piezoelectric stack as the main driving element and can work at the non-resonant frequency, which is conducive to stable operation. With different operating principles, non-resonant piezoelectric actuators can be divided into direct drive, inchworm, stick-slip, and walking types.

Direct-drive piezoelectric actuators mainly consist of the displacement amplified mechanism and several piezoelectric stacks. These piezoelectric stacks are embedded in the compliant mechanism to drive the mobile stage directly by means of the deformation of the compliant mechanism. For instance, Ling et al. presented a piezo-actuated parallel millimeter-range XY monolithic mechanism based on a hybrid rhombus-lever multistage displacement amplifier [31], as shown in Fig. 1-6(a). A motion range of 1.2 mm × 1.2 mm at a resonant frequency of 128 Hz was achieved. Tang et al. designed a fully decoupled compliant 2-DOF micro/nano positioning stage with dual mode [32], as presented in Fig. 1-6(b). The prototype indicates that the workspace is around 120 × 120 μm^2, while the cross-coupling between the two axes is kept within 2%. Zhu et al. proposed a piezo-actuated XY parallel compliant mechanism by incorporating a novel Z-shaped flexure hinge into the mirror-symmetrical structure [33], as shown in Fig. 1-6(c). The output resolution of this mechanism is approximately 70 nm, and the experimental amplification ratio is about 35.68. It can be seen that direct-drive piezoelectric actuators are usually used for precision positioning platforms to realize micro-/nano scale positioning resolution.

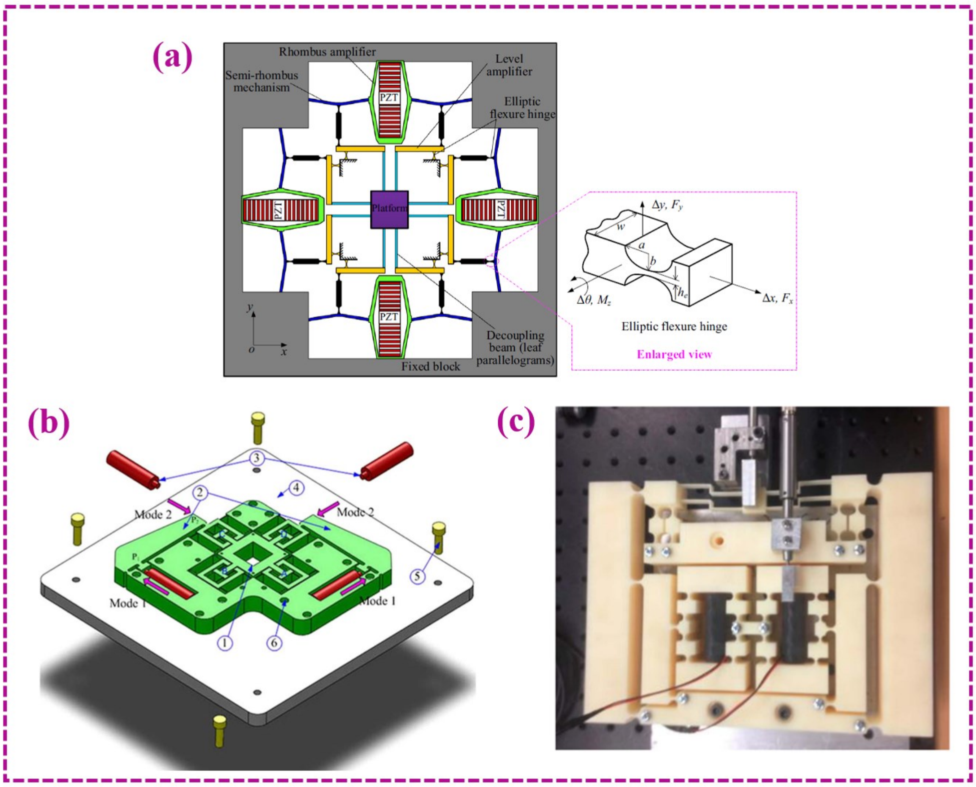

Fig. 1-6. Direct-drive piezoelectric actuators. (a) Actuator by Ling et al. [31], (b) Actuator by Tang et al. [32], and (c) Actuator by Zhu et al. [33].

The inchworm-type piezoelectric actuator is a type of mechanism that mimics the motion of an inchworm found in nature. A typical inchworm-type piezoelectric actuator generally contains the clamping unit and feeding unit. For example, Tian et al. proposed a U-shaped inchworm-type piezoelectric actuator with a low motion coupling ratio of 4% and maximum thrust of 189.7 N [34], as shown in Fig. 1-7(a). Fig. 1-7(b) shows a piezoelectric positioning platform by means of the inchworm motion principle with a minimum stepping angle of 0.23 μrad and stepping displacement of 0.15 μm proposed by Li et al. [35]. Mohammad et al. presented a compact precision high positioner based on an inchworm-type actuator [36], as shown in Fig. 1-7(c). A minimum positioning resolution of 120 nm was achieved. It can be obtained that the inchworm-type actuator can achieve a micro/nano-scale precision positioning over a large stroke.

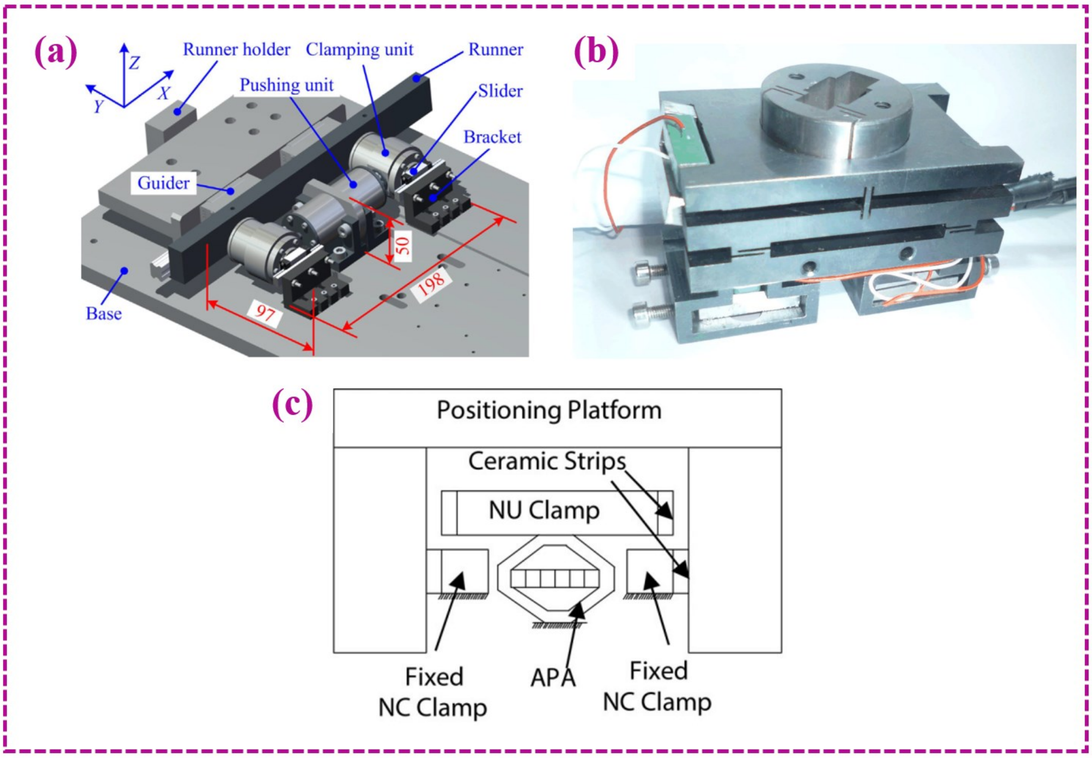

Fig. 1-7. Inchworm-type piezoelectric actuators. (a) Actuator by Tian et al. [34], (b) Actuator by Li et al. [35], and (c) Actuator by Mohammad et al. [36].

As for stick-slip type actuators, the piezoelectric stacks are excited to generate slow deformation and rapid deformation alternately by using sawtooth waveform signal with different duty ratios so that the slider can be driven to output the linear or rotary motions due to the static and sliding friction [37-41]. Up to present, various stick-slip type actuators have been proposed. Fig. 1-8(a) shows a novel stick-slip actuator based on a triangular-compliant driving mechanism proposed by Zhang et al. [42] to increase the driving force. Cheng et al. developed a trapezoid-type stick-slip piezoelectric linear actuator using a right circular flexure hinge mechanism [43], as presented in Fig. 1-8(b). This actuator could achieve maximum output velocity and load of 5.96 mm/s and 3 N. Huo et al. proposed a kind of dual-driven high precision rotary platform based on the stick-slip principle [44] shown in Fig. 1-8(c) to realize a large circular motion stroke and high loading capacity. Li et al. also proposed a stick-slip type actuator with two 'legs' to reduce the backward motion [45], as presented in Fig. 1-8(d). Thus, stick-slip type actuators can realize high accuracy, compact structure, and simple operation.

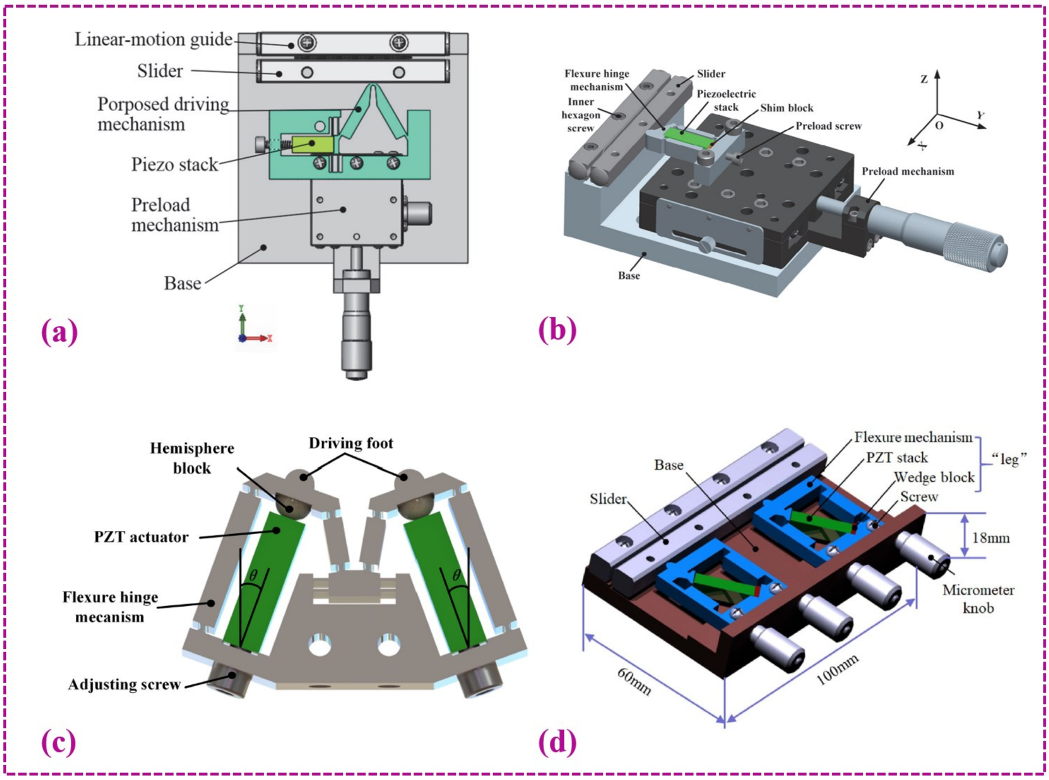

Fig. 1-8. Stick-slip type actuators. (a) Actuator by Zhang et al. [42], (b) Actuator by Cheng et al. [43], (c) Actuator by Huo et al. [44], and (d) Actuator by Li et al. [45].

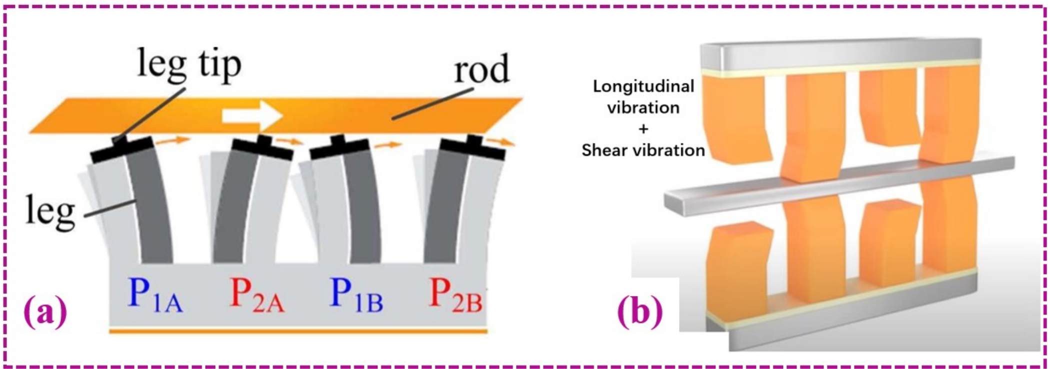

Fig. 1-9. Walking-type piezoelectric actuators. (a) Actuator by Li et al. [46] and (b) Actuator by PI company [47].

Walking-type piezoelectric actuators usually utilize multiple stators to work cooperatively to drive the slider. The operating principle is similar to human walking. In recent years, Li et al. [46] and the Physik Instrumente company [47] developed two kinds of walking piezoelectric actuators with multiple legs that use bending deformation and a combination of the longitudinal and shear deformations of piezoelectric stacks as the driving mechanism, respectively, as shown in Fig. 1-9. These two walking-type actuators can realize a sub-nanometer scale positioning resolution and a step displacement without backward motion.

1.2.3 Application of the piezoelectric actuators

Piezoelectric actuators are mainly used in precision positioning systems, biomedical engineering, precision instruments, automotive industry, aerospace technology due to their advantages of fast response, high precision, power-off self-locking, and flexible design.

Piezoelectric actuators are widely used in precision positioning platforms because of their micro/ nano-scale positioning accuracy. Figs. 1-10(a) shows a 6-DOF positioning platform developed by Physik Instrumente company [48]. The positioning resolutions in translational and rotational degrees of freedom were 80 nm and 2 μrad, respectively. New focus company proposed a 6-DOF positioning platform with positioning resolutions in translational and rotational degrees of freedom of 50 nm and 2 μrad, as shown in Fig. 1-10(b).

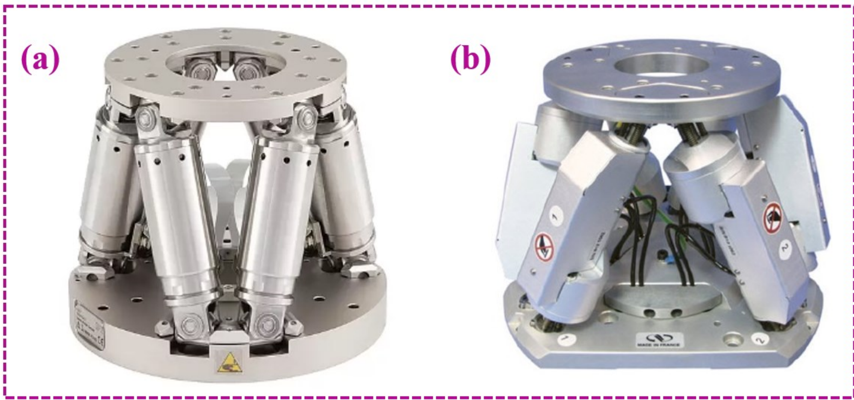

Fig. 1-10. Precision positioning platforms. (a) Proposed by PI company [48] and (b)Proposed by New focus company.

In the field of biological micro-manipulation, high positioning accuracy and high acceleration are essential for the performance of actuators. Piezoelectric actuators have become a good choice for medical equipment due to their excellent positioning accuracy and response speed. They are used by Japanese scholars for cell puncture experiments and white blood cell manipulation [49,50], as shown in Fig. 1-11.

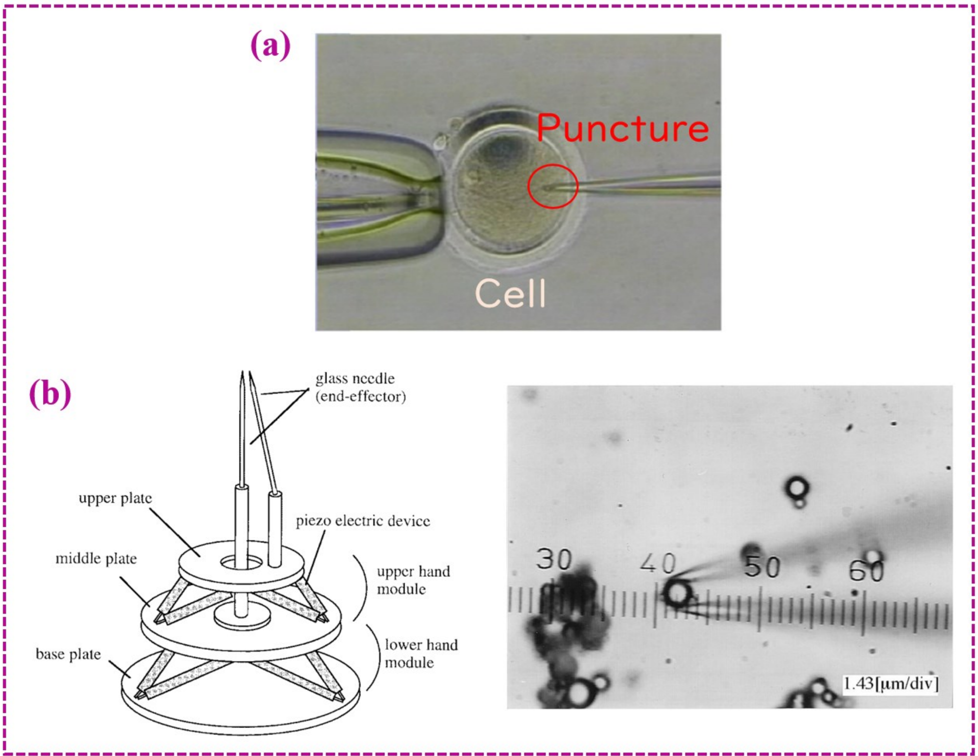

Fig. 1-11. Applications in the field of biological micro-manipulation. (a) Cell puncture experiments [49] and (b) white blood cell manipulation [50].

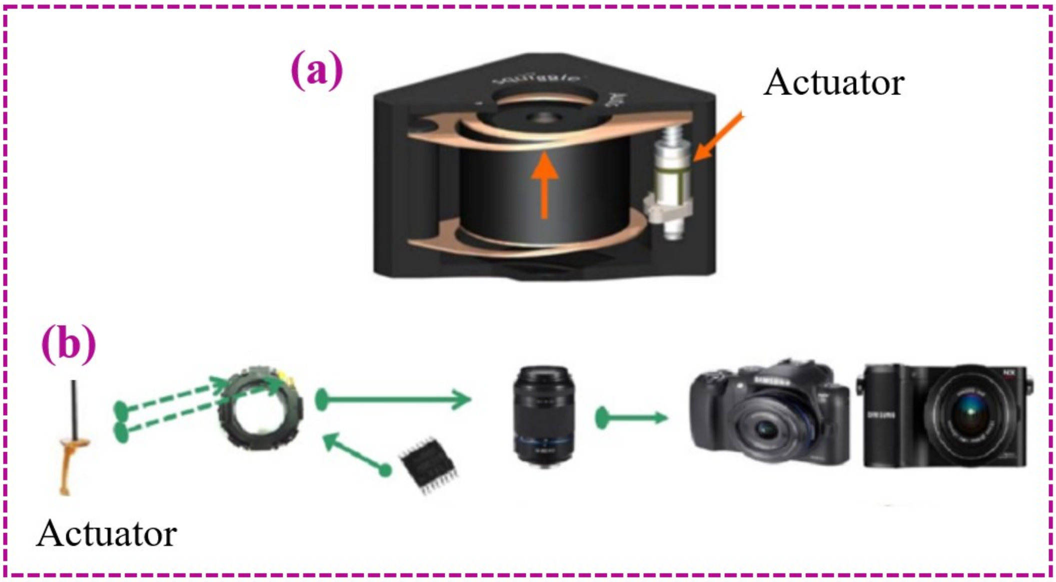

Fig. 1-12. Applications in mobile phones and cameras. (a) Focusing systems of mobile phones [51] and (b) focusing system of cameras [52].

Piezoelectric actuators can also be used for driving lenses in mobile phones and cameras. New Scale Technology company has applied miniature screw-type actuators to the focusing systems of mobile phones [51], as shown in Fig. 1-12(a). The system directly uses the lens as the moving component, making the structure more compact and responsive. Piezo-tech company has applied its developed TULA-series stick-slip piezoelectric linear actuator to the focusing system of cameras [52], as presented in Fig. 1-12(b).

Nanjing University of Aeronautics and Astronautics has applied piezoelectric actuators in the aerospace field due to their immunity to magnetic field interference and excellent performance in vacuum environments.

1.2.4 Current problems

There are still some issues with the existing piezoelectric actuators. For example, the heating and wear problems of the ultrasonic motors cannot be avoided, which makes them difficult to operate stably for extended periods [53-55]. In addition, there is a limitation in positioning resolution for ultrasonic motors [56]. As for direct-drive actuators, the walking stroke is limited in a micrometer level [57-60]. Inchworm-type actuators generally need at least three driving elements to realize the actions of clamping and feeding. This causes the structure and driving process is complex [61-64]. The backward motion and wear problem of stick-slip actuators are difficult to be avoided during the process of the slip phase [65-68].

Existing walking-type piezoelectric actuators suffer from the following disadvantage: (1) The piezoelectric stacks are usually placed perpendicular to the direction of the slider motion. Considering the preload mechanism, such a structure requires a large arrangement of space. (2) The stators are placed parallel in one line to drive the slider, it is easy to generate the wear problem. (3) This kind of actuator requires at least eight piezoelectric stacks to work cooperatively to drive the slider. The structure of the PZT with multiple inputs is complicated such as electrodes for longitudinal and shear, which results in a complex control system.

Thus, to meet the driving requirements of the aperture plate in SEM, piezoelectric actuators still need to be further improved.

1.3 Research content and objectives

As stated by the current research status, existing piezoelectric actuators have already realized good performance and have been widely applied in various precision positioning fields. However, they still cannot be used in some specific precision positioning applications requiring (1) a low speed with a large stroke, (2) less wear, (3) no backward motion, and (4) high positioning accuracy, such as the driving of the aperture of SEM used to monitor lithography process in semiconductor manufacturing [69]. Therefore, this research aims to develop a new type of piezoelectric linear actuator to overcome the limitations of the existing piezoelectric actuators and meet the driving requirements of the aperture plate in the optical system of SEM and other precision positioning fields.

This study consists of six chapters, and the main research contents of each chapter are presented in Fig. 1-13.

Chapter 1 Introduction

The concept of piezoelectric actuators, the research status of different types of piezoelectric actuators, and their applications are introduced in detail. The research background and significance, research content, and objectives are explained.

Chapter 2 Characteristics of piezoelectric ceramics and piezo-actuated principle

This chapter explains the essence of the inverse piezoelectric effect according to key properties of piezoelectric ceramics. Then, the characteristics and usage guidelines of the piezoelectric stacks are summarized. Finally, the piezo-actuated principles using the piezoelectric stack are discussed.

Chapter 3 Dual-side drive walking-type piezoelectric linear actuator with parallel-arrangement stators

A dual-side drive walking-type piezoelectric linear actuator with the parallel-arrangement dual stator is proposed. The working principle is described in detail. An actuator prototype is fabricated, and a series of experiments are tested to evaluate its output performance.

Chapter 4 Output characteristics simulation of the piezoelectric linear actuator based on dynamic models

The dynamic models in the x and y direction are established to simulate the output characteristics of the piezoelectric linear actuator. The performance of the actuator when using the single stator or the dual stator are compared by calculation.

Chapter 5 Single-side drive walking-type piezoelectric linear actuator with triangular compliant mechanism

To solve the problems of the dual-side drive actuator, a walking-type piezoelectric linear actuator with triangular-compliant mechanisms is proposed. The structure design and operating principle of the actuator are described in detail. An actuator prototype is fabricated, and a series of experiments are carried out for comparison with simulation results.

Chapter 6 Conclusion and future work

This chapter summarizes the main results achieved in this study and discusses future work.

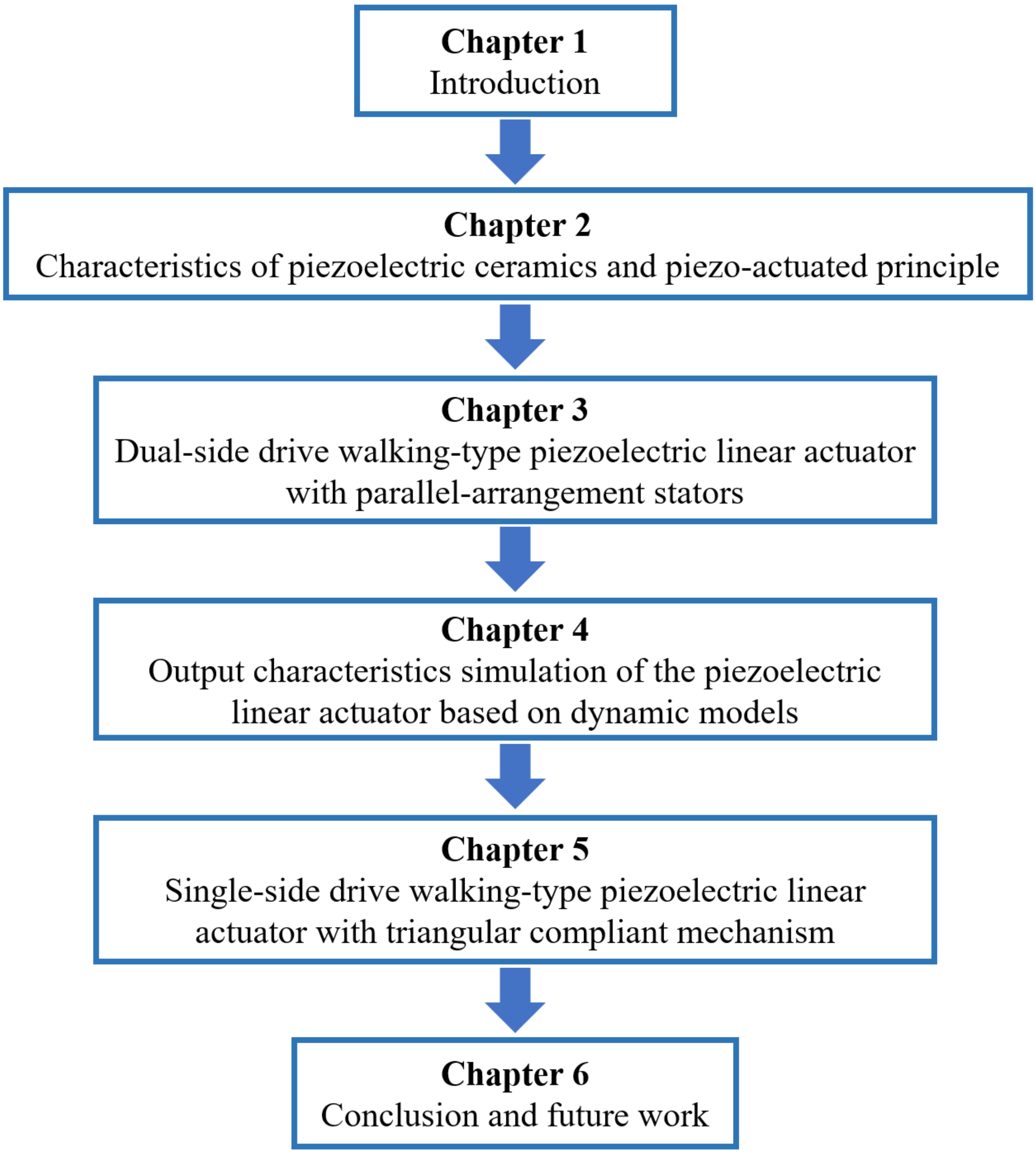

Fig. 1-13. Main research contents of this study.

2. Characteristics of piezoelectric ceramics and piezo-actuated principle

2.1 Introduction

Piezoelectric ceramics are functional materials that can convert mechanical and electrical energy into each other. When a piezoelectric ceramic material is subjected to external mechanical stress, a charge of opposite polarity appears on its two polarized surfaces, and the amount of charge is proportional to the magnitude of the external force. This phenomenon is called the direct piezoelectric effect, as shown in Fig. 2-1(a). On the contrary, when an electric field is applied to the piezoelectric ceramic in some specific directions, a mechanical strain will be induced. The deformation is approximately proportional to the applied voltage, which is called the inverse piezoelectric effect [70], as shown in Fig. 2-1(b).

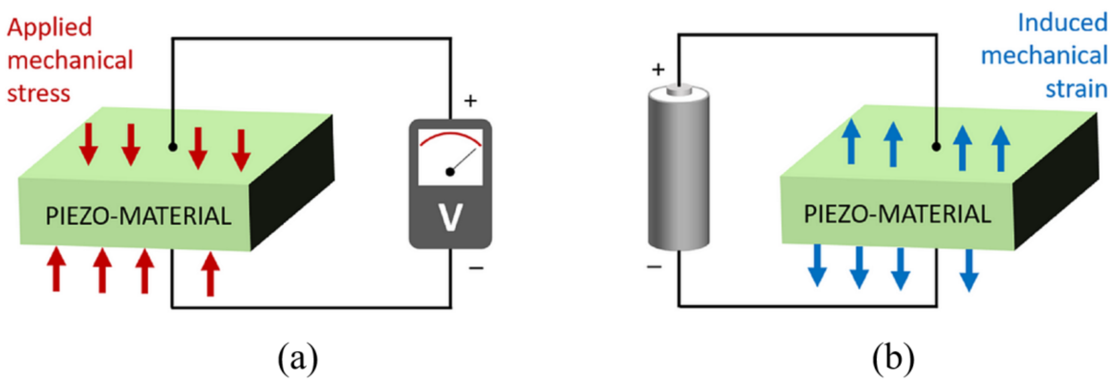

Fig. 2-1. Piezoelectric effect. (a) Direct piezoelectric effect and (b) inverse piezoelectric effect.

The piezoelectric linear actuator is a specific application of the piezoelectric effect in engineering. There are two key processes in piezoelectric actuators: one is converting the electrical energy of piezoelectric ceramics into stator elastic energy; the other is transferring the elastic energy from the stator to the slider by friction. The two processes and their energy flows are shown in Fig. 2-2.

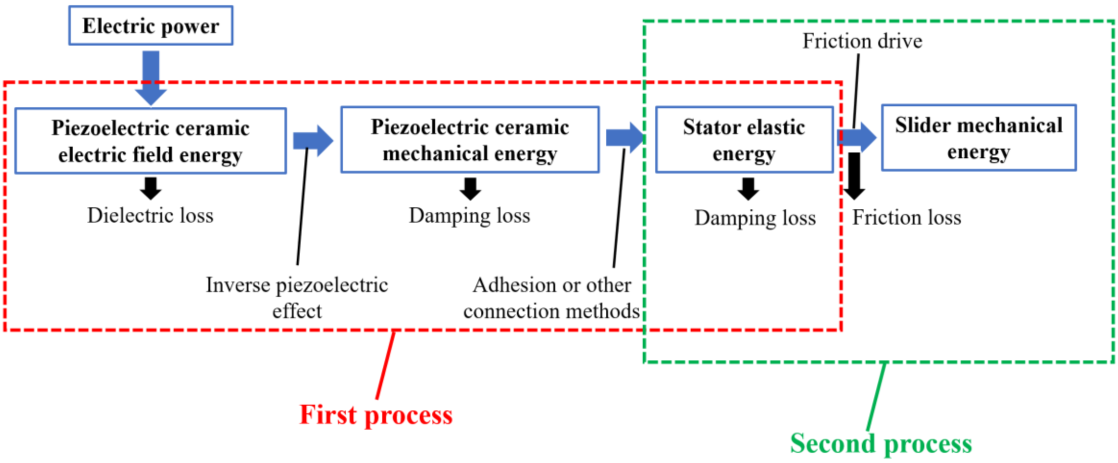

Fig. 2-2. Energy conversion and transfer principle of the piezoelectric actuator.

The first energy conversion process is realized through the inverse piezoelectric effect of piezoelectric ceramics, which involves the parameters of piezoelectric materials. The second energy transfer process is realized through the frictional effect between the stator and the slider, which involves the type of contact friction. Thus, it is necessary to summarize the performance parameters of piezoelectric components and piezo-actuated principles.

2.2 Parameters of piezoelectric ceramics

Piezoelectric ceramics are anisotropic materials that have been polarized, and the main performance parameters include dielectric, elastic, and piezoelectric properties [71]. The piezoelectric ceramic crystal coordinate system is shown in Fig. 2-3.

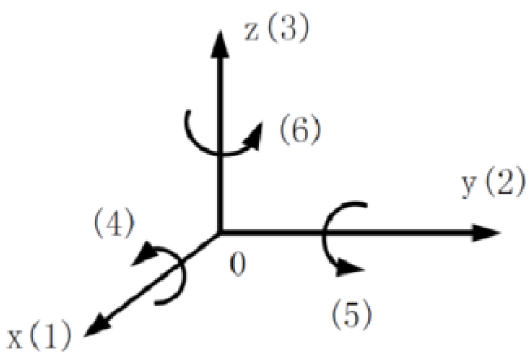

Fig. 2-3. Piezoelectric ceramic crystal coordinate system.

2.2.1 Dielectric constant

When a dielectric material is subjected to an external electric field, it produces induced charges that weaken the electric field. The ratio of the magnitude of the applied electric field to the magnitude of the resulting electric field in the dielectric material is known as the dielectric constant, which is commonly represented by the symbol ε. It reflects the material's polarization properties and insulation characteristics and can be expressed by

$$\varepsilon = \frac{Ct}{A}, \tag{2-1}$$

where C represents the electrical capacity; t denotes electrode spacing; A is defined as the area of the electrode.

Piezoelectric ceramics become anisotropic crystals after polarization, and the dielectric constant matrix of the polarized piezoelectric ceramics can be written as

$$\varepsilon = \begin{bmatrix} \varepsilon_{11} & 0 & 0 \\ 0 & \varepsilon_{11} & 0 \\ 0 & 0 & \varepsilon_{33} \end{bmatrix} \text{ (z-directional polarization)} \tag{2-2}$$

$$\varepsilon = \begin{bmatrix} \varepsilon_{11} & 0 & 0 \\ 0 & \varepsilon_{33} & 0 \\ 0 & 0 & \varepsilon_{11} \end{bmatrix} \text{ (y-directional polarization)} \tag{2-3}$$

$$\varepsilon = \begin{bmatrix} \varepsilon_{33} & 0 & 0 \\ 0 & \varepsilon_{11} & 0 \\ 0 & 0 & \varepsilon_{11} \end{bmatrix} \text{ (x-directional polarization)} \tag{2-4}$$

Due to the piezoelectric effect, the dielectric constant will vary according to the external loading conditions, and the dielectric constants in the free and loaded states are denoted as ε^T and ε^S, respectively. Thus, the polarized piezoelectric ceramics have four dielectric constants: ε_{11}^T, ε_{33}^T, ε_{11}^S, and ε_{33}^S.

2.2.2 Elasticity constant

Piezoelectric ceramic materials generally have five independent elastic stiffness coefficients and five independent elastic compliance coefficients, which are referred to as c_{11}, c_{12}, c_{13}, c_{33}, c_{44} and s_{11}, s_{12}, s_{13}, s_{33}, s_{44}. Due to the piezoelectric effect of piezoelectric ceramics, the elastic coefficients of piezoelectric ceramics vary under different electrical conditions. The constant measured under the condition of very small external resistance or zero electric field strength is called the short-circuit elastic compliance coefficient, denoted as s^E, while the constant measured under the condition of very large external resistance or zero electric displacement is called the open-circuit elastic compliance coefficient, denoted as s^D. Thus, Piezoelectric ceramics have a total of 10 elastic compliance coefficients (s_{11}^E, s_{12}^E, s_{13}^E, s_{33}^E, s_{44}^E, s_{11}^D, s_{12}^D, s_{13}^D, s_{33}^D, s_{44}^D) and 10 elastic stiffness coefficients (c_{11}^E, c_{12}^E, c_{13}^E, c_{33}^E, c_{44}^E, c_{11}^D, c_{12}^D, c_{13}^D, c_{33}^D, c_{44}^D). The compliance and stiffness matrix can be expressed as

$$s = \begin{bmatrix} 0 & s_{11} & s_{12} & s_{13} & 0 & 0 \\ 0 & s_{12} & s_{11} & s_{13} & 0 & 0 \\ 0 & s_{13} & s_{13} & s_{33} & 0 & 0 \\ 0 & 0 & 0 & s_{44} & 0 & 0 \\ 0 & 0 & 0 & 0 & s_{44} & 0 \\ 0 & 0 & 0 & 0 & 0 & 2(s_{11} - s_{12}) \end{bmatrix} \tag{2-5}$$

$$c = \begin{bmatrix} 0 & c_{11} & c_{12} & c_{13} & 0 & 0 \\ 0 & c_{12} & c_{11} & c_{13} & 0 & 0 \\ 0 & c_{13} & c_{13} & c_{33} & 0 & 0 \\ 0 & 0 & 0 & c_{44} & 0 & 0 \\ 0 & 0 & 0 & 0 & c_{44} & 0 \\ 0 & 0 & 0 & 0 & 0 & 2(c_{11} - c_{12}) \end{bmatrix} \tag{2-6}$$

2.2.3 Piezoelectric constant

Piezoelectric constant is the parameter that reflects the coupling between the elastic and dielectric properties of piezoelectric materials. Due to different independent variables or boundary conditions, there are four sets of piezoelectric constants for piezoelectric ceramics.

(1) Piezoelectric strain constant d_{ij}: The ratio of the strain change caused by the variation of electric field strength to the variation of electric field strength when the stress is constant. Or the ratio of the electrical displacement change caused by the stress change to the change of stress when the electric field is constant.

(2) Piezoelectric stress constant e_{ij}: The ratio of the stress change caused by the variation of electric field strength to the variation of electric field strength when the strain is constant. Or the ratio of the electrical displacement change caused by the change of strain to the change of strain when the electric field is constant.

(3) Piezoelectric voltage constant g_{ij}: The ratio of the change of electric field strength caused by the variation of stress to the variation of stress when the electric displacement is constant. Or the ratio of the strain change caused by the variation of the electric displacement to the variation of the electric displacement when the stress

is constant.

(4) Piezoelectric stiffness constant h_{ij}: The ratio of the stress change caused by the variation of the electric displacement to the variation of the electric displacement when the strain is constant. Or the ratio of the change of electric field strength caused by the strain change to the strain change when the electric displacement is constant.

Due to the anisotropic, four sets of piezoelectric constants after the polarization can be obtained: $d_{31} = d_{32}$, d_{33}, $d_{15} = d_{24}$; $e_{31} = e_{32}$, e_{33}, $e_{15} = e_{24}$; $g_{31} = g_{32}$, g_{33}, $g_{15} = g_{24}$; $h_{31} = h_{32}$, h_{33}, $h_{15} = h_{24}$.

The form of the piezoelectric strain constant matrix is as follows

$$d = \begin{bmatrix} 0 & 0 & d_{31} \\ 0 & 0 & d_{31} \\ 0 & 0 & d_{33} \\ 0 & d_{15} & 0 \\ d_{15} & 0 & 0 \\ 0 & 0 & 0 \end{bmatrix} \tag{2-7}$$

2.2.4 Electromechanical coupling coefficient

The electromechanical coupling coefficient K represents the coupling effect between the electrical and mechanical energy of the piezoelectric ceramic. It can be expressed as

$$K_{ij} = \frac{U_I}{\sqrt{U_M U_E}} = d_{ij}\sqrt{\frac{1}{\varepsilon^T s^E}} = e_{ij}\sqrt{\frac{1}{\varepsilon^T c^E}} = g_{ij}\sqrt{\frac{\varepsilon^T}{s^E}} = h_{ij}\sqrt{\frac{\varepsilon^S}{c^D}} \tag{2-8}$$

where U_I, U_M, and U_E represent the output energy density of piezoelectric ceramic, storage mechanical energy density of piezoelectric ceramic, and storage electrical energy density of piezoelectric ceramic, respectively.

2.3 Piezoelectric equations and vibration modes

2.3.1 Piezoelectric equations

The piezoelectric equation is a unified description of the piezoelectric materials of dielectricity, elasticity, and piezoelectricity. As for the piezoelectric vibrator, there are electrical boundary conditions including short circuit and open circuit, and mechanical boundary conditions including mechanical freedom and mechanical clamping. Thus, four types of piezoelectric equations can be obtained by considering different combinations of the two boundary conditions, as listed in Table 2-1.

Table 2-1. Four types of piezoelectric equations

Type	Boundary condition	Piezoelectric equation
(1)	Mechanical freedom: $T = 0, S \neq 0$ Short circuit: $E = 0,\ D \neq 0$	$\begin{bmatrix} S_i \\ D_m \end{bmatrix} = \begin{bmatrix} s_{ij}^E & d_{ni} \\ d_{mj} & \varepsilon_{mn}^T \end{bmatrix} \begin{bmatrix} T_j \\ E_n \end{bmatrix}$
(2)	Mechanical clamping: $T \neq 0, S = 0$ Short circuit: $E = 0,\ D \neq 0$	$\begin{bmatrix} T_j \\ D_m \end{bmatrix} = \begin{bmatrix} -e_{nj} & c_{ji}^E \\ \varepsilon_{mn}^S & e_{mi} \end{bmatrix} \begin{bmatrix} E_n \\ S_i \end{bmatrix}$
(3)	Mechanical freedom: $T = 0, S \neq 0$ Open circuit: $E \neq 0,\ D = 0$	$\begin{bmatrix} S_i \\ E_n \end{bmatrix} = \begin{bmatrix} g_{mi} & s_{ij}^D \\ \beta_{mn}^T & -g_{nj} \end{bmatrix} \begin{bmatrix} D_m \\ T_j \end{bmatrix}$
(4)	Mechanical clamping: $T \neq 0, S = 0$ Open circuit: $E \neq 0,\ D = 0$	$\begin{bmatrix} S_i \\ D_m \end{bmatrix} = \begin{bmatrix} c_{ji}^D & -h_{mj} \\ -h_{ni} & \beta_{nm}^S \end{bmatrix} \begin{bmatrix} S_i \\ D_m \end{bmatrix}$

(*i, j*=1,2,3,4,5,6; *m, n*=1,2,3)

Type (2) of the piezoelectric equation is generally used for analysis and calculation of the piezoelectric actuator. T_j, D_m, E_n, S_i, c_{ji}^E, e_{mi}, ε_{mn}^S represent mechanical stress vector, electric displacement vector, electric field strength vector, mechanical strain vector, elastic stiffness coefficient, piezoelectric stress constant, and dielectric constant, respectively.

2.3.2 Vibration modes

Based on the inverse piezoelectric effect, a variety of vibration modes can be excited when the alternating electric field is applied to the piezoelectric ceramic in some specific directions. Vibration modes of the piezoelectric transducer include longitudinal extension parallel to the electric field direction (LE), transverse contraction perpendicular to the electric field direction (TE), and thickness shear mode (TS), as shown in Fig. 2-4.

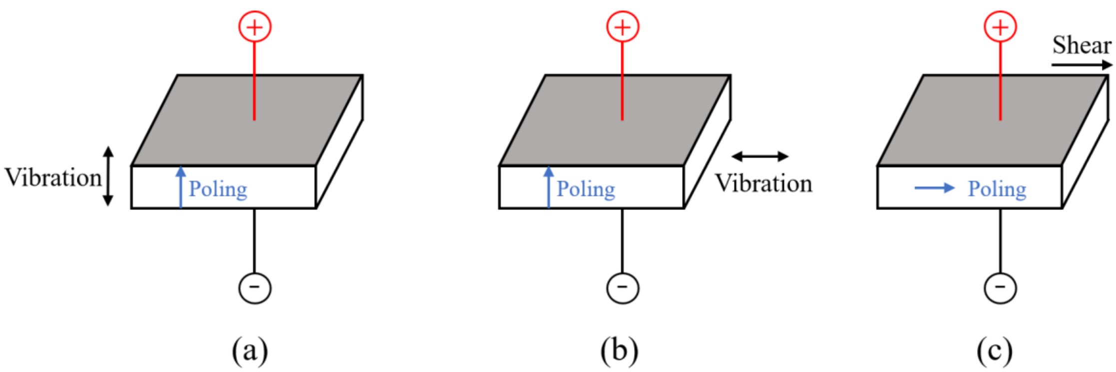

Fig. 2-4. Vibration modes. (a) Longitudinal extension (LE), (b) transverse contraction perpendicular to the electric field direction (TE), and (c) shear mode (TS).

The piezoelectric stack used in this study utilizes the LE mode (d_{33} effect) of piezoelectric ceramics.

2.4 Piezoelectric stack

2.4.1 Structure of the piezoelectric stack

Under the longitudinal extension (LE) mode, to obtain a large output load or deformation with a low driving voltage, multiple piezoelectric ceramic layers are mechanically connected in series and electrically connected in parallel to consist of the piezoelectric stack. The structure schematic diagram of the piezoelectric stack is shown in Fig. 2-5. The piezoelectric stack is mainly composed of multiple piezoelectric ceramics, insulation layers, internal electrodes, and external electrodes. The polarization direction of adjacent piezoelectric ceramic layers is the opposite.

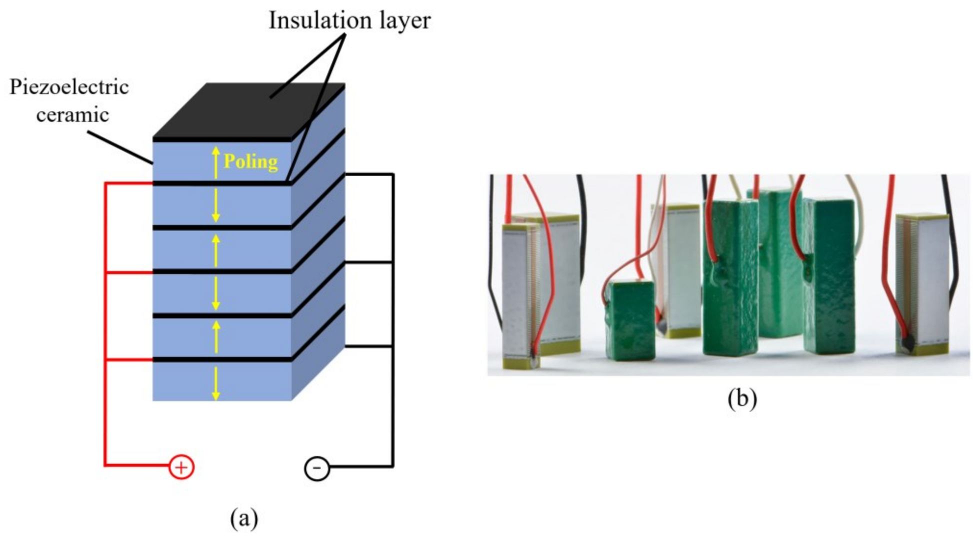

Fig. 2-5. Piezoelectric stack. (a) Structure schematic diagram and (b) products by PIEZOTECHNICS.

2.4.2 Performance of piezoelectric stack

Output force and output displacement are two key characteristics of piezoelectric stacks.

When a voltage signal is applied in the polarization direction, the multilayer piezoelectric ceramic layers all output displacement, and the total output displacement of the piezoelectric stack Δh is equal to the sum of the output displacement of the multilayer piezoelectric ceramic layers, expressed as

$$\Delta h = n \cdot d_{33} \cdot V \tag{2-9}$$

where n, and V represent the number of piezoelectric ceramic layer and applied voltage, respectively.

The output force F_{PZT} of the piezoelectric actuator can be calculated by

$$F_{PZT} = k_{PZT} \cdot \Delta h = k_{PZT} \cdot n \cdot d_{33} \cdot V \tag{2-10}$$

where k_{PZT} denotes the equivalent stiffness of the piezoelectric stack.

It can be seen that the output displacement of the piezoelectric stack can be increased by increasing the number of piezoelectric ceramic layers or the driving voltage. In addition, with the same output displacement, the voltage applied to the piezoelectric stack is 1/n of that applied to the single-layer piezoelectric ceramic.

The hysteresis characteristic of a piezoelectric stack is an inherent property of piezoelectric materials [72]. Among the many factors that affect the output accuracy of the piezoelectric stack, the influence of hysteresis is relatively significant. The hysteresis characteristic of a piezoelectric stack by THORLABS is shown in Fig. 2-6. When the same voltage is applied to the piezoelectric stack, the output displacements during the loading and unloading stages are not the same. The shape and characteristics of the hysteresis mode are related to the voltage difference of the applied voltage signal, temperature, and applied load. Charge control or closed-mode system control can effectively reduce hysteresis effects to achieve precision control.

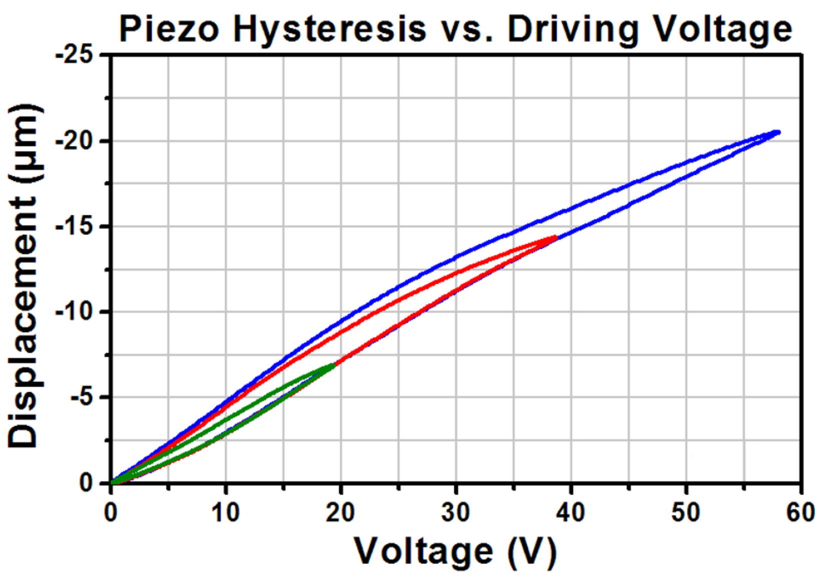

Fig. 2-6. Hysteresis characteristics of the piezoelectric stack.

2.4.3 Usage guidelines of piezoelectric stack

Piezoelectric stacks are the core drive element of piezoelectric actuators. The performance superiority or inferiority of the piezoelectric stack will directly affect the performance of the actuator. Thus, the following aspects should be paid attention to:

(1) The piezoelectric stack has a strong compression resistance, but poor tensile and shear resistance, so a preload should be added in actual, generally 50% of the maximum output force;

(2) The piezoelectric stack should be fixed vertically between the mount and the driven body, and the contact area between the mount and the driven body and the piezoelectric stack should be not less than the end area of the piezoelectric stack;

(3) Piezoelectric stacks should operate within the allowable temperature and humidity range;

(4) The piezoelectric stack must be operated under a positive voltage (same as polarization direction) and should avoid working for a long time in the DC high-voltage state, otherwise it will easily cause the depolarization of the piezoelectric stack, resulting in failure;

(5) It is recommended to use epoxy adhesive when bonding a piezoelectric stack to other surfaces.

2.4.4 Piezo-actuated principle using piezoelectric stack

Compared with resonant piezoelectric actuators, non-resonant piezoelectric actuators can operate at non-resonant frequencies. They usually realize mechanical motions by combining the static deformations of piezoelectric elements and the static friction force between the stator and slider and have the advantages of high precision, high stability, and a simple control system.

Non-resonant piezoelectric linear actuators often use piezoelectric stacks as the core driving element and generally consist of several main parts: stator part, mechanical clamping part, slider guide part, and preload mechanism. When the voltage is applied to the piezoelectric stack, the mechanical energy generated by the inverse piezoelectric effect is transmitted to the stator, which leads to a motion on the driving foot of the stator. This motion will be transferred to the slider guide part through the friction between the stator and the slider, so as to output macro linear motion. The whole system composition of the non-resonant piezoelectric actuator is shown in Fig. 2-7.

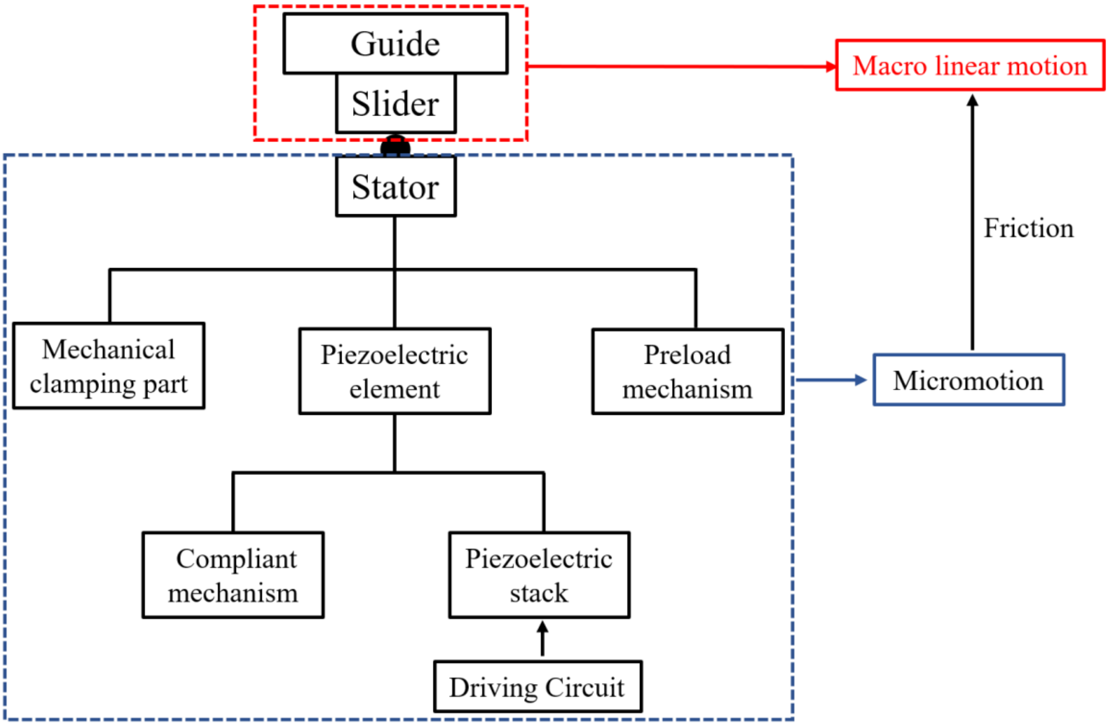

Fig. 2-7. Whole system composition of the non-resonant piezoelectric actuator.

The design of the stator will become very flexible based on the piezoelectric stack, which results in different piezo-actuated principles. Existing non-resonant piezoelectric actuators have four kinds of actuation methods: (1) direct actuation, (2) inertial actuation, and (3) clamping-feeding actuation.

2.4.4.1 Direct actuation

Direct actuation utilizes the deformation of piezoelectric stacks to directly drive the objects. High acceleration output and theoretically infinitely small resolution can be realized. In addition, the short transmission chain and fewer intermediate links also increase the rigidity of the system using direct drive, which is suitable for applications that have strict requirements on response speed and actuation accuracy.

2.4.4.2 Inertial actuation

Inertial actuation is also known as stick-slip actuation. The piezoelectric stacks are excited by a sawtooth waveform signal with different duty ratios, as shown in Fig. 2-8. During the stick phase, the piezoelectric stack extends slowly and drives the slider to move by a displacement. Then, during the slip phase, the piezoelectric stack contracts rapidly, while the slider does not move due to inertia. By repeating these two steps, macro linear motion can be achieved.

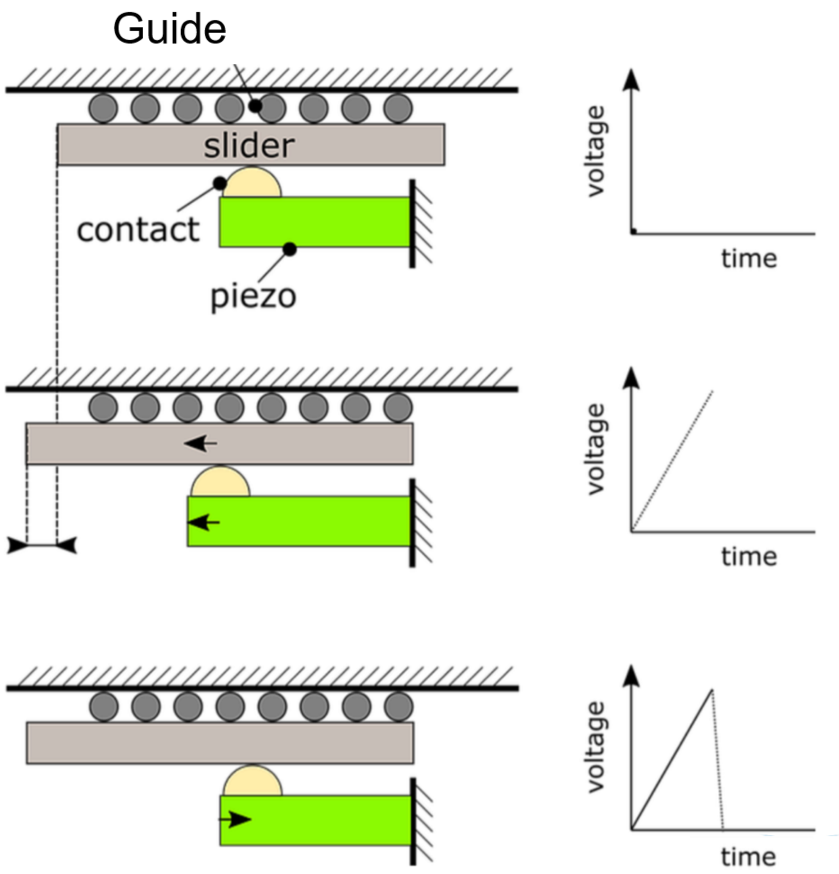

Fig. 2-8. Inertial actuation.

2.4.4.3 Clamping-feeding actuation.

Clamping-feeding actuation method is generally used for inchworm piezoelectric actuators. Two groups of clamping piezoelectric stacks and a group feeding piezoelectric stacks are required for actuation. The output displacement of the slider is accumulated by means of alternate clamping by two sets of clamping piezoelectric stacks, as shown in Fig. 2-9.

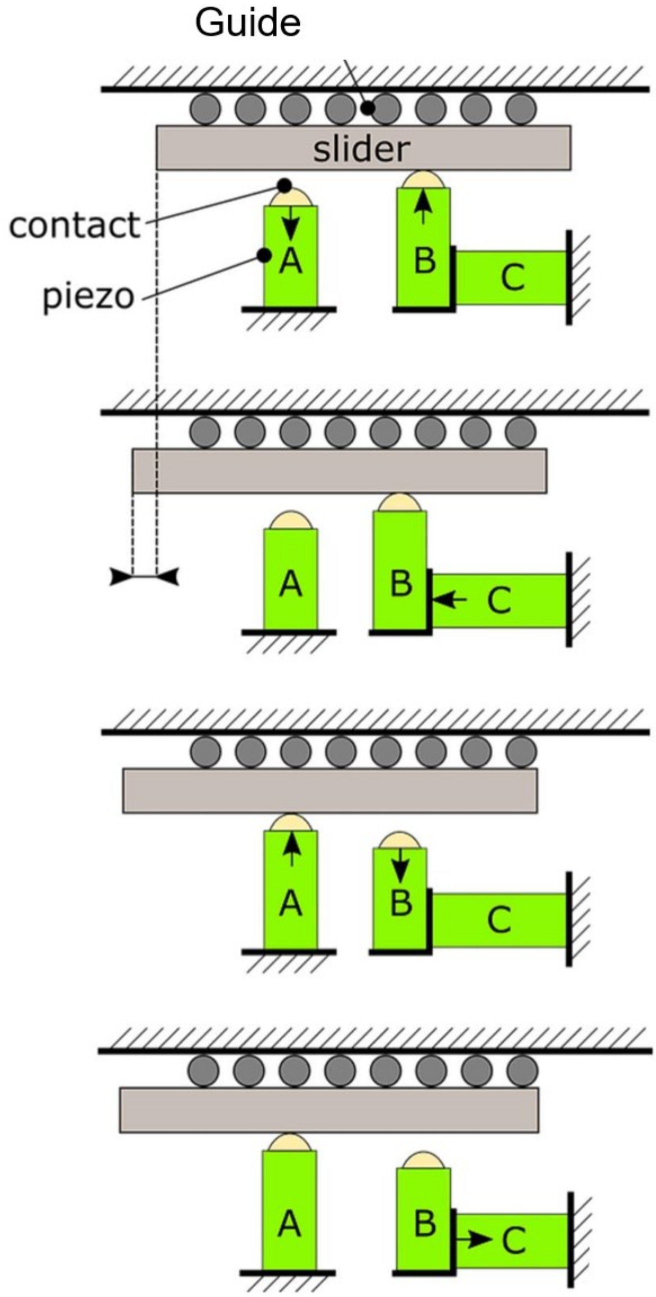

Fig. 2-9. Clamping-feeding actuation.

In addition, non-resonant piezoelectric actuators can realize two working modes of stepping drive mode and continuous drive mode. Under these two working modes, high-precision positioning, and large stroke are achieved, respectively.

2.5 Conclusion

This chapter first introduces the performance parameters and piezoelectric equations of piezoelectric ceramics in detail. Then, the characteristics and usage guidelines of the piezoelectric stacks were summarized. Finally, the piezo-actuated principles using the piezoelectric stack were discussed.

3. Dual-side drive walking-type piezoelectric linear actuator with parallel-arrangement stators

3.1 Introduction

Walking-type piezoelectric actuators have been able to achieve the performance of high precision, low speed with a large stroke, and no backward motion, and can be expected to be applied for driving the aperture plate in the optical system of SEM and other precision positioning fields. However, existing walking-type piezoelectric actuators still have drawbacks such as wear problems, and complex structure and control systems. Therefore, it is necessary to further study the walking-type piezoelectric actuators.

Based on the previously designed single stator non-resonant linear ultrasonic actuator [73], we proposed a novel dual-side walking-type piezoelectric linear actuator with the parallel-arrangement dual stator to solve the above industrial issues. This chapter first introduces the configuration of the actuator and its operating principle under multiple driving modes. Then, the design and optimization of the parallel compliant mechanism by combining the finite element method (FEM) and response surface methodology (RSM) are explained. Finally, a prototype of the actuator and a series of experiments to investigate its output performances are discussed.

3.2 Structure design and operating principle

3.2.1 Configuration

The proposed dual-stator structure is shown in Fig. 3-1(a). The structure is composed of a frame, two stators, four blocks, and two preload bolts. Two stators are nested in the frame between each pair of blocks, and the preload bolts are used to provide the required preload for the operation of the piezoelectric stacks. The frame, parallel compliant mechanisms, and driving feet are made of SUS303 stainless steel, SUS304 stainless steel, and alumina, respectively. Each stator consists of two piezoelectric stacks, a parallel compliant mechanism, and two driving feet. All of the single stator components are glued together with epoxy adhesive. The dimension of the dual-stator structure is 42×28×5 mm. One of the schematic diagrams of the actuator based on the dual stator is shown in Fig. 3-1(b). The frame of the stator is seen as a base, and the sliders and guides on both sides of the stator are connected to the frame via the preload bolts and coil springs. The spring force can give the preload between the slider and stator when the preload bolts are tightened. A connecting plate is used to link two sliders to output a linear movement along the x-axis. It can be seen that a miniaturized and compact actuator is expected to be realized based on the proposed dual-stator structure. In this study, to obtain the accurate preload value and evaluate the output characteristics of the dual-stator actuator at various preloads, the combination of the coil spring and preload bolt was replaced by the preload mechanism consisting of the coil spring and micrometer. Meanwhile, a piece of test equipment using such a preload mechanism was developed.

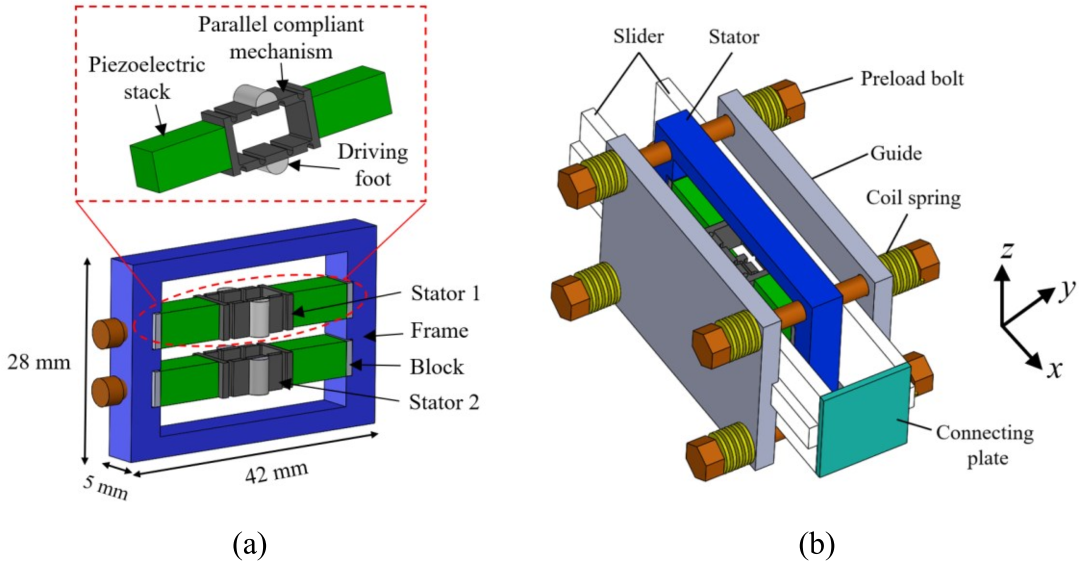

Fig. 3-1. The proposed dual-stator actuator. (a) Structure and dimension of the stator. (b) One of the schematic diagrams of the proposed actuator.

The test equipment of the proposed piezoelectric linear actuator with the symmetrical structure and the dual stator is illustrated in Fig. 3-2. Two sliders made of alumina are guided by two cross-roller guides. The connecting blocks are used to connect the cross-roller guides and sliding platforms with bolts. The preload mechanisms of both two sides are arranged to provide and adjust the preload between the sliders and driving feet through the micrometers and coil springs. Here, the preload value is equal to the screw-in distance of the micrometer multiplied by the spring constant (Hooke's Law). The connecting plate is used to connect two sliders and output the displacement and thrust in the x-axis direction. All of the parts are assembled on a base. The dimension of the actuator test equipment is 100×50×42 mm.

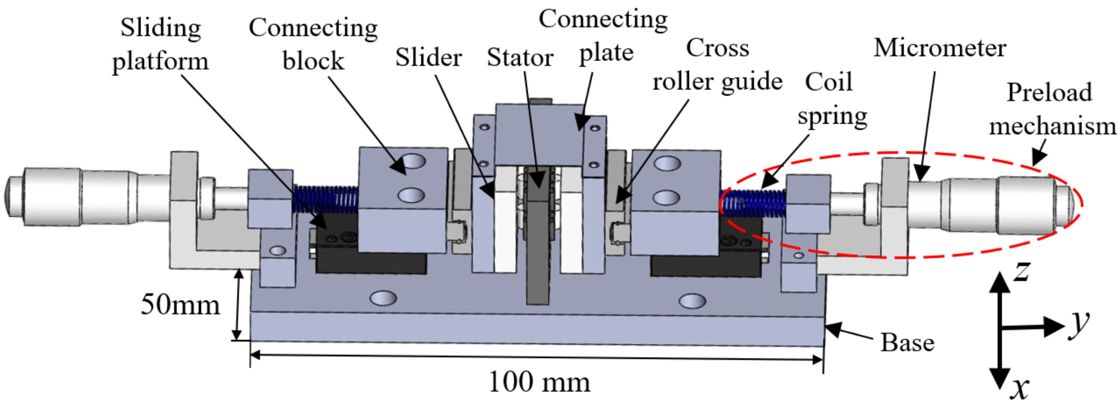

Fig. 3-2. Configuration and dimensions of the test equipment of the proposed actuator with a dual stator.

In contrast to the existing walking-type piezoelectric actuators, the actuator with a parallel-arrangement dual stator proposed in this paper can be expected to be as follows:

(1) The output thrust is larger because the slider is driven by the driving feet on both sides as in the single stator.

(2) The slipping phenomenon can be reduced by applying a gentle sinusoidal waveform voltage instead of the sawtooth waveform in stick-slip type driving, thus the wear problem is decreased.

(3) Four piezoelectric stacks with only one poling direction are fixed on two sides of the parallel compliant mechanisms and parallel to the direction of the slider motion. Meanwhile, two stators are arranged up and down in parallel in one frame rather than in a line. Accordingly, it is conducive to realizing a compact and miniaturized structure.

(4) It is possible to achieve more driving modes due to the different motion trajectories of the driving feet under various operating voltage signals.

3.2.2 Operating principle

The dual-stator actuator is proposed based on the single-stator structure. Thus, the operating principle of the single-stator is elaborated first. During operation, two driving feet on both sides of the parallel compliant mechanism make the same motion due to the symmetrical structure of the single stator. Therefore, the simplified geometric model of a half-parallel compliant mechanism is realized, as illustrated in Fig. 3-3. This model was used to analyze the trajectory of the driving foot.

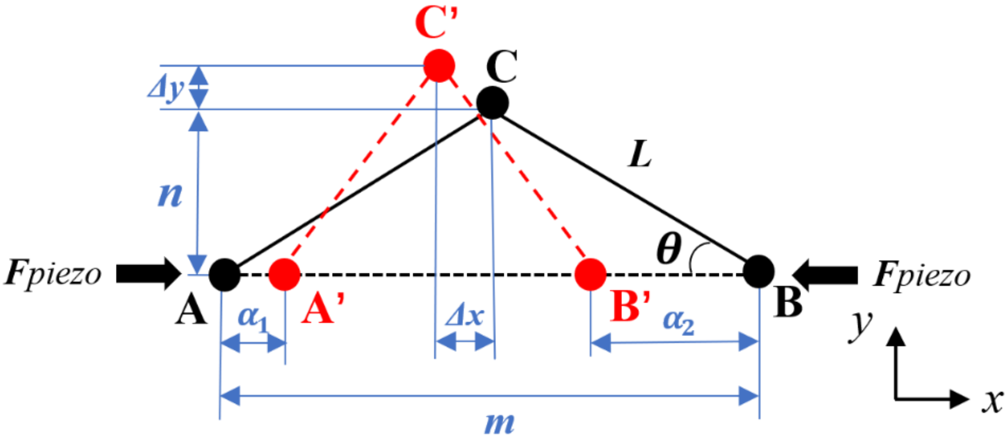

Fig. 3-3. Simplified geometric model of a half-parallel compliant mechanism.

At the initial position, points A and B are vertices on both sides of the parallel compliant mechanism. Point C is the apex of the driving feet. θ is the angle formed by line segments AB and BC. Spans m and n are the length of line segment AB and the distance between C to the line segment AB, respectively. F_{piezo} represents the force generated by the piezoelectric stack, which is perpendicular to the direction of the preload. The parallel compliant mechanism is continuously driven by the force F_{piezo} with a phase difference. This causes the positions of points A, B, and C to move to A', B', and C', respectively. Spans α_1 and α_2 are the motion displacements of points A and B generated by the two piezoelectric stacks. Movements Δx and Δy are motion displacements of point C in the x-axis direction and y-axis direction, respectively. Length L is the constant distance from points A and B to the center of the driving feet during the deformation of the parallel compliant mechanism. Using this geometric relationship, the following equations were obtained:

$$\mathrm{AC} = \mathrm{BC} = A^{'}C^{'} = B^{'}C^{'} = L \tag{3-1}$$

$$\Delta x = \frac{\alpha_2 - \alpha_1}{2} \tag{3-2}$$

$$\left(\frac{m}{2}\right)^2 + n^2 = \left[\frac{(m - \alpha_2 - \alpha_1)}{2}\right]^2 + (n + \Delta y)^2. \tag{3-3}$$

The values of α_1, α_2, and Δy are all measured in micrometers, and are much smaller than the size of the parallel compliant mechanism. Thus,

$$\left(\frac{\alpha_1 + \alpha_2}{2}\right)^2 \approx 0 \tag{3-4}$$

$$(\Delta y)^2 \approx 0. \tag{3-5}$$

Combining Eqs. (3-3)-(3-5) allows Δy to be expressed as

$$\Delta y = \frac{1}{tan\theta} \cdot \frac{\alpha_1 + \alpha_2}{2} \ . \tag{3-6}$$

Because the piezoelectric stack can only work under a positive voltage, when the piezoelectric stacks of both sides are excited by a combination of two sinusoidal voltages with a phase difference of 90° and offset voltages, α_1 and α_2 can be described as

$$\alpha_1 = nd_{33}V(1 + sin\omega t) \tag{3-7}$$

$$\alpha_2 = nd_{33}V(1 + cos\omega t) \tag{3-8}$$

where *n*, d_{33}, and *V* are the number of ceramic layers in the piezoelectric stack, the piezoelectric strain coefficient, and the voltage amplitude, respectively. All of these values are constant. If we assume that

$$nd_{33}V = \delta \tag{3-9}$$

α_1 and α_2 can be rewritten as follows:

$$\alpha_1 = \delta(1 + sin\omega t) \tag{3-10}$$

$$\alpha_2 = \delta(1 + cos\omega t). \tag{3-11}$$

By substituting Eqs. (3-10) and (3-11) into (3-2) and (3-6), respectively, the following equations are obtained:

$$\begin{cases} \Delta x = \dfrac{\delta(cos\omega t - sin\omega t)}{2} \\ \Delta y = \dfrac{1}{tan\theta} \cdot \dfrac{\delta(2 + sin\omega t + cos\omega t)}{2} \end{cases} . \tag{3-12}$$

After eliminating the parameter *t*, the following formula is obtained:

$$\left(\frac{\Delta x}{\frac{\sqrt{2}}{2}\delta}\right)^2 + \left(\frac{\sqrt{2}tan\theta}{\delta}\Delta y - \sqrt{2}\right)^2 = 1. \tag{3-13}$$

Eq. (3-13) indicates that the motion trajectory of the driving feet is an ellipse.

The elliptical motion of the driving foot on the stator can be decomposed into motion parallel and perpendicular to the direction of the slider motion. In an operation cycle, when a certain preload is applied between the sliders and driving feet by the preload spring, the perpendicular motion applies a vertical force to the sliders, and the parallel motion moves the sliders by displacement x_1 with the friction force, as shown in Fig. 3-4. The sliders can realize a large-stroke linear motion by repeating the above process.

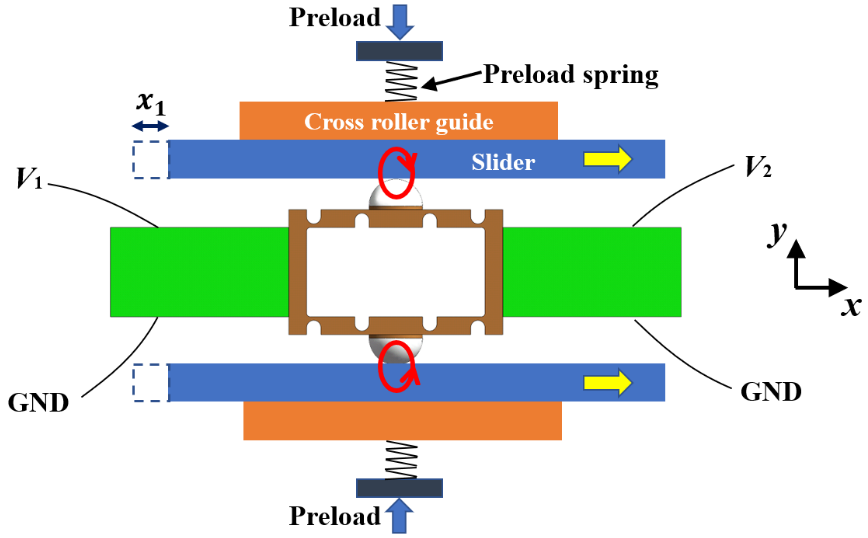

Fig. 3-4. Operating principle of the single stator.

3.2.2.1 Operating principle of the co-drive mode

The sinusoidal voltages V_1-V_4 applied to the four piezoelectric stacks of the dual stator are shown in Fig. 3-5 and Eq. (3-14) for the co-drive mode.

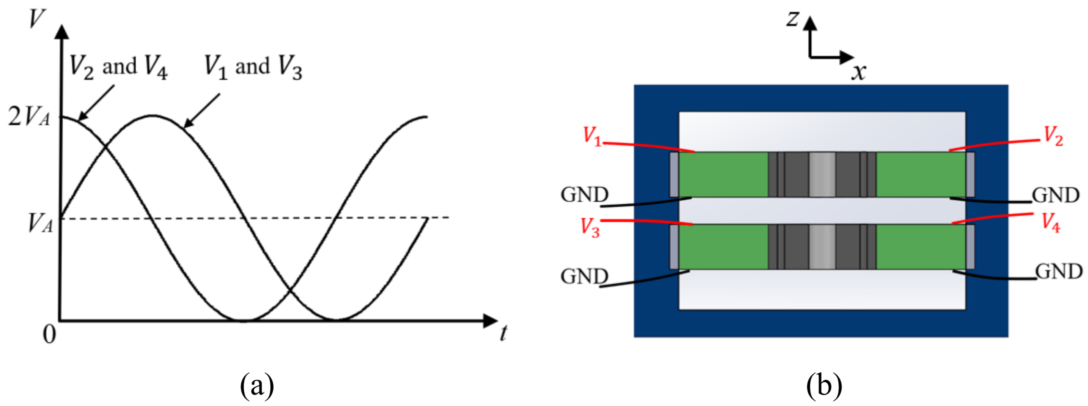

Fig. 3-5. Co-drive mode. (a) Sinusoidal voltage signals and (b) dual stator.

$$\begin{cases} V_1 = V_3 = V_A(1 + sin\omega t) \\ V_2 = V_4 = V_A(1 + cos\omega t). \end{cases} \tag{3-14}$$

The voltages of V_1, V_2 and V_3, V_4 are applied to stator 1 and stator 2, respectively. The phase difference between the applied voltages V_1 and V_2 is 90°, and V_1 and V_3, V_2 and V_4 are in phase. As a result, the driving feet of the two stators will make an in-phase elliptical motion to drive the sliders. This indicates the same operating principle as that of a single stator.

3.2.2.2 Operating principle of the alternate-drive mode

The sinusoidal voltages V_1-V_4 applied to the four piezoelectric stacks of the dual stator are described in Fig. 3-6 and Eq. (3-15) for the alternate-drive mode. The phase difference from the applied voltages V_1 to V_4 is 90° in turn so that the driving feet of the two stators will make alternating elliptical motions with a half-cycle difference. The input voltages are divided into two stages corresponding to two operating processes in one working cycle. The detailed operating principle of the alternate-drive mode is illustrated in Fig. 3-7. For ease of description, two stators are placed in line to explain the principle. This is the same effect as the two stators mounted above and below each other.

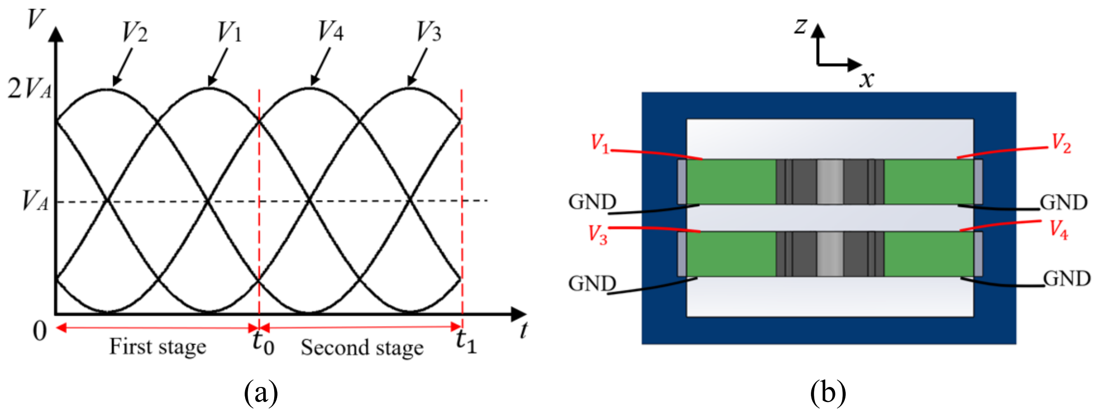

Fig. 3-6. Alternate-drive mode. (a) Sinusoidal voltage signals and (b) dual stator.

$$\begin{cases} V_1 = V_A(1 + sin\omega t) \\ V_2 = V_A(1 + cos\omega t) \\ V_3 = V_A(1 - sin\omega t) \\ V_4 = V_A(1 - cos\omega t) \end{cases}. \tag{3-15}$$

First, during the first stage ($0 < t < t_0$), the operating process is shown in Fig. 3-7(a). The driving foot on stator 1 contacts the slider and moves in the upper half of the elliptical trajectory under the input voltages of V_1 and V_3. Friction causes the slider to be driven to move a displacement x_1. Meanwhile, the driving foot of stator 2 traces the motion in the bottom half of the elliptical trajectory under the input voltages of V_2 and V_4, and is separated from the slider.

Then, during the second stage ($t_0 < t < t_1$), the operating process is shown in Fig. 3-7(b). The driving feet of both stators reach the two vertices on the x-axis of the elliptical trajectory again first, and then the driving feet reverse roles (driving vs. separated). The driving foot on stator 2 moves in the upper half of the elliptical trajectory and continues to drive the slider to move a displacement x_2 by friction thanks to the input voltages of V_2 and V_4. On the contrary, the driving foot on stator 1 is separated from the slider due to the input voltages of V_1 and V_3.

It can be seen that the alternate-drive mode of the actuator drives the sliders two times in an operating cycle. By repeating the above sequence, the slider can realize a large stroke motion.

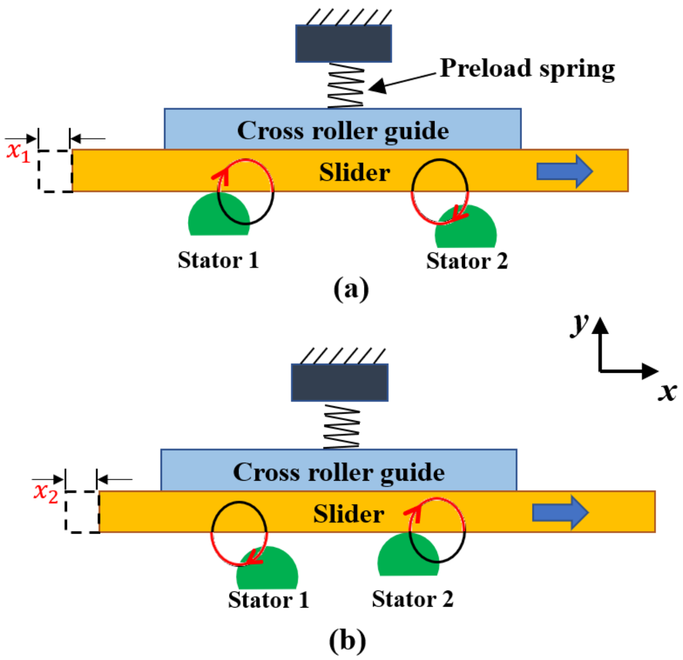

Fig. 3-7. Operating principle of the alternate-drive mode. (a) First stage and (b) second stage.

3.2.2.3 Operating principle of the precision positioning mode

The voltages V_1-V_4 applied to the four piezoelectric stacks of the dual stator are described in Fig. 3-8 for the precision positioning mode. The positioning resolutions of the forward and reverse motions can be evaluated by applying voltages V_1, V_3 and V_2, V_4, respectively. At each increasing stage of the voltage, the slider could be pushed to move a displacement x_1 by driving foot due to the deformation of the parallel compliant mechanism, as shown in Fig. 3-9.

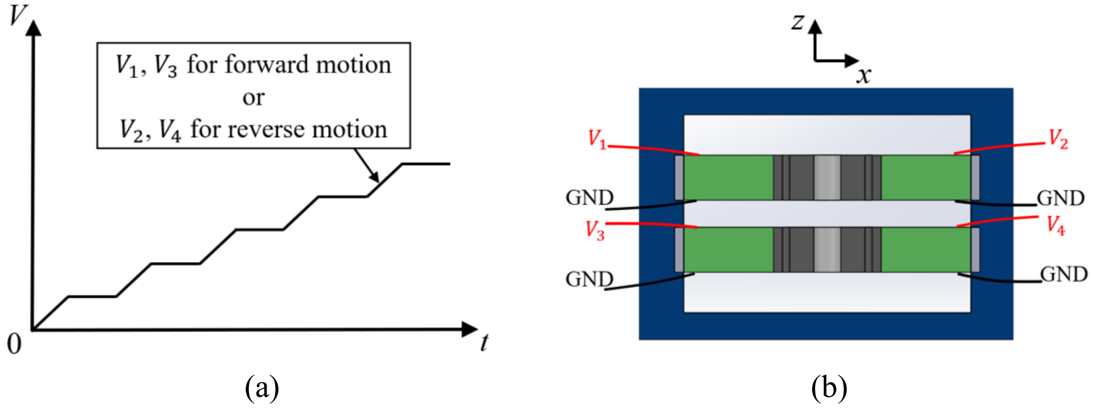

Fig. 3-8. Precision positioning mode. (a) Stepping voltage signals and (b) dual stator.

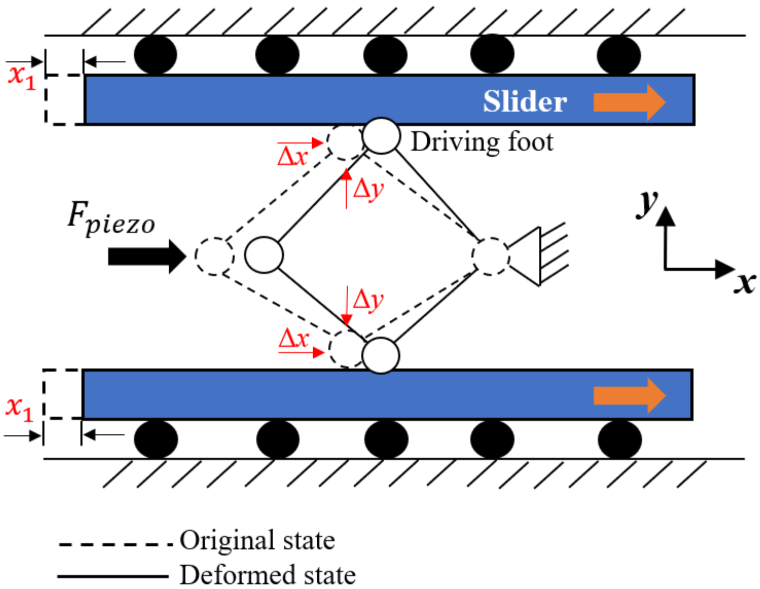

Fig. 3-9. Operating principle of the precision positioning mode.

In summary, the proposed dual-stator actuator is able to work in three different operation modes. The co-drive mode shows the same operating principle as a single-stator actuator and aims to compare it with the performance of the dual-stator actuator using alternate drive mode. The characteristics of speed, thrust, and stepping displacement of the proposed actuator can be evaluated under the alternate drive mode. Moreover, the precision positioning mode is used to test the positioning resolution of the actuator.

3.2.3 Structure design and optimization

From the analysis of the operating principle, the working stability and thrust of the proposed actuator will be determined by the deformation of the parallel compliant mechanism along the y-axis directly. Thus, the structure of the parallel compliant mechanism shown in Fig. 3-10(a) is designed and optimized by combining the finite element method (FEM) and response surface methodology (RSM) in this study.

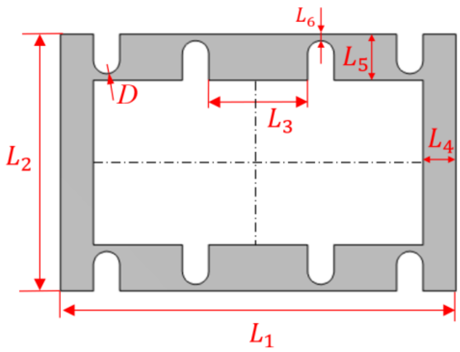

(a)

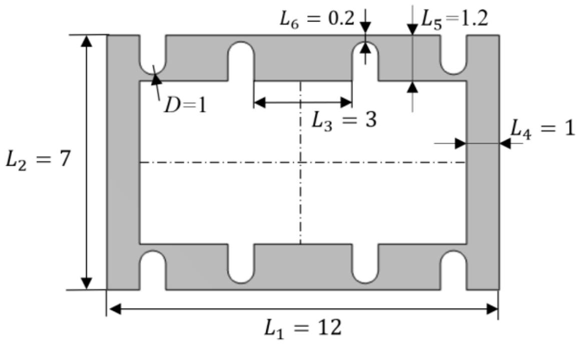

(b)

Fig. 3-10. Parallel compliant mechanism. (a) Main structure parameters of parallel compliant mechanism and (b) previous structure.

FEM is used with COMSOL Multiphysics 5.6 to evaluate the y-directional displacement y and maximum equivalent stress σ of the parallel compliant mechanisms with different sizes. Based on the previously studied structure of the parallel compliant mechanism as described in Fig. 3-10(b), the finite element mesh model of the stator and the boundary conditions are shown in Fig. 3-11. Both sides of the stator are fixed. The size of the piezoelectric stack is $5 \times 5 \times 10$ mm, and it is equipped with 100 layers of piezoelectric ceramics (PZT-5H). Two surfaces perpendicular to the axial direction of each piezoelectric ceramics are set as electrodes, and the polarization directions of adjacent ceramics are opposite. The materials of the parallel compliant mechanism and driving feet are stainless steel (SUS304, yield strength of 205 MPa) and alumina, respectively. The applied voltages of V_1 and V_2 on the piezoelectric stacks are 100 V. The simulation results of y-directional displacement y and maximum equivalent stress σ are 6.44 μm and 100 MPa, respectively are shown in Fig. 3-12(a).

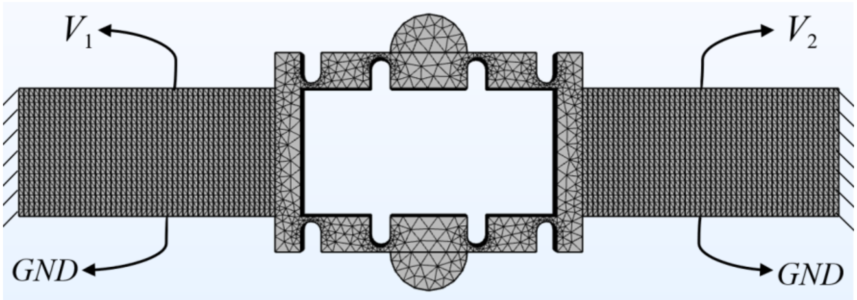

Fig. 3-11. Finite element mesh model of the stator and its boundary conditions.

RSM is selected to optimize the structure of the parallel compliant mechanism because output performances of the parallel compliant mechanism are affected by multiple variables at the same time. Here, the lengths L_1, L_2, L_4 and L_6 are determined to be 12, 7, 1 and 0.2 mm, respectively according to the experiences in the previous study and the limitation of the size of the stator. Three variables, Diameter D, thickness L_5 of the hinges, and the length L_3 are optimized furtherly in the range of 0.4-1.2 mm, 1-1.8 mm, and 2.6-3.4 mm, respectively. After the optimization by RSM (as described in **Appendix A**), the optimized size of the parallel compliant mechanism can be determined as shown in Table 3-1. The predicted values of y and σ of the optimized structure through RSM regression models are 8.38 μm and 136 MPa, respectively. FEM is used to verify the feasibility of the optimized result. With the optimized structure of the stator, the simulation results of y-directional displacement and maximum equivalent stress are 8.46 μm and 135 MPa (less than the yield strength of SUS304, 205MPa), respectively as presented in Fig. 3-12(b), which match well with the predicted value of the RSM regression models (maximum error = 0.95 %). Moreover, the simulation result of y-directional displacement has increased by 31.4 % compared to the previous structure.

Table 3-1. Parameters of the optimized structure.

Parameters	L_1 (mm)	L_2(mm)	L_3(mm)	L_4(mm)	L_5(mm)	L_6(mm)	D(mm)
Optimized structure	12	7	2.6	1	1	0.2	0.84

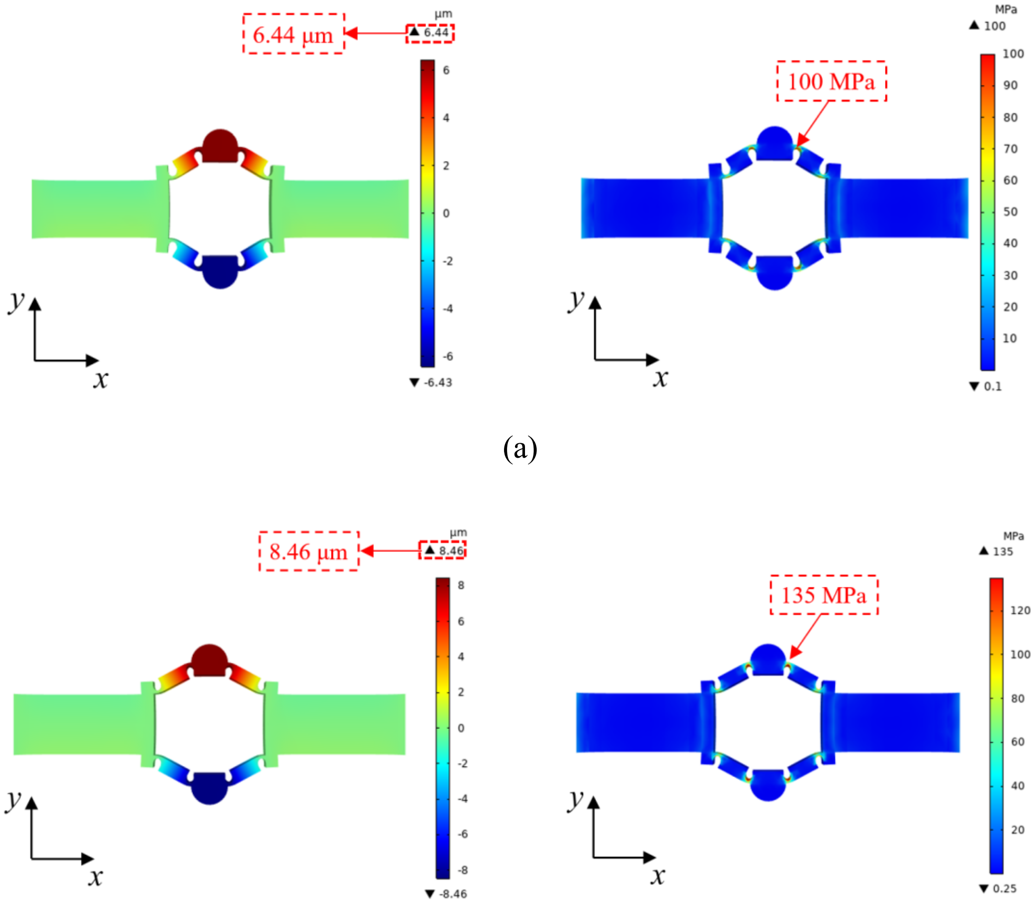

(a)

(b)

Fig. 3-12. Simulation results of y-directional displacement and maximum equivalent stress. (a) Previous structure and (b) optimized structure.

As for the optimized structure, the experimental result of y-directional displacement measured by the laser displacement meter (LDM) is shown in Fig. 3-13. The sampling period of the LDM was 200 ms. The maximum y-directional displacement of 8.2 μm was obtained under a DC voltage of 100 V. It indicates that there is only a 3.17% error between the FEM result and the experimental result. This is mainly caused by manufacturing errors, which are reflected in the fact that the dimensions of the manufactured parallel compliant mechanism are slightly different from the optimized values. All sum up, the optimized structure of the parallel compliant mechanism can be selected for further analysis.

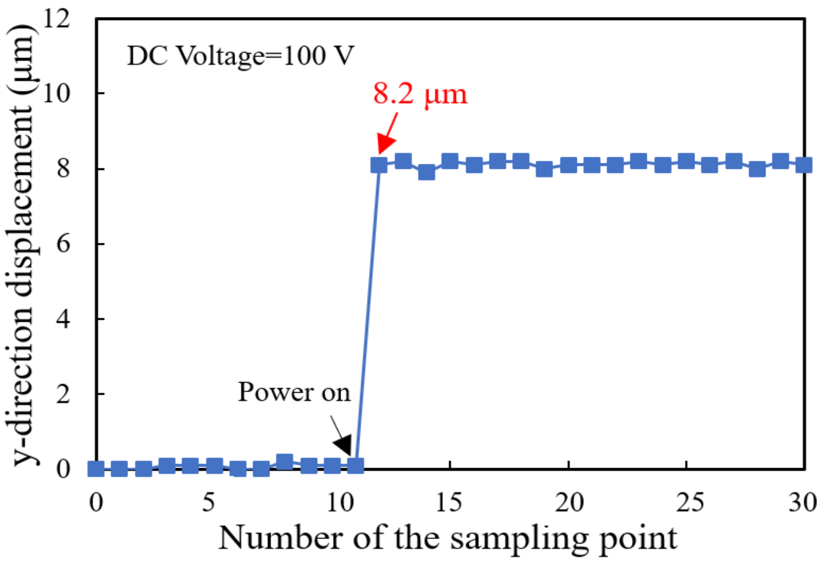

Fig. 3-13. Experimental result of y-directional displacement.

Afterward, the modal analysis of the stators is investigated through the FEM to avoid the resonant phenomenon. As illustrated in Fig. 3-14, the first four-order resonant frequencies are 13924.3 Hz, 14454.8 Hz, 16260.2 Hz, and 16694.9 Hz, respectively. Thus, these frequencies should be avoided during the operating process.

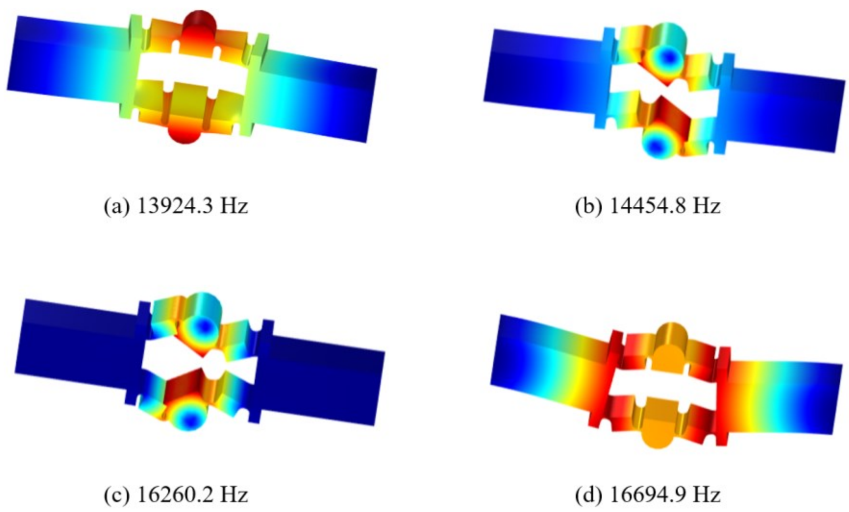

Fig. 3-14. Modal analysis of the stator. (a) First-order modal, (b) second-order modal, (c) third-order modal, and (d) fourth-order modal.

To research the output characteristics of the three driving modes, a piece of test equipment of the proposed actuator was manufactured, and experiments were performed, as discussed in section 3.3.

3.3 Experiments and discussion

A prototype of the test equipment of the proposed actuator with a dual stator was built, As described in Fig. 3-15(a), assembled by the piezoelectric stacks (FUJI CERAMICS, 5×5×10 mm) used for driving, two cross guides (GSG6-25, THK), and two sliding platforms (VRT 1025, THK). The experimental system is shown in Fig. 3-15(b). Two function generators (WF1974, NF Corp.) provided the required sinusoidal waveform voltage signals, which were amplified by two voltage amplifiers (HSA 4012, NF Corp.). An oscilloscope (DCS-2204E, TEXIO) was used to display the input voltages. A force gauge (FGP-0.5, SHIMPO) was used to measure the zero-speed thrust of the actuator. In addition, the output displacement and speed of the actuator were measured by a laser displacement sensor (LK-G3000V, KEYENCE), as shown in Fig. 3-16.

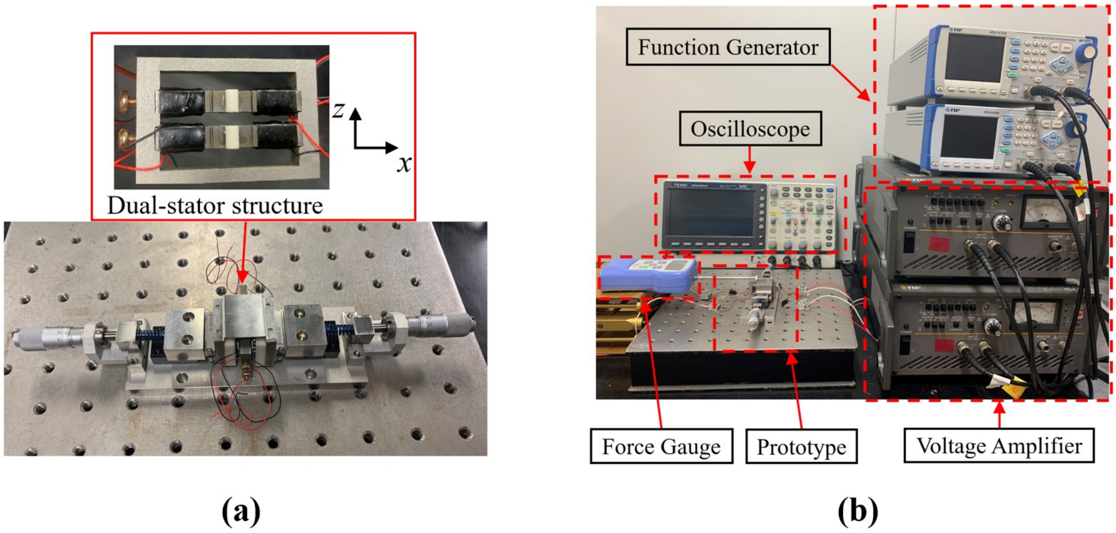

Fig. 3-15. Experimental system. (a) Prototype of the proposed actuator with a dual stator and (b) measurement of the thrust.

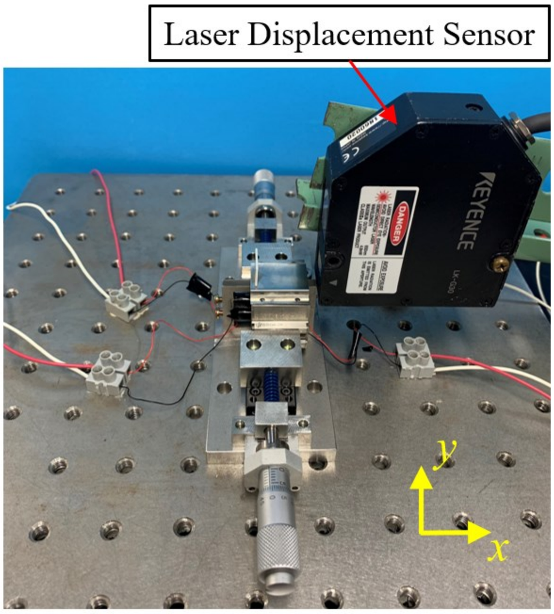

Fig. 3-16. Measurement system of the output displacement and speed.

3.3.1 Performance test for the co-drive mode

For the co-drive mode of the proposed actuator, the relationship between the no-load speed of the slider and the driving frequency is illustrated first in Fig. 3-17. The driving voltage, offset voltage, and preload were 100 Vp-p, 50 V, and 7.8 N, respectively. It can be seen that the actuator can work stably within 300-1000 Hz, and the no-load speed of the sliders increased with the increase of driving frequency. However, the slider has no macro displacement at a frequency lower than 300 Hz.

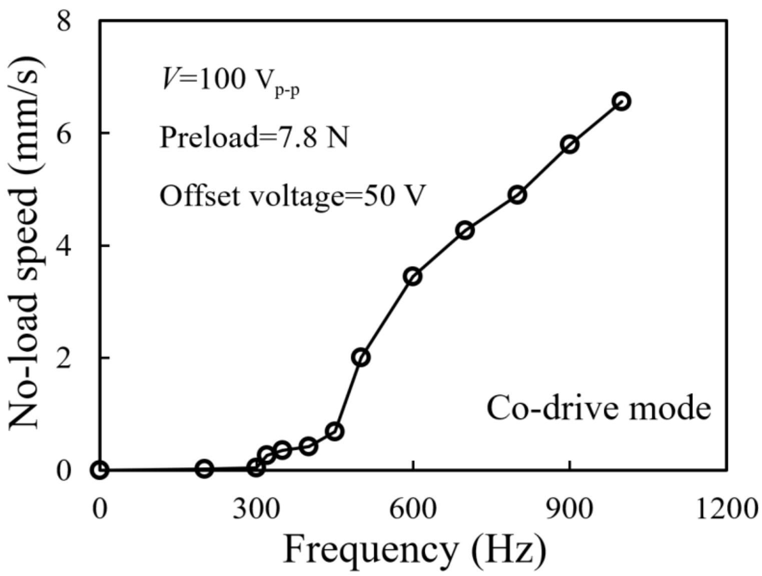

Fig. 3-17. No-load speed of the slider under the co-drive mode.

The co-drive mode can be viewed as the actuator driven by a single stator. Thus, the mass-spring system consisting of the slider and preload spring was proposed to explain the reason why the actuator cannot work at lower frequencies, as shown in Fig. 3-18.

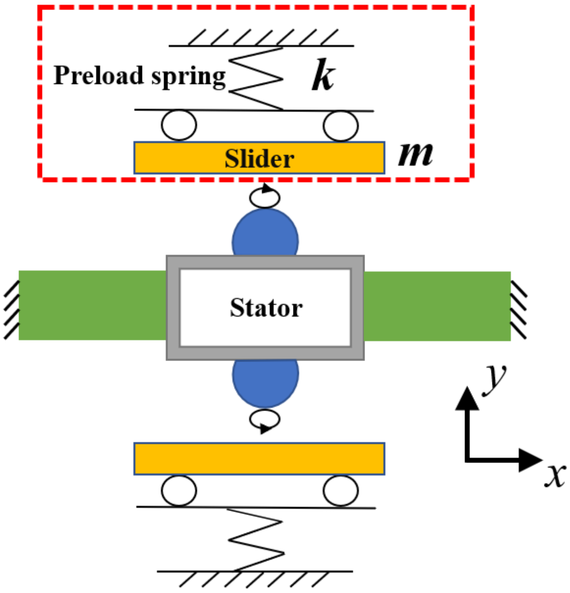

Fig. 3-18. Mass-spring system consisting of the slider and preload spring.

The natural frequency ω_1 of the mass-spring system can be calculated as

$$\omega_1 = \sqrt{\frac{k}{m}} \tag{3-16}$$

where k and m are the stiffness of the preload spring and mass of the slider in the mass-spring system, respectively.

When the drive frequency is greater than a critical value, the frequency of the elliptical motion of the driving feet on stator ω_2 is more than that on ω_1. This means that the spring response speed cannot keep up with the elliptical motion speed of the driving feet. Therefore, when the driving feet finish driving the sliders by making a motion in the upper half of the elliptical trajectory and move into the bottom half of the elliptical trajectory, the preload springs do not recover following the driving feet at this time. This causes the driving feet to be separated from the sliders. Then the driving feet continue moving into the upper half of the elliptical trajectory to contact and drive the sliders again. Thus, the slider movement is productive. However, suppose the frequency of the elliptical motion of the driving feet on stator ω_2 is lower than ω_1 at a lower driving frequency. The spring response speed is greater than the elliptical motion speed of the driving feet, which means that the driving feet cannot be separated from the sliders when they are in the bottom half of the elliptical trajectory and continue to drive the sliders, causing a reverse motion. As a result, the sliders only make a slight reciprocating motion without macroscopic linear motion. Under the co-drive mode, the driving feet may not separate from the sliders effectively at a driving frequency lower than 300 Hz, resulting in the failure of the proposed actuator. Thus, this driving mode has limitations for applications that require a lower output speed of the sliders at a lower driving frequency.

3.3.2 Performance test for the alternate-drive mode

As shown in Fig. 3-19, the relationship between the preload and thrust under the alternate-drive mode was evaluated first. The measurement result was obtained at a driving frequency of 100 Hz; the applied voltages were set to 50, 75, and 100 $V_{p\text{-}p}$; and the corresponding offset voltages were applied at 25, 37.5, and 50 V, respectively. The thrust increased first until it peaked with an increase of the preload and then began to decrease afterward. This is because, at a given input voltage, the contact force between the driving feet and the sliders increased as the preload increased. This increased the frictional driving force, which in turn increased the thrust. Then, as the preload increased further to a value greater than the force opposite to the direction of preload generated by the driving feet, the elliptical motion of the driving feet was restrained, and the driving feet did not separate from the sliders effectively, resulting in decreased thrust.

In this study, the preloads corresponding to the maximum thrust at different voltages were considered as the optimal preload. Under these preloads, the actuator had the highest thrust output performance and could operate more stably under a load. Thus, at the applied voltages of 50, 75, and 100 $V_{p\text{-}p}$, the optimal preloads were 8.6, 12.3, and 20.6N, respectively. The maximum thrust and its corresponding optimal preload increased as the applied voltage increased. This is because the force and displacement opposite the direction of preload generated by the driving feet increased with an increase in the applied voltage, allowing a larger preload to be applied to increase the contact force, which increased the maximum thrust. When the applied voltage and preload were 100 $V_{p\text{-}p}$ and 20.8N, respectively, the maximum thrust reached 7.3 N. The above optimal preload under different voltages was used for subsequent experiments.

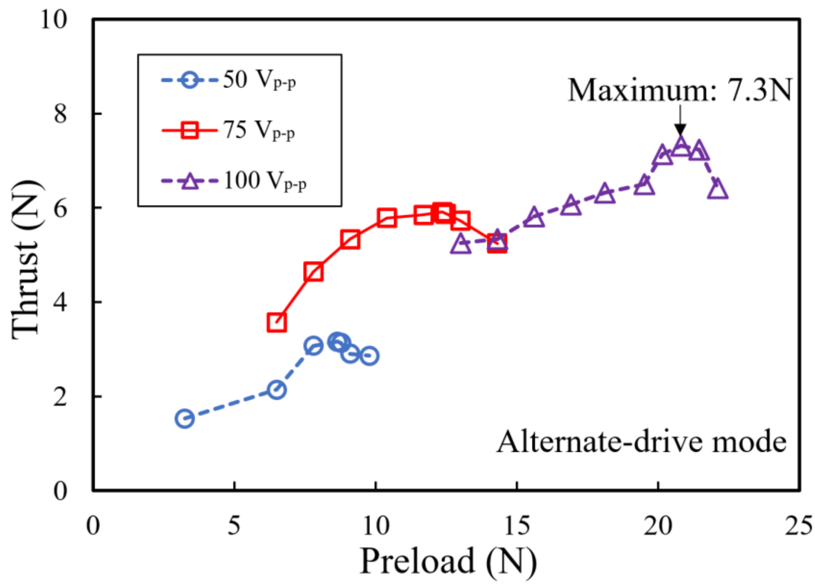

Fig. 3-19. Relationship between the preload and thrust under the alternate-drive mode at 50, 75, and 100 $V_{p\text{-}p}$ and 100 Hz.

Afterward, the relationship between the no-load speed of the sliders and the driving frequency was evaluated. The experimental data are plotted in Fig. 3-20. Fig. 3-20(a) shows the characteristics of low-speed operation. When the applied voltage was 50 $V_{p\text{-}p}$, the offset voltage was 25 V, and the preload was 8.6 N, the no-load speed of the sliders increased from 0.06 to 1.2 mm/s between 10 to 500 Hz. The characteristics of high-speed operation are shown in Fig. 3-20(b). The speeds at high frequencies were measured in a very short operating time to avoid high heat generation. The applied voltage was kept the same at 100 $V_{p\text{-}p}$, and the preload was 20.8 N. As the driving frequency increased from 500 to 3000 Hz, the no-load speed of the actuator varied almost linearly and reached 16.1 mm/s at 3000 Hz. The no-load speed can be further increased by further increasing the driving frequency above 3000 Hz. However, the piezoelectric stacks experienced a severe heating problem after operating for a period when the driving frequency was more than 3000 Hz at 100 $V_{p\text{-}p}$, which easily damaged the stacks. Thus, the highest working frequency was selected as 3000 Hz.

Then, the stepping displacement of the proposed actuator under the alternate-drive mode was measured as shown in Fig. 3-21. The applied voltages were 50, 75, and 100 $V_{p\text{-}p}$, and the corresponding preloads were 8.6, 12.3, and 20.8 N, respectively. The driving frequency of 1 Hz was selected. Every working cycle produced a forward slider displacement d_1 and a backward slider displacement d_2. According to the working principle of the alternate-drive mode, the sliders can be driven alternately by the dual stator without backward motion in an ideal state. However, it is impossible to maintain the same contact state between the sliders and driving feet on the dual stator because of

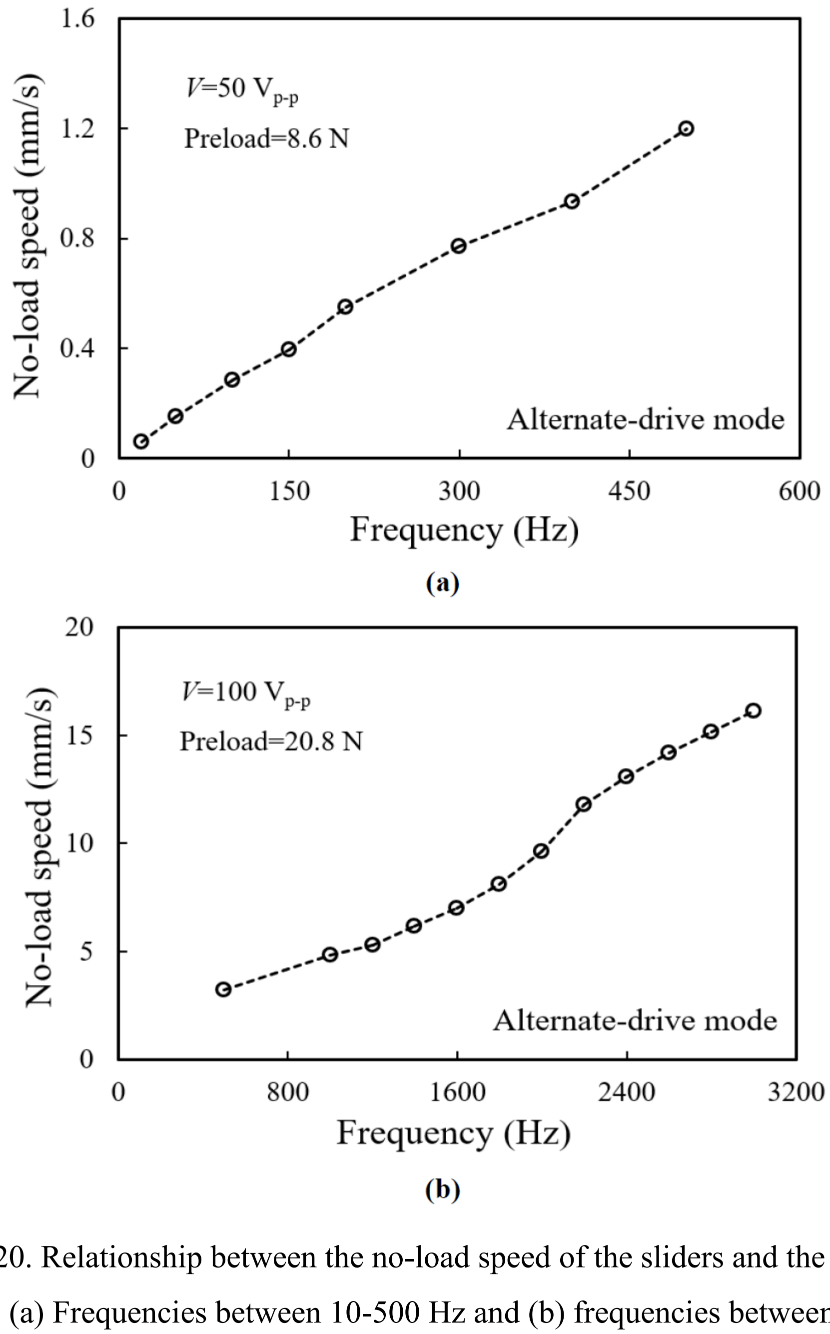

Fig. 3-20. Relationship between the no-load speed of the sliders and the driving frequency. (a) Frequencies between 10-500 Hz and (b) frequencies between 500-3000 Hz.

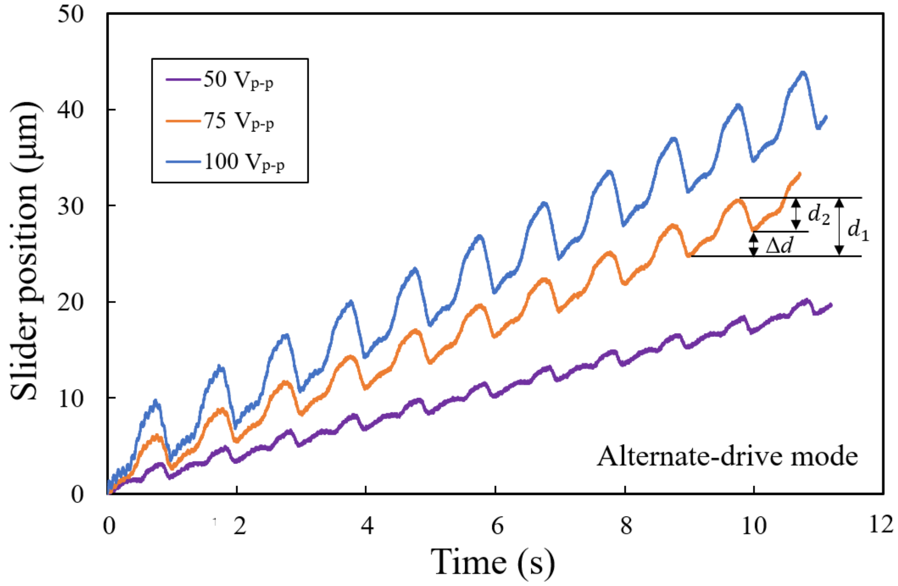

Fig. 3-21. Stepping displacements of the slider under the alternate-drive mode at applied voltages of 50, 75, and 100 $V_{p\text{-}p}$; preloads of 8.6, 12.3, and 20.8 N; and driving frequency of 1 Hz.

assembly errors. Therefore, when the driving feet on one stator finished driving the slider and entered the bottom half of the elliptical trajectory, the driving feet on the other stator could not contact and continue to drive the slider in time. This means that the static friction force may perform negative work in the driving process, resulting in the backward motion of the sliders. Thus, the stepping displacement Δd can be calculated by

$$\Delta d = d_1 - d_2. \tag{3-17}$$

The experimental results indicate that the proposed actuator can realize the stepping displacements of 1.8, 3.5, and 4.1 μm at the applied voltages of 50, 75, and 100 $V_{p\text{-}p}$, respectively. As more voltage was applied, the stepping displacement and driving duration increased because the higher voltage increased the driving friction and contact force between the driving feet and sliders.

As shown in Fig. 3-22, a string-pulley-weight system was added to evaluate the load characteristics of the proposed actuator under the alternate-drive mode. According to vary the weight, the speed of the slider at different loads was measured with a laser displacement sensor. The results are plotted in Fig. 3-23. The applied voltage, offset voltage, driving frequency, and preload were 50 $V_{p\text{-}p}$, 25 V, 500 Hz, and 8.6 N, respectively. The results show that the slider speed decreased almost linearly with increasing load, and the actuator was able to work stably under a load of 0 to 3 N. In addition, with reference to the characteristics of the no-load speed, it is expected that the load speed will also decrease with decreasing driving frequency.

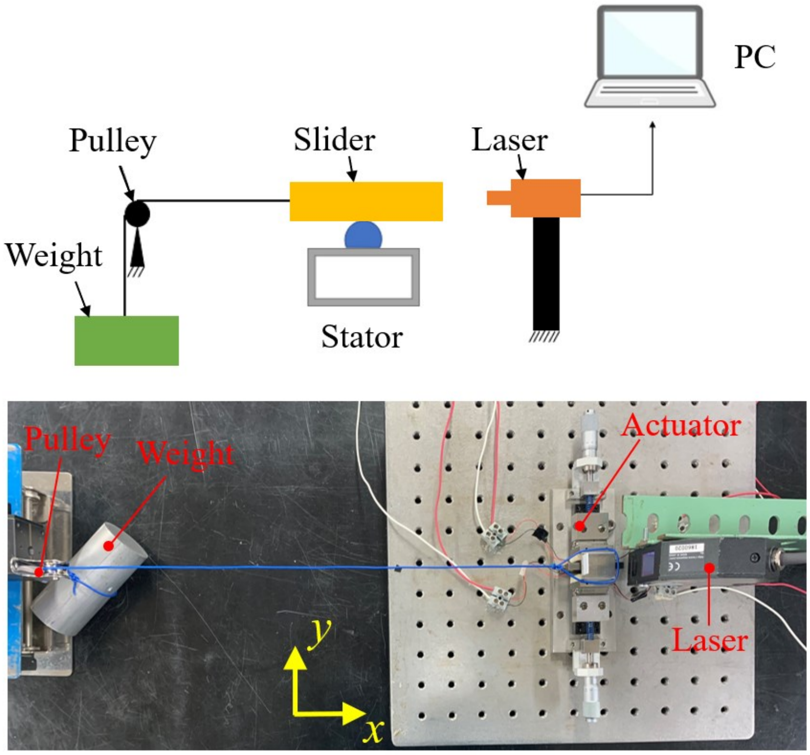

Fig. 3-22. String-pulley-weight system for evaluation of the load characteristics.

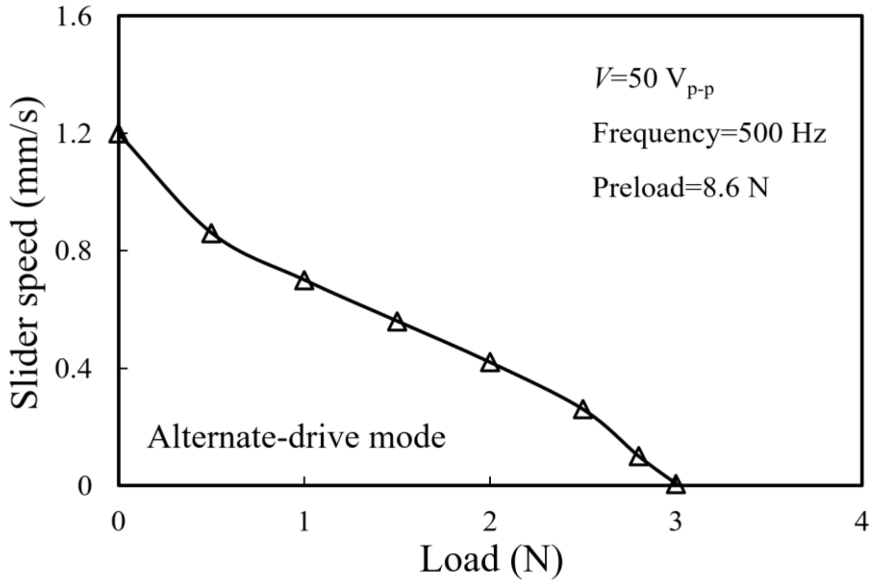

Fig. 3-23. Load characteristics of the actuator.

3.3.3 Performance test for the precision positioning mode

During the experiments, we found the minimum stepping voltage that could drive the slider to move a displacement was 4 V. Therefore, the stepping displacement of the slider under every 4 V stepping voltage could be regarded as the positioning resolution of the proposed actuator. From the experimental results shown in Fig. 3-24, the positioning resolutions of the forward and reverse motions were 156 and 172 nm, respectively. It indicated that the proposed actuator could realize the submicron-scale positioning.

The above experimental results illustrate that the proposed actuator is suitable for precision positioning applications. For example, thanks to the actuator's characteristics described in Table 3-2, the actuator can achieve the targets that the thrust is greater than 1 N, the no-load speed is slower than 0.5 mm/s, and the positioning resolution is submicron scale. Meanwhile, a gentle sinusoidal waveform voltage with low frequency can lead to less wear between the stator and slider. These specifications are similar to those used to drive the aperture of a scanning electron microscope used in semiconductor manufacturing. In addition, Table 3-3 summarizes and compares the performance of the maximum load and speed between the proposed actuator and the previously reported dual-stator actuators. It indicates that the proposed actuator with the dual stator can achieve higher speed and better loading capability than the previous actuators [74-77] under almost the same driving voltage, which is also expected to be used for driving the nozzle in a three-dimensional printer.

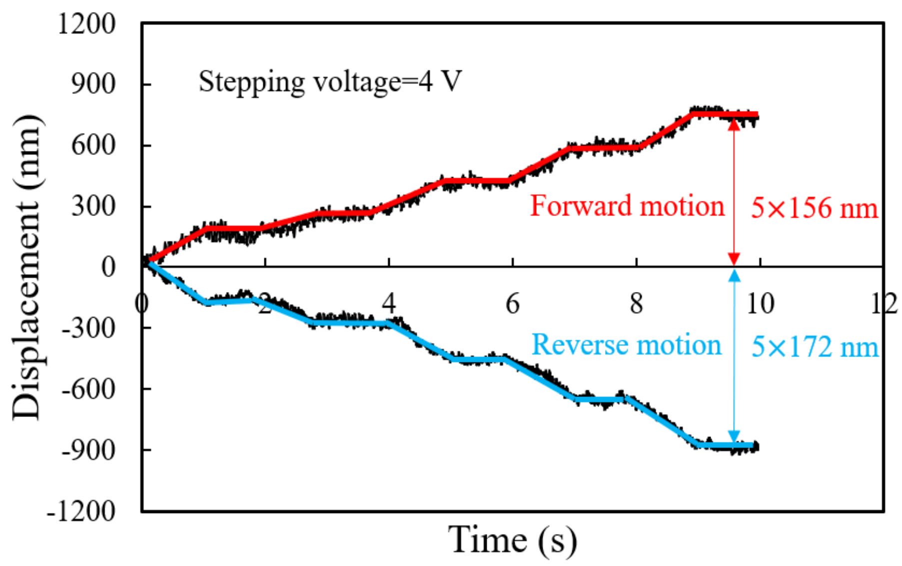

Fig. 3-24. Positioning resolutions of the forward and reverse motions.

Table 3-2. Characteristics of the proposed actuator under the voltage of 50 V_{P-P}.

	Voltage (V)	Frequency (Hz)	Speed (mm/s)	Load (N)	Positioning resolution (nm)	Wear phenomenon
Proposed actuator	50	1-500	0.0018-1.2	0-3	156, 172	Less wear
Specifications of aperture driving			Lower than 0.5 mm/s	Over than 1 N	High precision	No wear

Table 3-3. Comparison between some previous actuators and this work.

Reference	[74]	[75]	[76]	[77]	This work
Driving voltage (V)	100	120	100	100	100
Driving frequency (Hz)	800	400	5000	220	3000
Speed (mm/s)	16.7	1.1	6	2.3	16.1
Maximum load (N)	3	7	3.5	3.8	7.3

3.4 Improvement of the dual-side drive actuator

Above experimental results indicate the proposed dual-side drive walking-type piezoelectric linear actuator still exist fallback problems due to the assembly error of two stators and contact error between the driving feet and slider. This not only decreases the positioning accuracy and operating efficiency but also increases wear. Thus, the backward motion during the stepping process needs to be further suppressed.

In this study, to reduce contact error, the shape of the driving foot is improved first from semi-cylinder to hemisphere, which causes the contact type between the drive foot and the slider to be changed from line contact to point contact to reduce contact area, as shown in Fig. 3-25. A prototype based on the improved stator is manufactured for the experimental evaluation, as shown in Fig. 3-26.

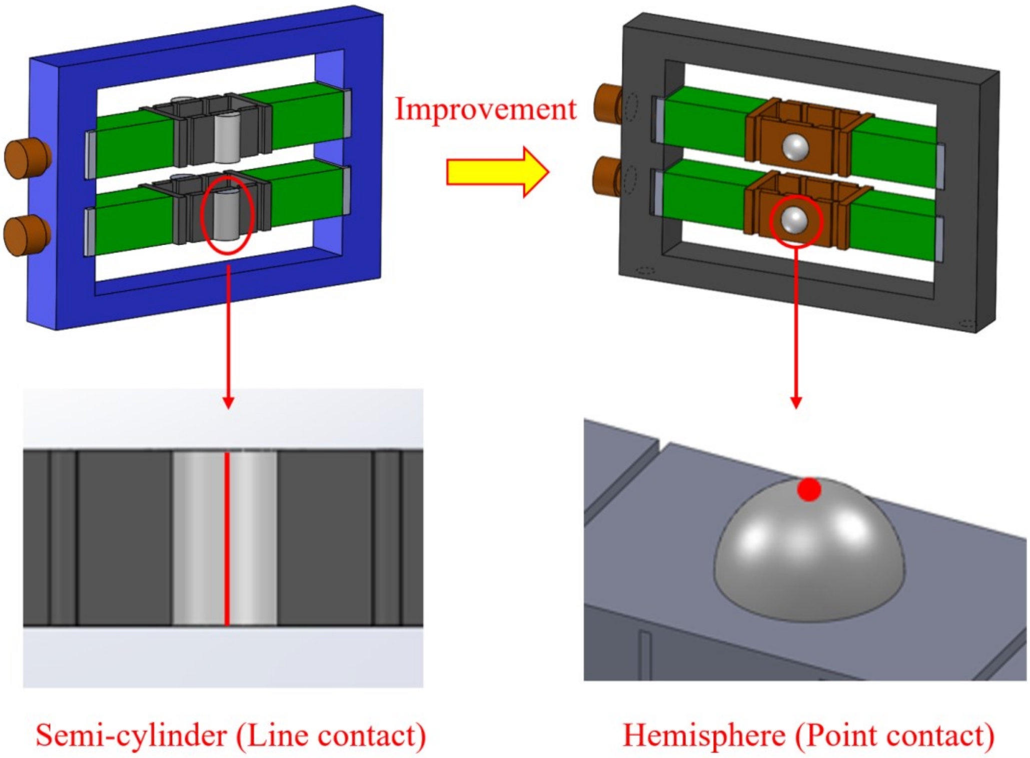

Fig. 3-25. Improvement for the shape of the driving foot.

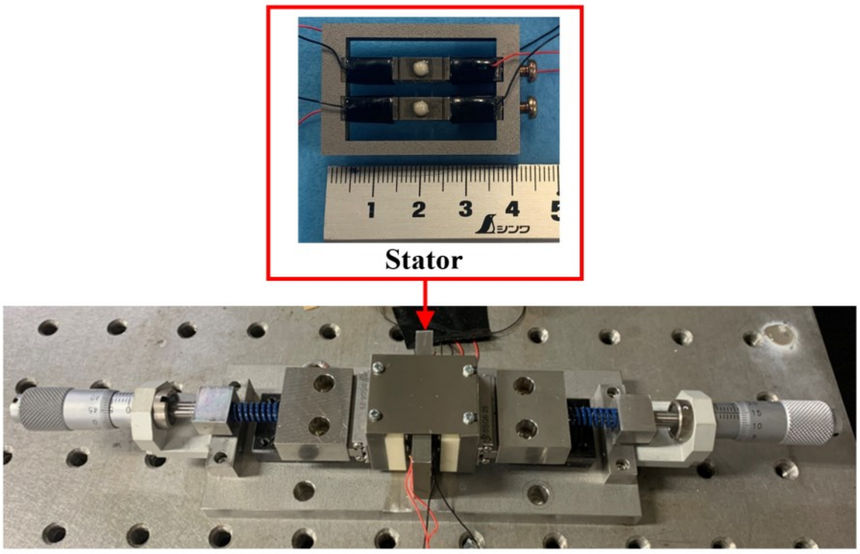

Fig. 3-26. Actuator prototype based on the improved stator

3.4.1 Stepping characteristic

The stepping characteristics of the actuator were further evaluated by the laser displacement sensor. When the driving voltage is 48 V_{p-p}, the frequency is 1 Hz, and the preload is 5.2 N, the measured results are plotted in Fig. 3-27. It can be seen that the backward motion has reduced compared to the dual-side drive actuator, but still cannot be completely suppressed.

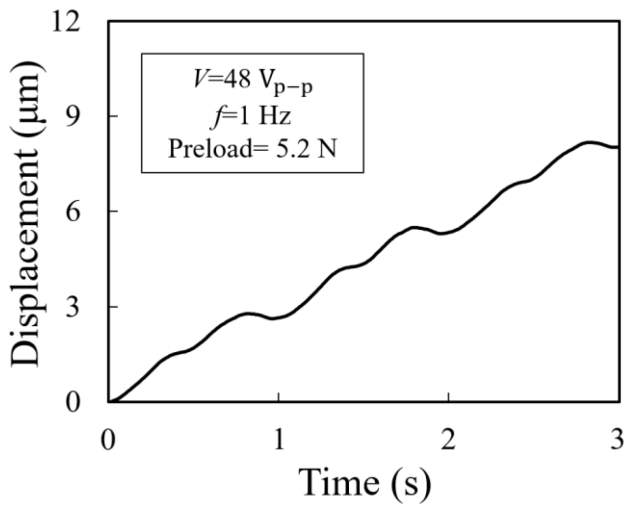

Fig. 3-27. Measured stepping displacements of the proposed actuator.

In the analysis of the operating principle, two stators of the actuator are considered to work in an ideal state. This means there is no assembly error between the stators and sliders. Thus, a stepping displacement free of backward motion can be achieved. However, assembly errors are impossible to be avoided during the experiments, which will result in the position difference Δd between two driving feet on the same side of two stators, as shown in Fig. 3-28. This causes the behavior that, under the same peak-peak voltages and bias voltages, when the driving feet on stator I (or II) finish driving the sliders and move into the bottom half of the elliptical trajectory, the driving feet on stator II (or I) cannot contact and drive sliders in time (From (a) to (b)). Accordingly, the driving feet on stator I (or II) won't be separated from the sliders in the bottom half of the elliptical trajectory and continue to drive the sliders to move in the reverse displacement x_2 until the driving feet on stator II (or I) contact the slider (From (b) to (c)). Then, due to the position difference between two driving feet, the driving feet on stator I (or II) will contact the slider the in the bottom half of the elliptical trajectory in advance (From (c) to (d)), and drive the sliders to move a backward displacement x_4 again (From (d) to (e)).

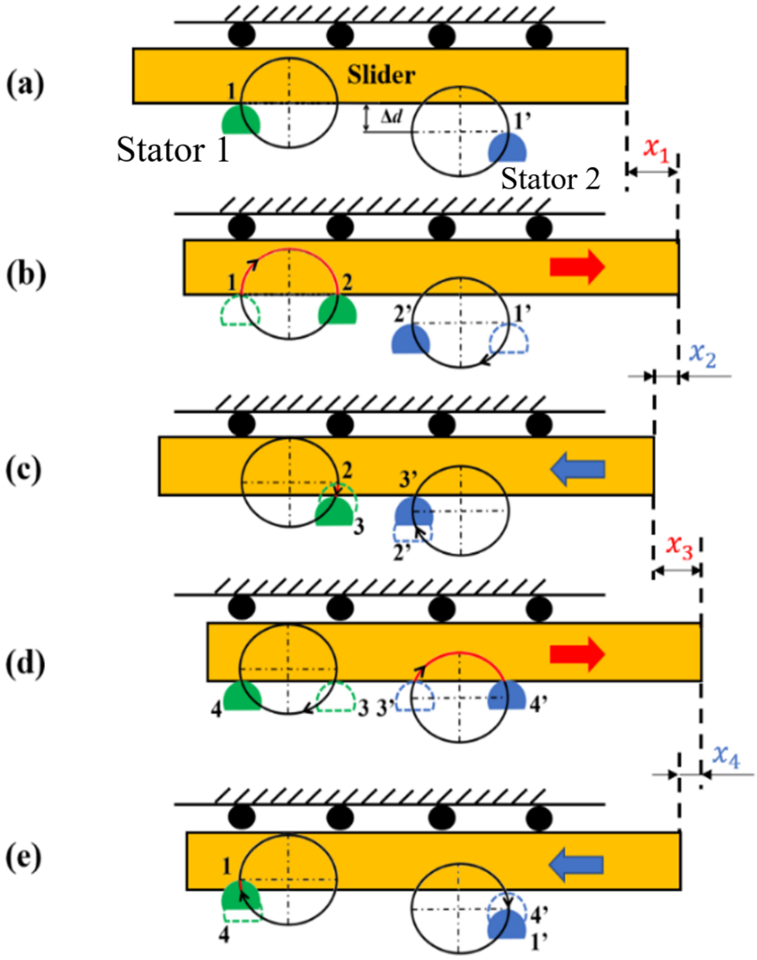

Fig. 3-28. Backward motion caused by assembly errors.

From the above analysis for the backward motion, it can be seen that the backward motion caused by assembly errors can be suppressed by reducing the position difference between two driving feet on the same side of two stators caused by assembly errors.

3.4.2 Backward motion suppression

Based on the characteristic of the piezoelectric stack, when two different bias voltages are applied to the piezoelectric stacks of two stators, the extensions of the piezoelectric stacks are different, which results in the different deformation of two flexible mechanisms in the normal direction. This means the positions of the driving feet on flexible mechanisms can be adjusted by varying the applied bias voltages. Thus, a solution to compensate for the position difference of the driving feet of two stators by correcting the bias voltages is proposed in this paper to reduce the backward motion.

Fig. 3-29 shows the improved voltage signal applied to four piezoelectric stacks. The peak-to-peak voltages applied to the two stators are the same, and there is a bias voltage difference ΔV between the two stators. During the experiments, by varying bias voltage difference ΔV, the relationships between the ΔV and backward displacement can be obtained as shown in Fig. 3-30. When the voltage is 48 Vp-p and the driving frequency is 1 Hz, compared with applying the same bias voltage to both stators ($\Delta V = 0$), the backward displacements are reduced by 68.1 % from 0.22 to 0.07 μm at the bias voltage difference of 14 V. It can be seen that the backward motion is effectively suppressed.

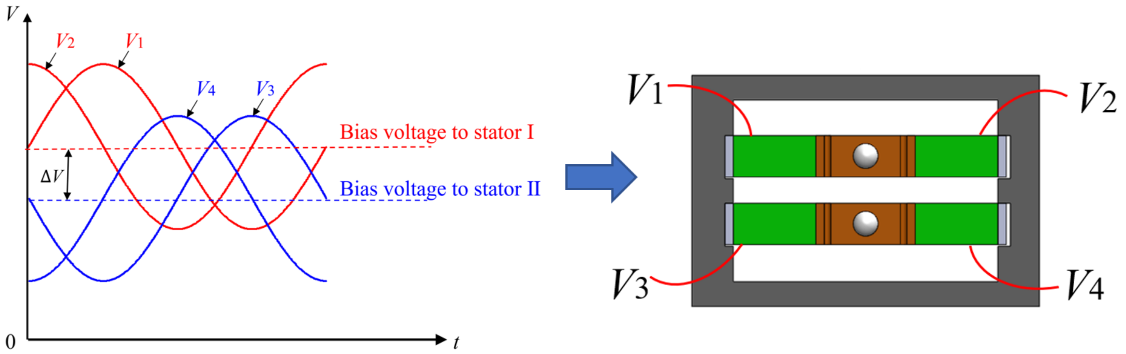

Fig. 3-29. Improved voltage signal.

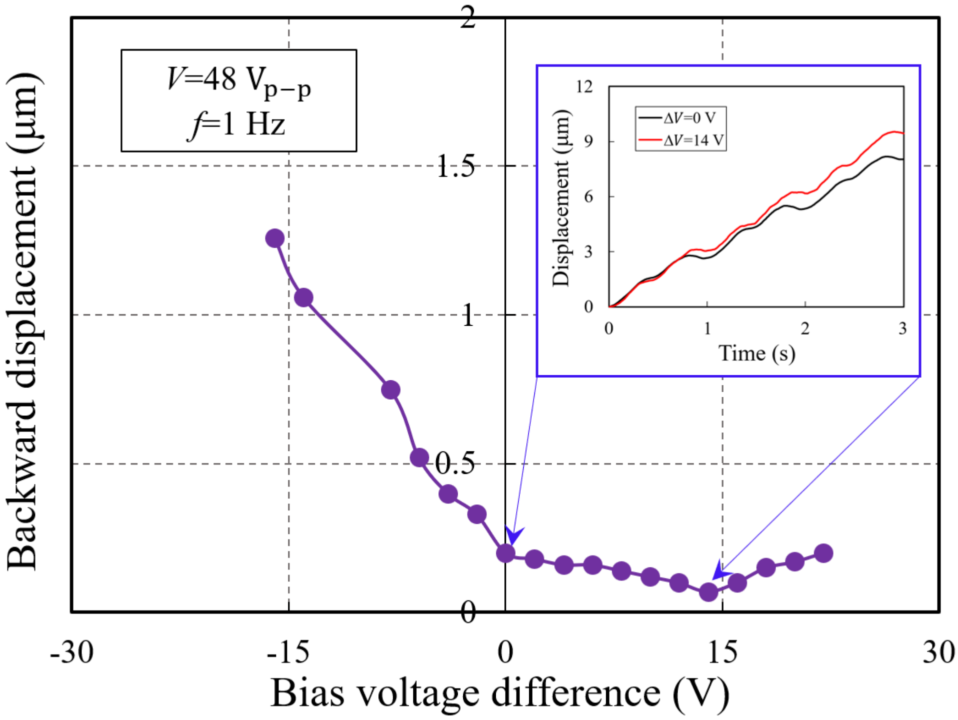

Fig. 3-30. Relationship between the ΔV and backward displacement.

3.5 Conclusion

1. To solve problems of the existing walking-type piezoelectric actuators and meet driving requirements of the aperture plate in the optical system of SEM. This chapter proposed a novel multi-drive-mode walking-type piezoelectric linear actuator with the parallel-arrangement dual stator. The operating principles and elliptical trajectory of the driving feet of a single-stator design were analyzed by a simplified geometric model.

2. A prototype was fabricated, and a series of experiments were tested to evaluate its output performance under three driving modes. The experimental results indicated that, under the alternate-drive mode, a no-load speed of 0.06 to 1.2 mm/s at driving frequencies of 10 to 500 Hz and a stepping displacement of 1.8 μm at 1 Hz were achieved. A maximum thrust of 7.3 N at 100 Hz and a maximum no-load speed of 16.1 mm/s at 3000 Hz were obtained. Moreover, under the precision positioning mode, the positioning resolutions of forward and reverse motions were 156 and 172 nm, respectively. However, the dual-side drive actuator shows a serious backward motion.

3. The improvement in the shape of the driving foot from semi-cylinder to hemisphere and a method of correcting the bias voltages were proposed to reduce the backward motion of the dual-side drive actuator. As a result, the backward motion was effectively improved, but cannot be completely suppressed.

Thus, the dual-side drive walking-type piezoelectric linear actuator still needs to be further improved.

4. Output characteristics simulation of the piezoelectric linear actuator based on dynamic models

4.1 Introduction

Chapter 3 proposed a dual-side drive walking-type piezoelectric actuator to achieve low speed with a large stroke, less wear, and high positioning resolution. The sliders of the actuator are driven by both sides of the two stators and a connecting plate is utilized to connect the sliders by 4 bolts, which leads to a large output thrust. However, it is difficult to ensure that the torques generated by four bolts are the same, leading to different preload on the two stators and contact errors. Thus, the dual-side drive actuator has a complex structure and a backward motion.

To solve the problems of the dual-side drive actuator, a novel stator structure with parallel-arrangement triangular-compliant mechanisms is further developed, as shown in Fig. 4-1. Compared to the stator of the dual-side drive actuator, only one side of the stator is used to drive the slider, the contact pairs are reduced from 4 to 2 pairs. Thus, the assembly and contact errors are expected to be improved. Based on the novel stator structure, the configuration of the single-side drive actuator is illustrated in Fig. 4-2.

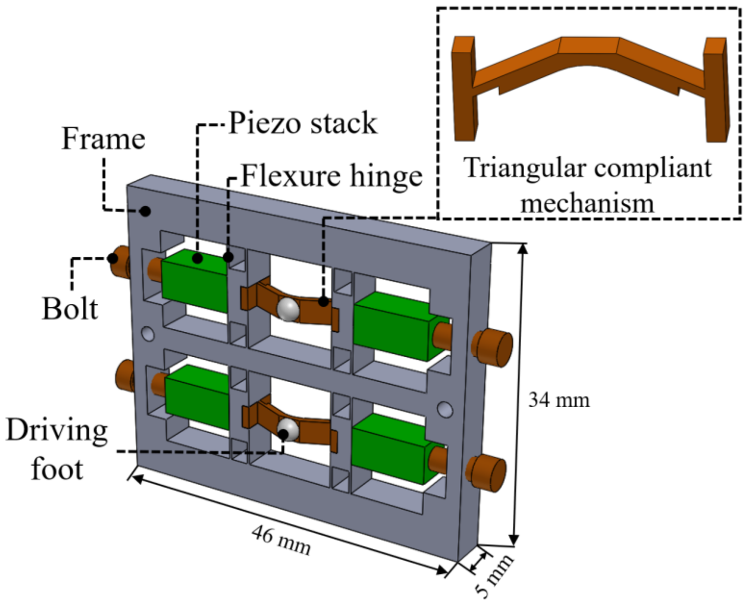

Fig. 4-1. Novel stator structure with parallel-arrangement triangular-compliant mechanisms.

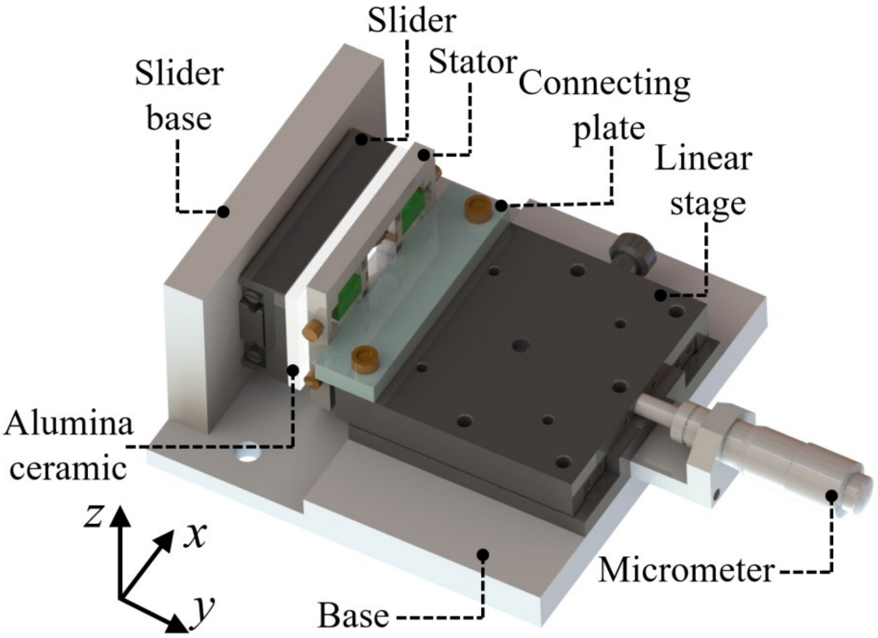

Fig. 4-2. Configuration of the single-side drive actuator based on the novel stator structure.

As known, the modeling system is always used to simulate the output performance of the system by analyzing system composition, external excitation, and disturbance, which is essential to improve the performance of the mechanical system [78-80]. Along with the development of the piezoelectric actuator, Li et al. and Wang et al. developed a dynamic model to simulate the displacement of the proposed stick-slip actuator [81,82]. Li et al. proposed a contact model for speed control of a standing wave linear ultrasonic motor [83]. However, a modeling system for analyzing the walking-type piezoelectric actuator has not been proposed.

This chapter introduces a dynamic model to evaluate the output characteristics of the single-side drive actuator to verify its feasibility. The performance of the actuator when using dual stator alternating drive and single stator drive are simulated, respectively.

4.2 Dynamic models of the single-side drive piezoelectric linear actuator

Based on the operating principle of the proposed actuator, the elliptical motion of the driving foot can be decomposed into motion in the *x*-direction (parallel to the slider) and motion in the *y*-direction (perpendicular to the slider). Thus, to evaluate the output characteristics of the proposed actuator, dynamic models in the *x*- and *y*-directions are established in this study.

4.2.1 Dynamic model in the *y*-direction

The proposed dual-stator structure is composed of two identical stators on the upper (stator I) and lower (stator II) halves. The *y*-direction dynamic model of each stator is shown in Fig. 4-3(a). The actuator can be considered to be a mass-spring-damper system. Figure 4-3(b) shows the interface model between the slider and the driving foot. Under a preload of F_c, the deformation of the friction layer $\delta = F_c/K_N$, where K_N is the normal elastic constant of the friction layer.

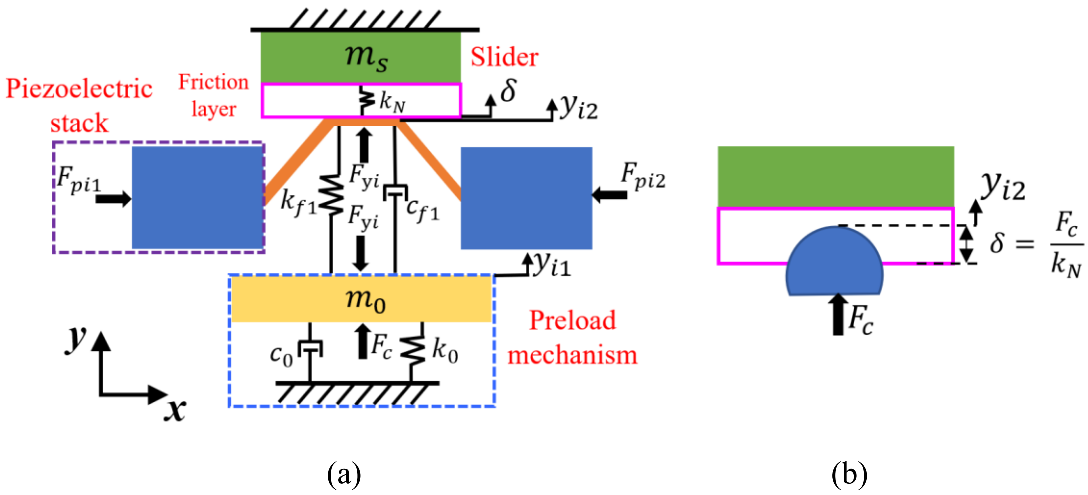

Fig. 4-3. (a) Dynamic model in *y*-direction and (b) interface model between slider and driving foot.

According to the force analysis, the dynamic model in the *y* direction can be represented as:

$$F_c - k_0 \cdot y_{i1} - C_0 \cdot \dot{y_{i1}} - (m_0 + m_f) \cdot \ddot{y_{i1}}$$
$$= F_{yi} + k_{f1} \cdot (y_{i1} - y_{i2}) + C_{f1} \cdot (\dot{y_{i1}} - \dot{y_{i2}}) \tag{4-1}$$

$$F_{yi} + k_{f1} \cdot (y_{i1} - y_{i2}) + C_{f1} \cdot (\dot{y_{i1}} - \dot{y_{i2}}) = F_{ni} + m_s \cdot \ddot{y_{i2}} \tag{4-2}$$

$$F_{ni}=\begin{cases} F_c+k_N\cdot y_{i2}, & y_{i2}+\frac{F_c}{k_N}>0 \text{ (Contact)} \\ 0, & y_{i2}+\frac{F_c}{k_N}\le 0 \text{ (Separation)} \end{cases} \tag{4-3}$$

where m_0, m_f, and m_s are the masses of the preload mechanism, triangular compliant mechanism, and slider, respectively; c_0 and c_{f1} are the y-direction equivalent damping coefficients of the preload mechanism and triangular compliant mechanism, respectively; and k_0 and k_{f1} are the y-direction equivalent stiffness of the preload mechanism and triangular compliant mechanism, respectively. To simplify the modeling process, the subscript i is utilized to represent the parameters of the two stators, where $i=1$ and 2 denote parameters related to stators I and II, respectively. y_{i1} and y_{i2} are the y-direction displacements of the preload mechanism and driving foot, respectively, F_{yi} is the y-direction force generated by the triangular compliant mechanism, and F_{ni} is the normal force applied to the slider. When the condition $y_{i2}+\frac{F_c}{k_N}\le 0$ is satisfied, the driving foot is separated from the slider. F_{pi1} and F_{pi2} are the output force generated by two piezoelectric stacks, respectively, of each stator.

A simplified analytical model of the triangular compliant mechanism is proposed for calculating the y-direction force F_{yi}, as shown in Fig. 4-4. Based on the moment balance of AC and BC (see Fig. 4), F_{yi} can be derived as:

$$F_{yi}=\left(F_{pi1}\cdot tan\theta+F_{pi2}\cdot tan\theta\right)\cdot\gamma \tag{4-4}$$

where γ is a loss factor. The compliant mechanism leads to losses during force transmission. Accordingly, loss factor γ, which is obtained from a static analysis using the finite element method, is utilized to correct the force F_{yi}.

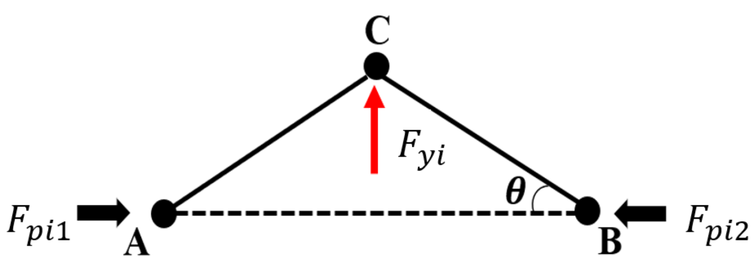

Fig. 4-4. Simplified triangular analytical model of triangular compliant mechanism.

The output force generated by the piezoelectric stacks can be written as:

$$\begin{cases} F_{pi1} = nd_{33}V_{i1}k_p \\ F_{pi2} = nd_{33}V_{i2}k_p \end{cases} \tag{4-5}$$

where n, d_{33}, and V_{i1}-V_{i2} are the number of PZT ceramic layers, piezoelectric strain coefficient, and applied driving voltage signals to piezoelectric stacks, respectively.

4.2.2 Dynamic model in the *x*-direction

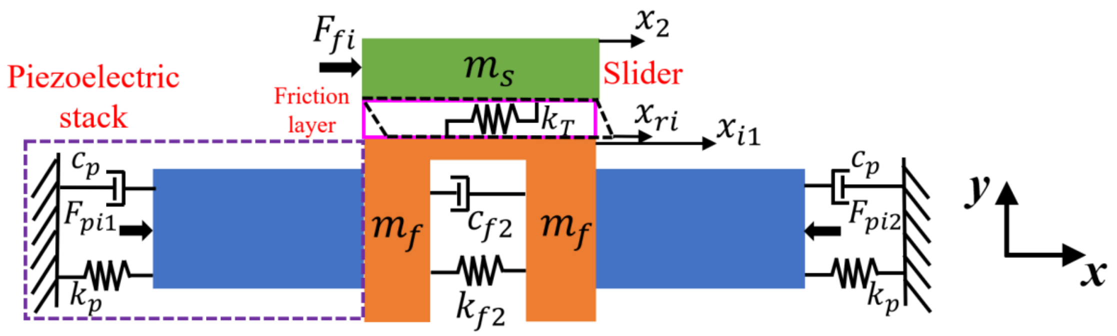

Fig. 4-5. Dynamic model of the actuator in the *x*-direction.

The derived *x*-direction dynamic model is shown in Fig. 4-5. Based on the force analysis and a previous study [84], the dynamic model of the actuator in the *x*-direction is given by:

$$(F_{pi1} - F_{pi2}) - 2(k_p + k_{f2})x_{i1} - 2(c_p + c_{f2})\dot{x_{i1}} - 2m_f \cdot \ddot{x_{i1}} = F_{fi} \tag{4-6}$$

$$F_{fi} = \begin{cases} \mu_d F_{ni}\, sgn(\dot{x_{i1}} - \dot{x_2}), & \dot{x_{i1}} \neq \dot{x_2} \text{ (slip phase)} \\ k_T x_{ri}, & \dot{x_{i1}} = \dot{x_2} \text{ (stick phase)} \end{cases} \tag{4-7}$$

$$c_{loss}\dot{x_2} + m_s\ddot{x_2} = F_{f1} + F_{f2} \tag{4-8}$$

where x_{i1}, x_2, and x_{ri} are the *x*-direction displacements of the driving foot, slider, and contact surface of the friction layer, respectively. k_p and k_{f2} are the equivalent stiffness of the *x*-direction equivalent stiffness of the piezoelectric stack and triangular compliant mechanism, respectively; c_p and c_{f2} are the *x*-direction equivalent damping coefficients of the piezoelectric stack and triangular compliant mechanism, respectively; and F_{fi} is the friction force experienced by the slider. The system is identified as being in the stick phase if the velocities of the driving foot and slider satisfy the condition $\dot{x_{i1}} = \dot{x_2}$; otherwise, it is identified as being in the slip phase. In the stick phase, interface friction F_{fi} is proportional to displacement of the contact surface x_{ri} with tangential elastic constant of the friction layer k_T. In the slip phase, F_{fi} is calculated based on the Coulomb model. μ_d is the dynamic coefficient and c_{loss} is the equivalent damping coefficient between the slider and stator.

4.3 Simulation and discussion

The Runge–Kutta method was utilized to solve the above-mentioned dynamic models. The values of the parameters used in the dynamic models are listed in Table 4-1.

Table 4-1. Parameters in dynamic model.

Parameter	Value	Parameter	Value
Number of PZT ceramic layers $\boldsymbol{n}$	100	Equivalent stiffness of the preload mechanism $\boldsymbol{k_0}$	13000 N/m
Piezoelectric strain coefficient $\boldsymbol{d_{33}}$	650e-12 m/V	Normal elastic constant of the friction layer $\boldsymbol{k_N}$	1.23e9
Mass of the preload mechanism $\boldsymbol{m_0}$	0.28 kg	Tangential elastic constant of the friction layer $\boldsymbol{k_T}$	2.5e10
Mass of the compliant mechanism $\boldsymbol{m_f}$	0.0015 kg	Equivalent damping coefficient of the piezoelectric stack $\boldsymbol{c_p}$	60 N·s/m
Mass of the slider $\boldsymbol{m_s}$	0.2 kg	Equivalent damping coefficient of the compliant mechanism $\boldsymbol{c_{f1}}$	100 N·s/m
y-direction equivalent stiffness of the compliant mechanism $\boldsymbol{k_{f1}}$	8.1e6 N/m	Equivalent damping coefficient of the compliant mechanism $\boldsymbol{c_{f2}}$	180N·s/m
x-direction equivalent stiffness of the compliant mechanism $\boldsymbol{k_{f2}}$	11.1e7 N/m	Equivalent damping coefficient of the preload mechanism $\boldsymbol{c_0}$	40 N·s/m
Equivalent stiffness of the piezoelectric stack $\boldsymbol{k_p}$	60e6 N/m	Equivalent damping coefficient between the slider and stator $\boldsymbol{c_{loss}}$	15 N·s/m

4.3.1 Simulation using single stator

The proposed dynamic models can be used to evaluate the output characteristics of the actuator when using a single-stator drive or dual-stator opposite-phase drive. Here, the single-stator drive has the same effect as a dual-stator in-phase drive. The output characteristics of the actuator under single-stator drive were first simulated. The phase difference between the voltages applied to the two piezoelectric stacks on the single stator was 90°.

The velocity of the slider is related to the driving frequency. Thus, the output characteristics of the actuator under low (1 Hz) and high (10 kHz) frequencies were simulated using the dynamic models, respectively. The results for the low frequency (1 Hz) are shown in Fig. 4-6. The applied voltage was 72 V_{pp} and the preload was 3 N. Fig. 4-6(a) indicates that the normal force applied to the slider was always greater than 0, which means that the driving foot was not separated from the slider during operation. This is considered to be caused by a small normal acceleration of the driving foot at 1 Hz. Fig. 4-6(b) shows the contact separation characteristics between the slider and the driving foot, where the numbers 1, 2, and 3 denote the stick phase, slip phase, and separation, respectively. The results indicate that only the stick phase occurred during contact. Thus, the slider showed the same motion as that of the driving foot in the *x*-direction. The velocity and displacement characteristics of the slider are shown in Figs. 4-6(c) and (d), respectively. As shown, the actuator made a reciprocating motion rather than a linear motion.

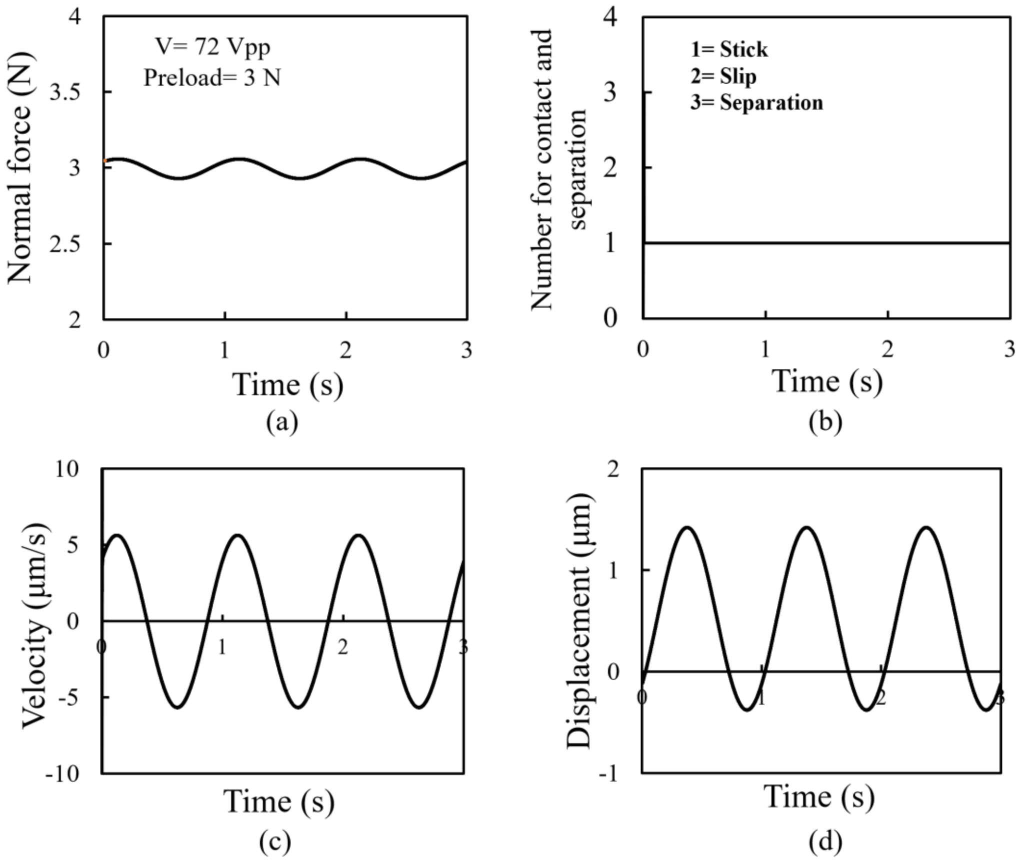

Fig. 4-6. Output characteristics of actuator operating at 1 Hz. (a) Normal force applied to slider, (b) contact separation characteristics, (c) velocity characteristics, and (d) displacement characteristics.

The results for the high frequency (10 kHz) are shown in Fig. 4-7. The applied voltage was 72 V_{pp} and the preload was 3 N. As shown in Fig. 4-7(a), a steady velocity was obtained after a short startup time, which means that a linear movement of the slider was achieved. Figs. 4-7(b), (c), and (d) show the normal force, contact separation, and driving force in the steady state, respectively. It can be seen that, at 10 kHz, the driving foot was able to separate from the slider and the slip phase was dominant between the slider and stator during contact.

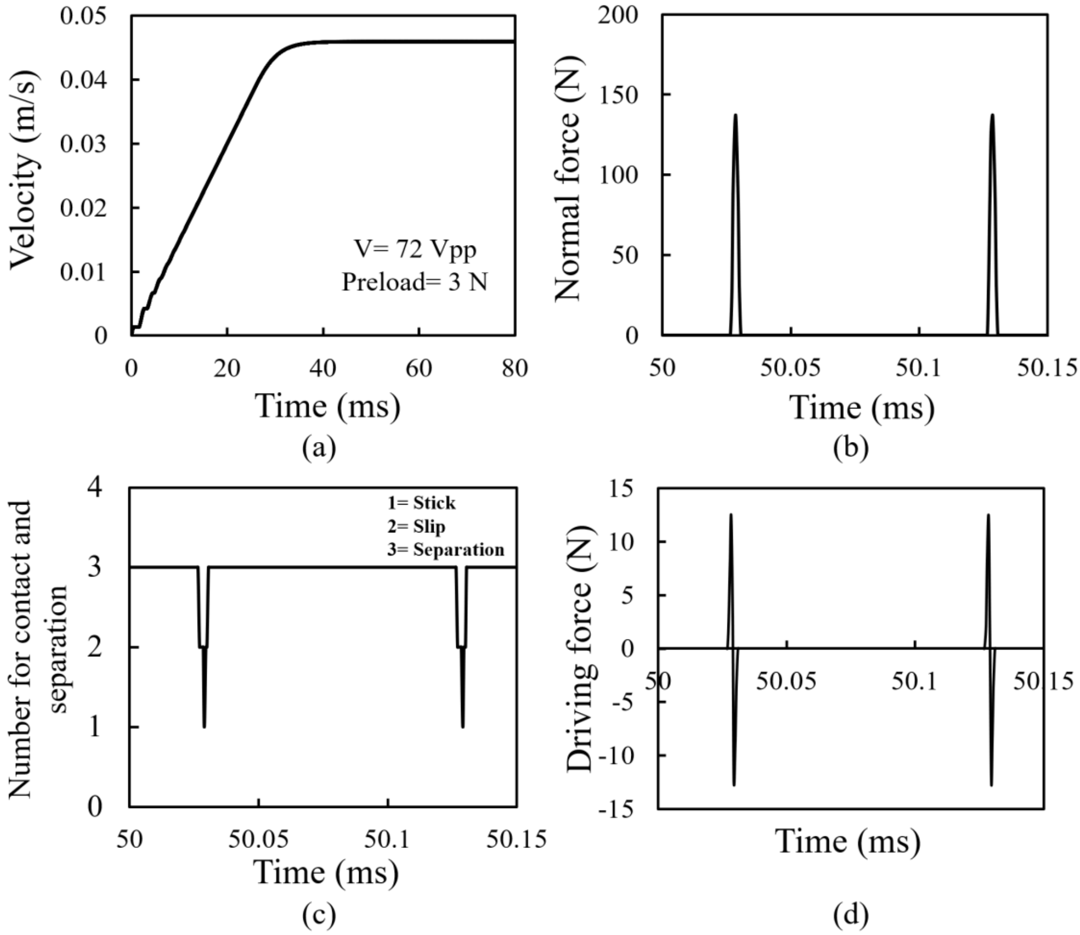

Fig. 4-7. Output characteristics of actuator operating at 10 kHz. (a) Velocity characteristics, (b) normal force applied to slider, (c) contact separation characteristics, and (d) driving force.

The above analysis results indicate that a steady linear motion was achieved at high frequency when utilizing a single stator. Thus, the no-load velocity and load characteristics with various preload values were simulated. The results are plotted in Fig. 4-8. The applied voltage was 72 V_{pp} and the frequency was 10 kHz. As shown in Fig. 4-

8(a), the velocity of the slider increased as the preload increased from 1 to 10 N. This was due to the fact that the normal force applied to the slider increased with increasing preload, leading to an increase in the driving force. However, when the preload was further increased from 10 to 20 N, the contact duration between the slider and stator was extended. The driving foot could not effectively separate from the slider, causing a decrease in velocity. Moreover, Fig. 4-8(b) shows that the load characteristics improved as the preload increased from 3 to 20 N.

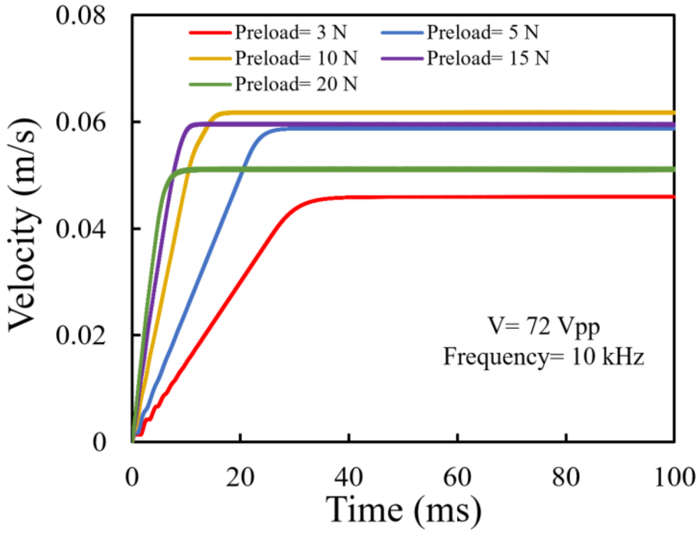

(b)

Fig. 4-8. Output characteristics for various preload values. (a) Transient response of no-load velocity and (b) load characteristics.

4.3.2 Simulation using dual stator

The output characteristics of the actuator with dual-stator opposite-phase drive were simulated. The phase difference between adjacent voltages applied to the four piezoelectric stacks on the two stators was 90°. Fig. 4-9 shows the displacement characteristic of the slider at a frequency of 1 Hz. Compared with the reciprocating motion of the slider obtained using a single stator, step displacements without backward motion were realized under various applied voltages. This is because when the driving foot on one stator finishes driving the slider and moves into the bottom half of its elliptical trajectory, the driving foot on the other stator contact and drive the slider. Accordingly, the driving foot on the first stator is separated from the slider in the bottom half of its elliptical trajectory; that is, it does not continue to drive the slider in the reverse (backward) direction.

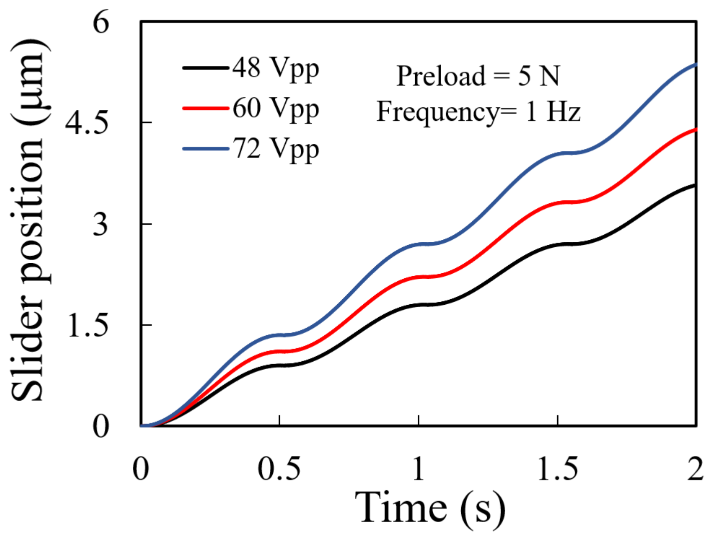

Fig. 4-9. Step characteristics under various driving voltages.

Fig. 4-10 shows a comparison of the no-load velocity and load characteristics between single- and dual-stator configurations for a driving frequency of 10 kHz. As shown in Fig. 4-10(a), under the same driving conditions, compared with the single-stator driving, the startup time of the actuator was halved when driven alternately by the dual stator. In addition, Fig. 4-10(b) indicates that the maximum load capacity of the actuator with the dual stator is almost twice that of the actuator with a single stator under the same driving conditions. Hence, it can be seen that the performance of the actuator is superior when alternately driven by a dual stator than by a single stator.

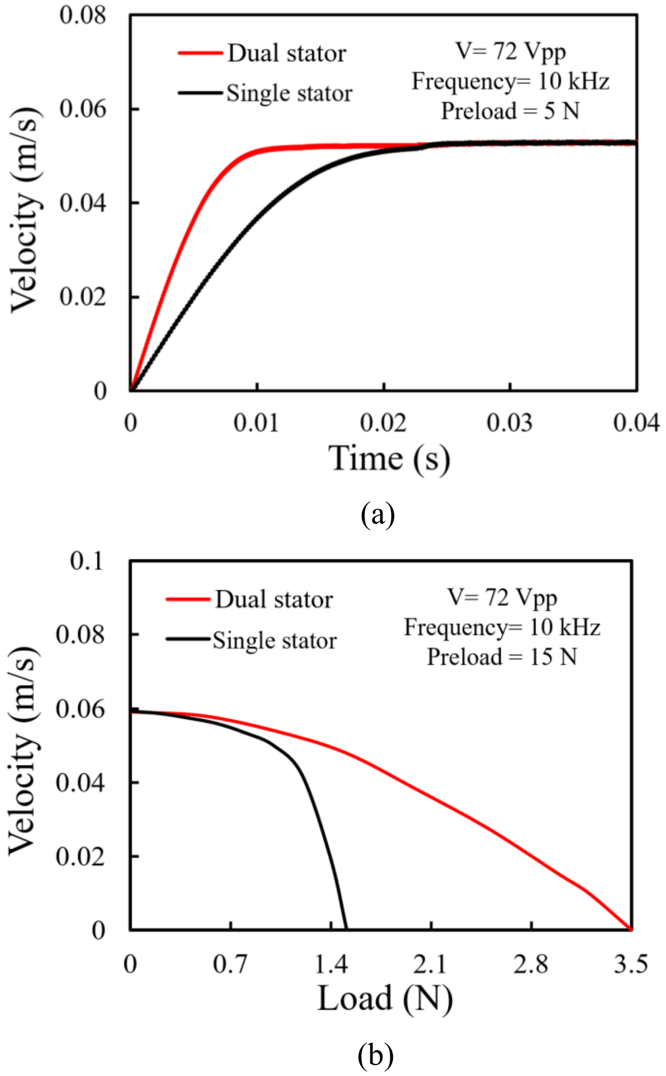

Fig. 4-10. Comparison of characteristics between single- and dual -stator configurations. (a) Transient response of no-load velocity and (b) load characteristics.

To verify the feasibility of the dynamic model, a prototype of the single-side drive actuator is fabricated and evaluated. The experimental results are compared with the simulation results in Chapter 5.

4.4 Conclusion

1. A novel stator structure with parallel-arrangement triangular-compliant mechanisms was developed to solve the problems of the dual-side drive actuator.

2. To verify the feasibility of the single-side drive actuator, dynamic models of the actuator in x and y direction were established, respectively.

3. The performance of the single-side drive actuator when using dual stator alternating drive and single stator drive were simulated by the proposed dynamic models, respectively. Simulated results indicate that whether at low or high frequencies, the performance of the actuator is superior when alternately driven by dual stator than by a single stator. Specifically, the step displacement without backward motion at 1 Hz and a better load capacity at 10 kHz were realized when the actuator was driven alternately by the dual stator.

5. Single-side drive walking-type piezoelectric linear actuator with triangular compliant mechanism

5.1 Introduction

In Chapter 4, a single-side drive stator structure with triangular-compliant mechanisms was proposed to address the issue of backward motion in the dual-side drive actuator. To validate the effectiveness of this design, dynamic models were developed in both the x and y directions to simulate the output characteristics of the single-side drive actuator. Simulated results indicate the single-side drive actuator was capable of achieving a step displacement without backward motion.

To further verify the feasibility of the proposed dynamic models, this chapter first introduces the structure and operating principle of the single-side drive actuator. Then, a prototype of the single-side drive actuator is fabricated, and a series of experiments are conducted to evaluate its velocity, stepping, and precision positioning characteristics. Finally, the experiential results are compared with the simulation results obtained from the dynamic models.

The single-side drive actuator effectively eliminates the backward motion and satisfies the driving needs of the aperture plate in SEM. With further miniaturization optimization, it has promising potential for industrial applications in the future.

5.2 Structure design and operating principle

5.2.1 Structure

As shown in Fig. 5-1(a), the stator of the proposed actuator is composed of a frame, four piezoelectric stacks, two triangular compliant mechanisms, and two driving feet. The piezoelectric stacks, as the driving elements, are secured to the frame by bolts and the triangular compliant mechanisms are embedded into the middle grooves of the frame. The flexure hinge is designed to guide the linear motion of the piezoelectric stack. The dimensions of the stator are 46 mm × 34 mm × 5 mm. The configuration of the proposed actuator, which is based on the stator structure, is shown in Fig. 5-1(b). The connecting plate is used to connect the stator and linear stage with bolts. The slider is fixed on a slider base to output linear motion in the *x*-direction. A micrometer head is arranged to provide and adjust the preload between the slider and stator along the *y*-direction. All parts are assembled on a base.

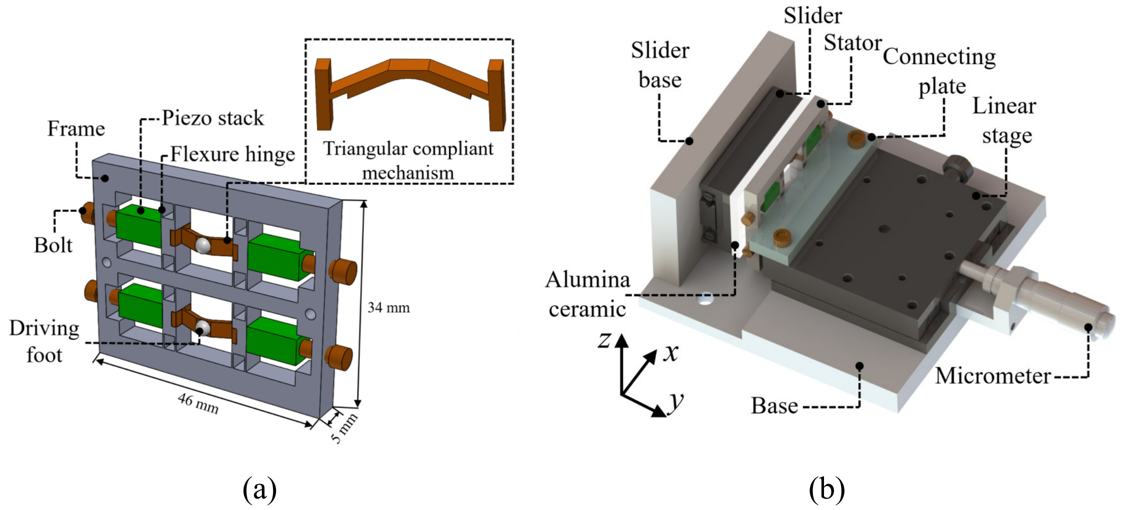

Fig. 5-1. (a) Stator structure and (b) configuration of proposed actuator.

5.2.2 Operating principle

The operating principle of the single-side drive actuator is similar to that of the dual-side drive actuator. The triangular compliant mechanisms of the stator easily deform when the piezoelectric stacks extend. This generates motion of the driving feet to drive the slider. The voltage signals applied to the four piezoelectric stacks are shown in Fig. 5-2(a). The phase difference between adjacent applied voltages (V_1 to V_4) is 90°. As a result, two driving feet on the triangular compliant mechanisms make alternating elliptical movements with a half-cycle difference. Thus, the applied voltages can be divided into two stages that correspond to two operation processes in one working cycle. The detailed driving principle is shown in Fig. 5-2(b). Here, the driving feet placed on the upper and lower two triangular compliant mechanisms are denoted as driving foot I and driving foot II, respectively.

First, from time 0 to t_0, driving foot I moves into the upper half of the elliptical trajectory under voltages V_1 and V_2 and contacts and drives the slider to move by a displacement d_1 via a friction force. Meanwhile, driving foot II moves into the lower half of the elliptical trajectory under voltages V_3 and V_4 and is separated from the slider.

Then, from time t_0 to t_1, the two driving feet reverse roles after they reach the two vertices of the elliptical trajectory. This means that driving foot II moves into the upper half of the elliptical trajectory and continues to drive the slider to move by a displacement d_2 under voltages V_3 and V_4, while driving foot I is separated from the slider under voltages V_1 and V_2. The slider is thus driven twice in one operating cycle. Therefore, by repeating the above processes, the slider of the proposed actuator can achieve a large stroke movement.

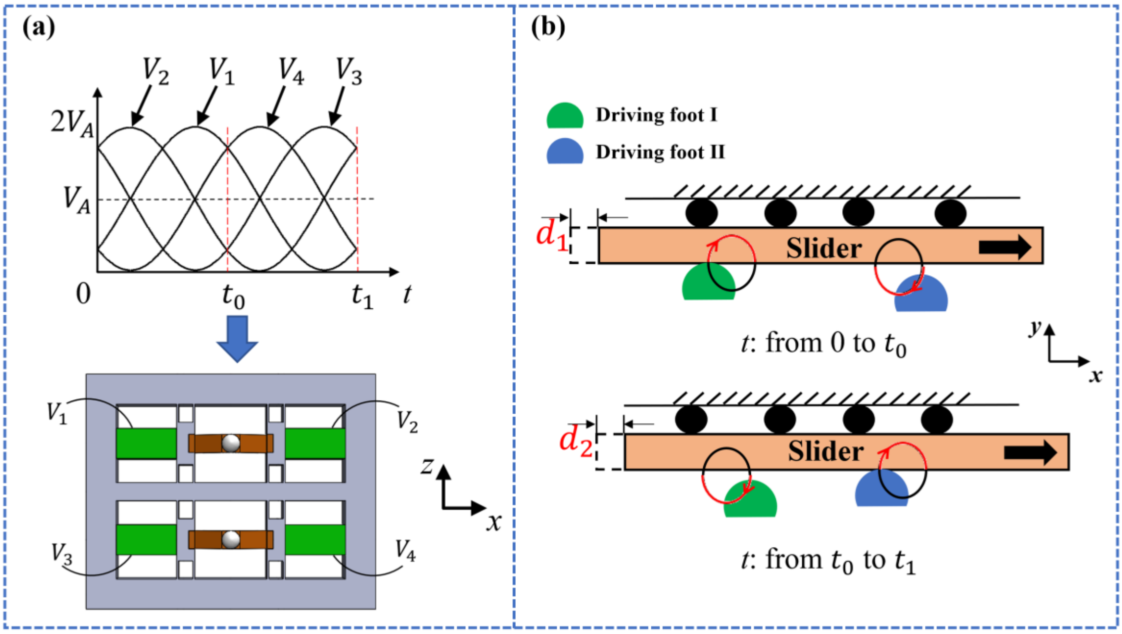

Fig. 5-2. Operating principle of proposed actuator. (a) Voltage signals applied to four piezoelectric stacks and (b) corresponding movement of driving feet.

5.2.3 Design of the triangular compliant mechanisms

From the analysis of the working principle, it is clearly seen that the normal displacement and equivalent stiffness of the triangular-compliant mechanism are important parameters that affect the output characteristics and stability of the actuator, while the parameter of angle θ of the triangular-compliant mechanism significantly influences normal displacement and equivalent stiffness. Thus, the angle θ should be further designed. In this study, the static structural analysis employing the finite element method is utilized to investigate the effects of different angles θ on the normal displacement and equivalent stiffness. During the static structural analysis, triangular-compliant mechanisms with angles ranging from 10-60° are selected, as shown in Fig. 5-3, and a displacement constraint of 5 μm is applied to both sides of the triangular-compliant mechanism, as illustrated in Fig. 5-4. Under these boundary conditions, the normal displacement y and force F can be directly obtained from the simulation, while the normal equivalent stiffness k can be calculated by

$$k = \frac{F}{y} \tag{5-1}$$

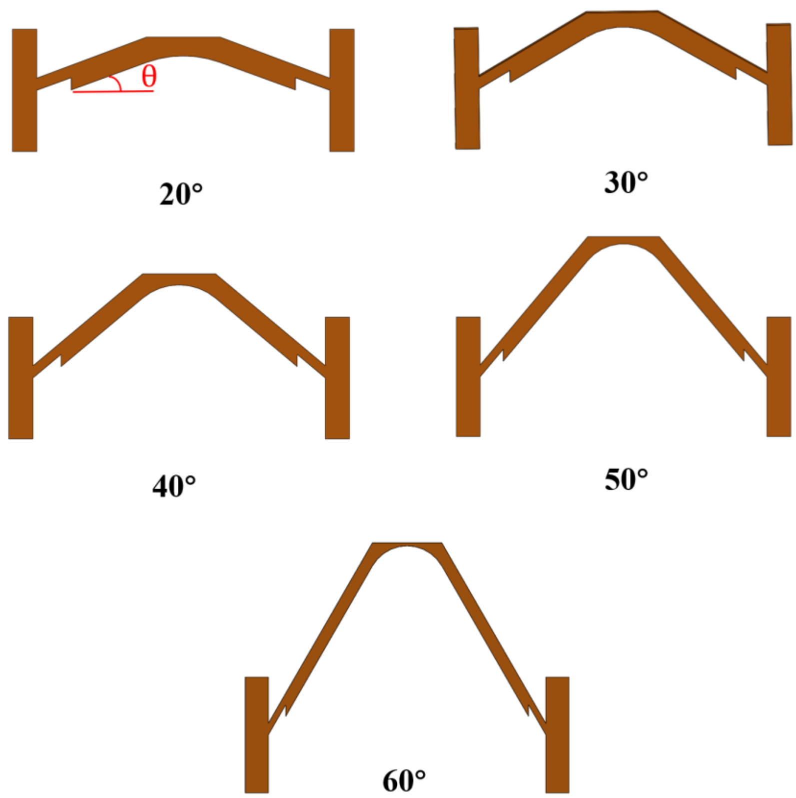

Fig. 5-3. Triangular-compliant mechanisms with different angles θ.

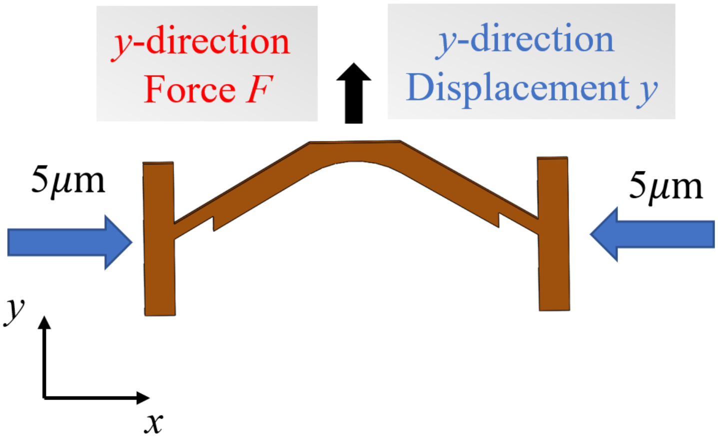

Fig. 5-4. Displacement constraint applied to both sides of the triangular-compliant mechanism.

The simulation results are shown in Fig. 5-5. It can be seen that as the angle θ increases, the normal displacement y decreases and the equivalent stiffness k first increases and then decreases. Here, the selection criteria is to ensure a sufficiently large normal displacement and stiffness. Thus, the angle θ of 30° is chosen.

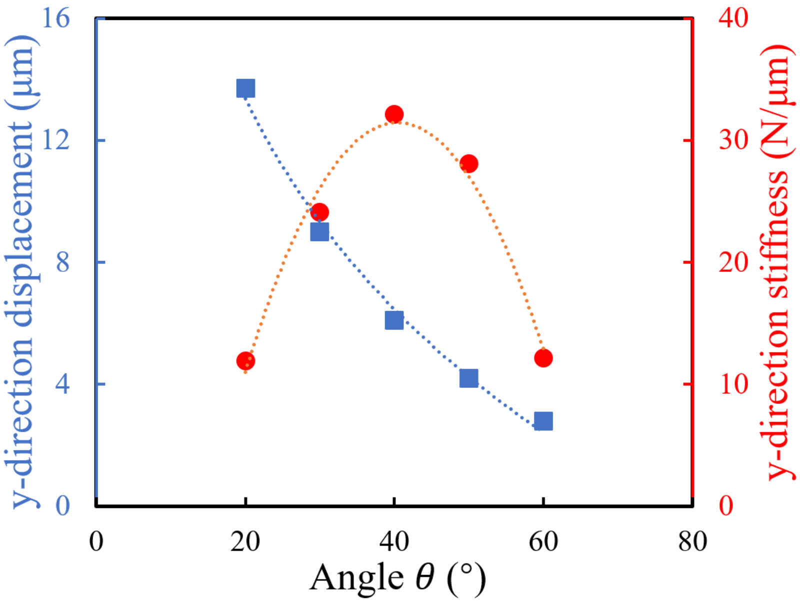

Fig. 5-5. Simulation results of normal displacement y and equivalent stiffness k with respect to angle θ.

5.3 Experiments and discussion

5.3.1 Prototypes of the stator and actuator

The prototypes of the stator and actuator were manufactured, as shown in Fig. 5-6. Stainless steel was selected as the material for the base, connecting plate, and frame. A cross-roller table (VRT2050, THK Co.) and a linear stage (XSG60, MISUMI Co.) were used. Piezoelectric stacks (5 mm × 5 mm × 5 mm) made by NIKKO were used.

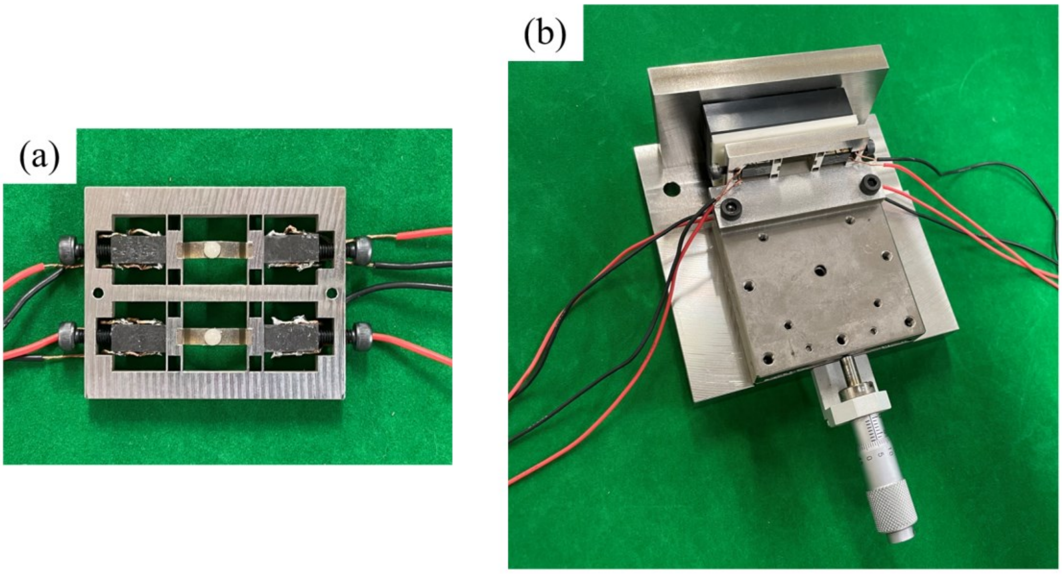

Fig. 5-6. Prototypes of the stator and actuator. (a) Stator prototype and (b) actuator prototype.

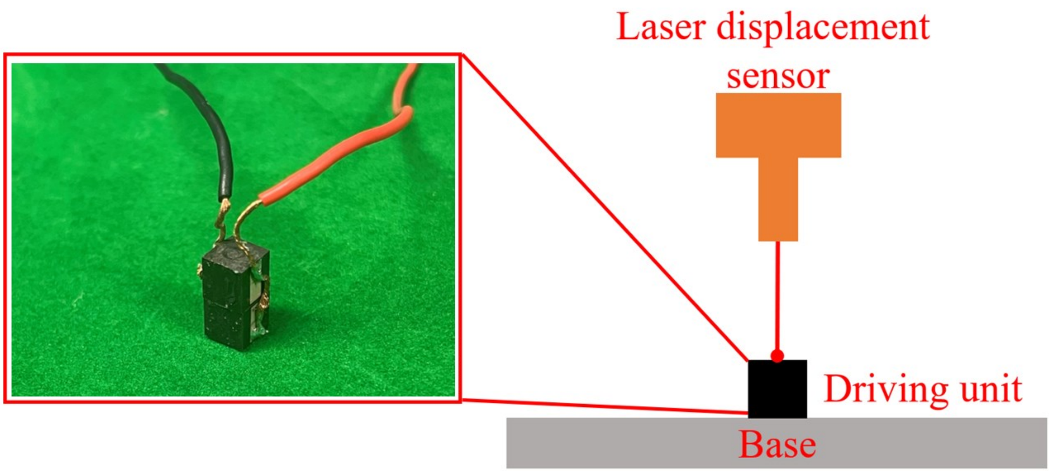

Fig. 5-7. Measurement method for the amplitude characteristic of the driving unit.

The stator includes 4 driving units, each of which consists of two piezoelectric stacks glued together with epoxy adhesive. Before assembling the stator, it is necessary to ensure that all four driving units show the same working performance. Therefore, we first tested the amplitude characteristic of each unit by using a laser displacement sensor with the same sinusoidal voltage, as shown in Fig. 5-7; the tested results are plotted in Fig. 5-8. All four drive units exhibited almost the same amplitude at driving frequencies of 1 Hz and 10 Hz. Thus, they can be utilized as the driving components in the stator.

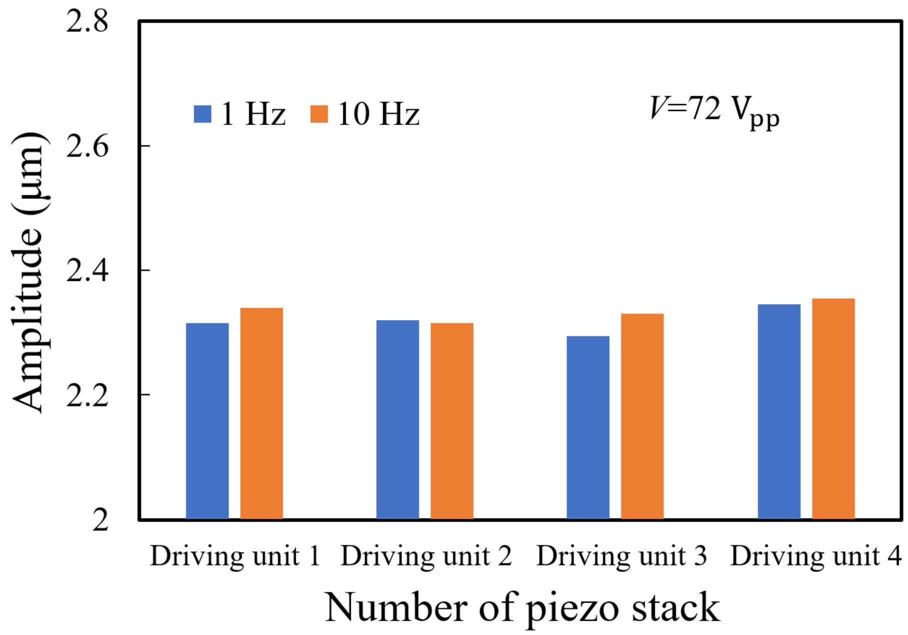

Fig. 5-8. Measured results of the amplitudes of 4 driving units under the frequencies of 1 and 10 Hz.

After finishing the assembly of the stator, the normal vibration amplitudes of the two driving feet on the stators were measured by using a laser displacement sensor to verify if the upper and lower stators have the same working performance, as shown in Fig. 5-9. The measured results demonstrate that the normal amplitudes of two driving feet are identical at a driving frequency of 1 Hz and a sinusoidal voltage of 72 V_{pp}, as depicted in Fig. 5-10. Thus, it is confirmed that this stator can be adopted in the single-side drive actuator.

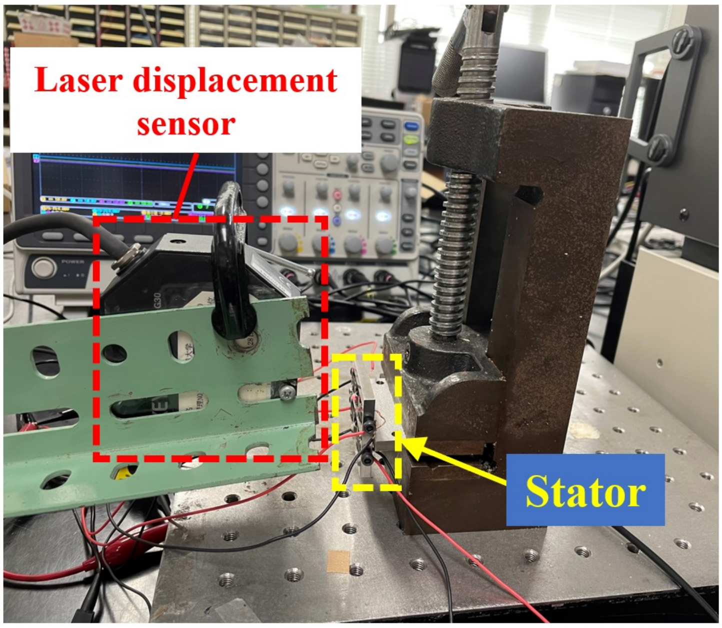

Fig. 5-9. Measurement system of normal vibration amplitude of two stators.

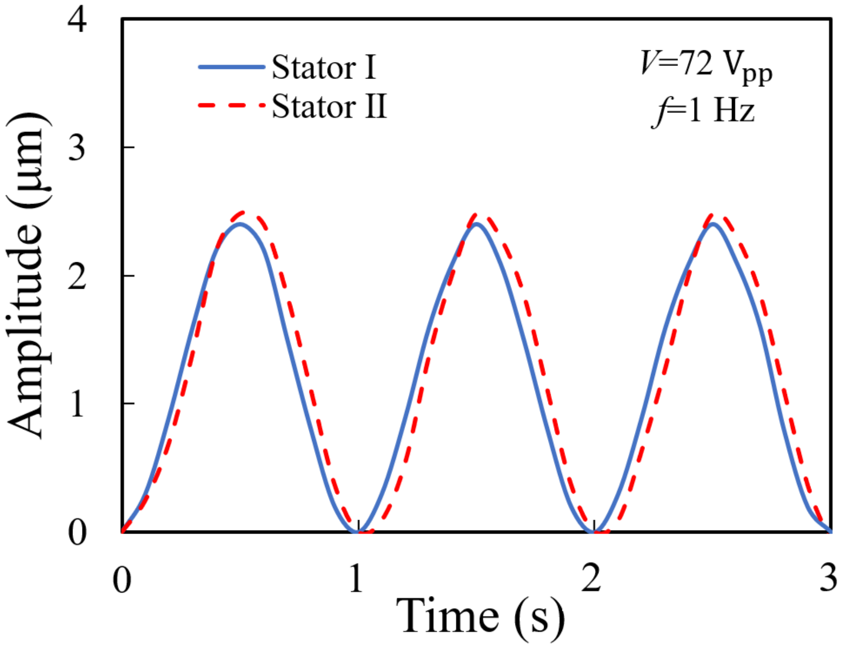

Fig. 5-10. Normal amplitudes of two driving feet at a driving frequency of 1 Hz and a voltage of 72 V_{pp}.

5.3.2 Experimental evaluation

The experimental setup is established to evaluate the output performance of the single-side drive actuator, as illustrated in Fig. 5-11. It consists of two power amplifiers (HSA 4012, NF Co.), two signal generators (WF1974, NF Co.), an oscilloscope (DCS-2204E, TEXIO), a laser displacement sensor (LK-G3000V, KEYENCE), and a force gauge (FGP-0.5, SHIMPO).

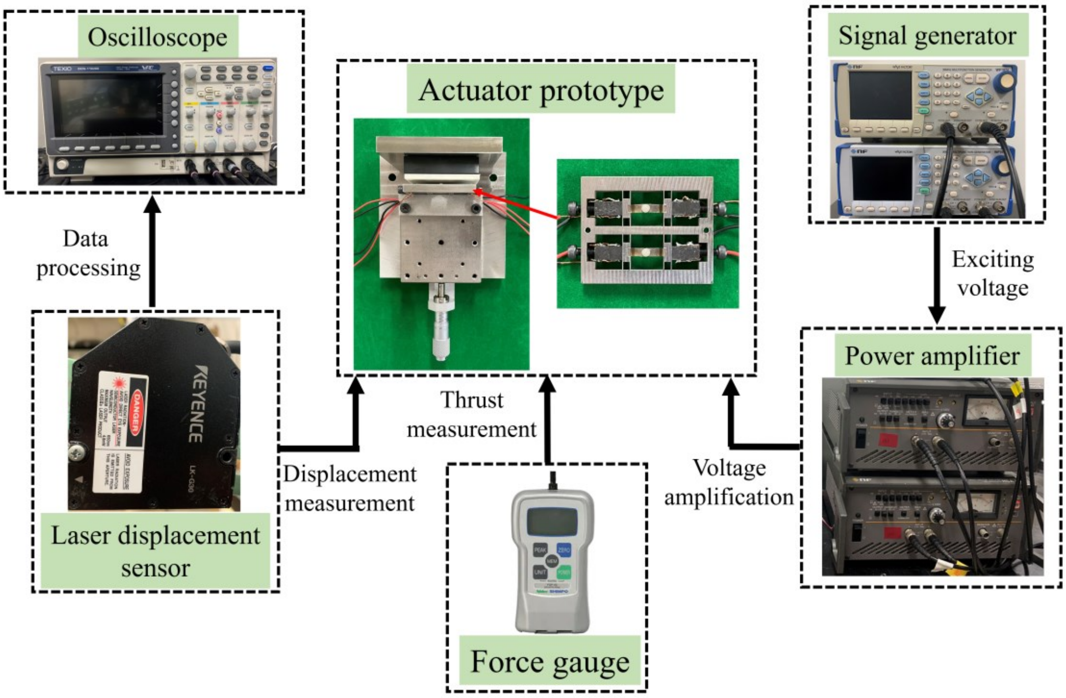

Fig. 5-11. Experimental setup.

5.3.2.1 Optimal preload test

In this study, the preload that corresponds to the maximum thrust is considered to be the optimal preload. Fig. 5-12 shows the relationship between the preload and thrust obtained in the experiment and simulation. The simulation results for the optimal preload at various voltages are slightly smaller than the experimental results, which is considered to be caused by the loss of preload when the micrometer head is being screwed during the experiment. At a driving frequency of 500 Hz, with increasing preload, the thrust of the proposed actuator initially increased and then decreased. Under driving voltages of 72, 84, and 96 V_{pp}, with corresponding offset voltages of 36, 42, and 48 V, respectively, a maximum thrust of 1.24, 1.5, and 1.74 N was achieved at a preload of 2.7, 2.85, and 3.3 N, respectively. Thus, the above preload values were selected as the optimal preload values for various voltages in subsequent experiments.

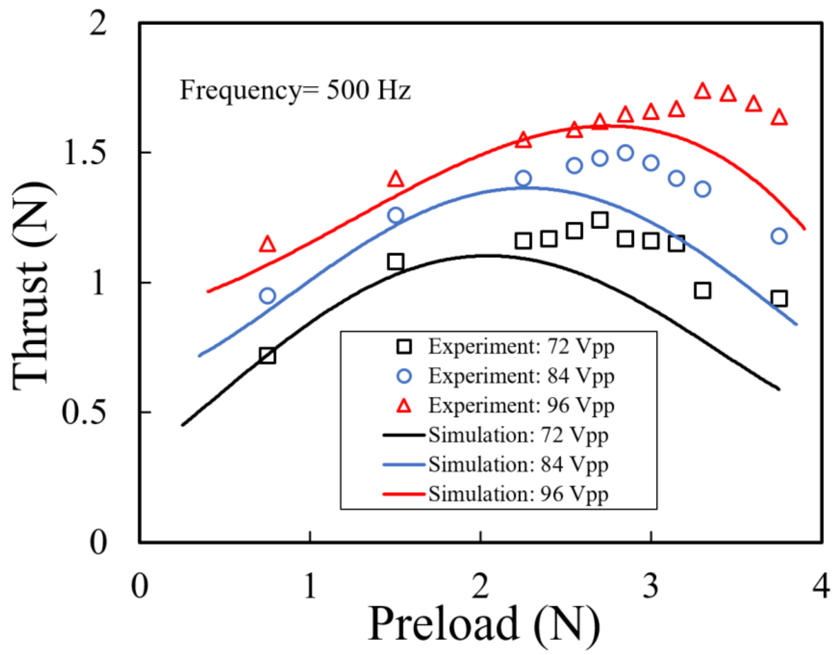

Fig. 5-12. Relationship between the preload and thrust.

5.3.2.2 Velocity characteristic

The single-side drive actuator can realize the macro linear motion when the driving frequency is over 100 Hz. First, we tested the velocity characteristics at frequencies in the range of 100-2000 Hz; the results are shown in Fig. 5-13. At a voltage of 96 V_{pp} and a preload of 3.3 N, the velocity of the actuator increased almost linearly from 0.42 to 8.7 mm/s when the driving frequency was increased from 100 to 2000 Hz. Moreover, a comparison was made between experimental and simulation results for velocity under the same driving conditions. The simulation curve is consistent with the trend of the experimental curve.

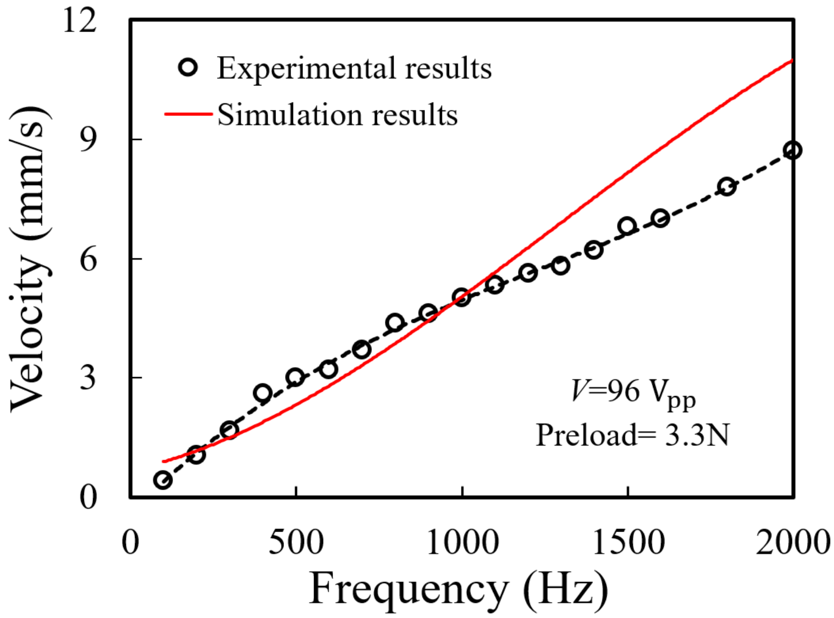

Fig. 5-13. Velocity characteristics for frequencies in range of 100-2000 Hz.

However, if the frequency exceeds 2 kHz, the input voltage cannot reach 96 V_{pp} due to the limitation of the power amplifier. Thus, a lower voltage was applied to ensure that the actuator could work under the same voltage in the evaluation of the velocity characteristics. Fig. 5-14 shows the velocity curve for frequencies in the range of 100-18000 Hz at a voltage of 36 V_{pp}. It can be seen that the velocity varied nonlinearly. At frequencies of 100-12000 Hz, the velocity initially increased from 100 to 11000 Hz. Theoretically, the output velocity could increase along with the driving frequency. However, the slip between the slider and driving feet is significant at high driving frequencies, decreasing one-step displacement. Thus, the velocity shows a decreasing trend in the frequency ranges of 11000-12000 Hz and 16000-18000 Hz. However, at frequencies of 12000-15000 Hz, there was a sudden increase in velocity. This can be considered to be caused by the resonance of the stator. Therefore, a modal analysis of the stator was carried out at a reference frequency of 14000 Hz; the results are shown in Fig. 5-15. Resonant modes appear at 13803 and 14367 Hz. This means that the stator may resonate around these two driving frequencies during the experiments, resulting in a sudden increase in speed. The velocities in the frequency range of 13800-14500 Hz were measured. A maximum velocity of 24.6 mm/s was achieved at a frequency of 14000 Hz.

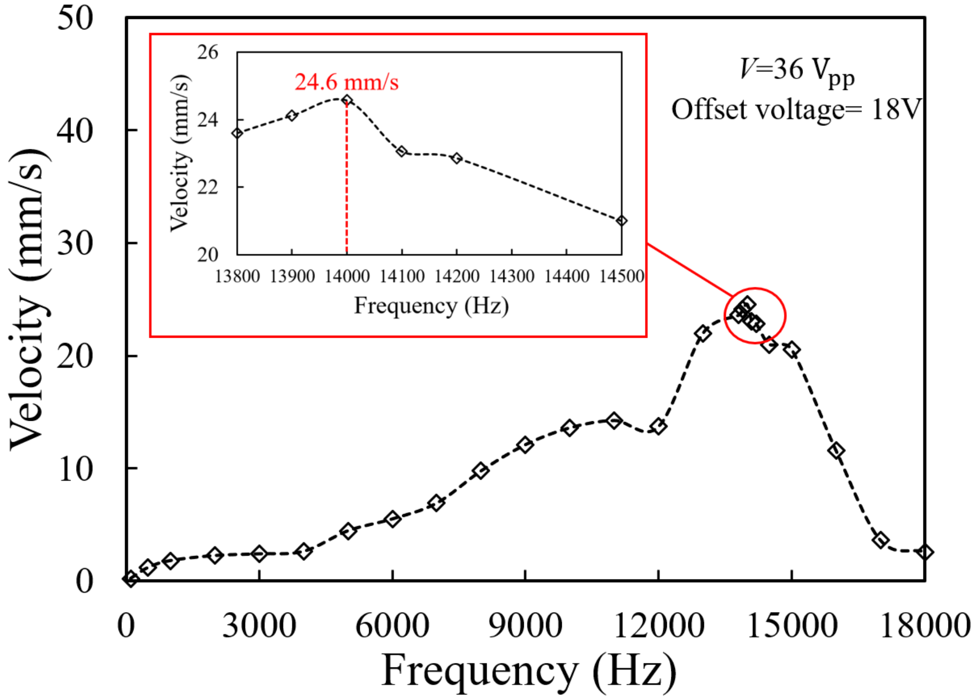

Fig. 5-14. Velocity characteristics for frequencies in range of 100-18000 Hz. Inset shows magnified view around 14000 Hz.

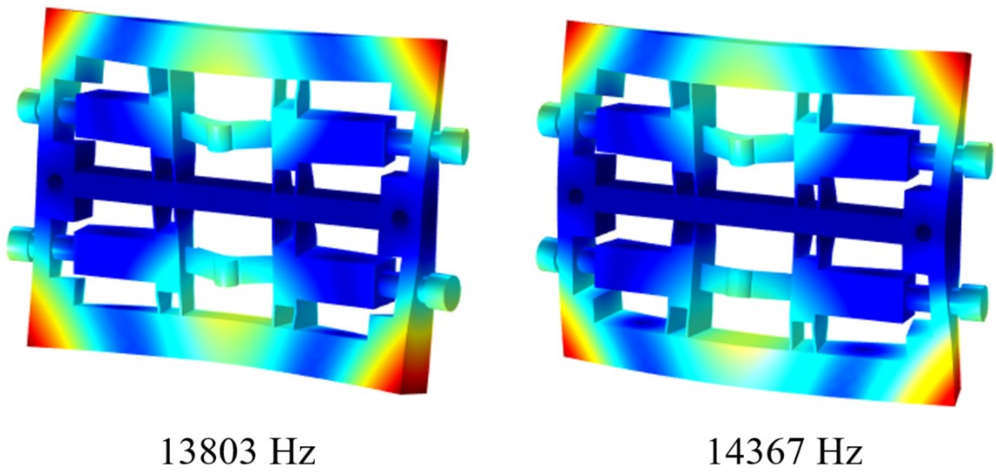

Fig. 5-15. Modal analysis of the stator.

The dead zone of the proposed actuator was measured at a frequency of 14000 Hz; the results are shown in Fig. 5-16. As the voltage increased, slider velocities under both in-phase drive (elliptical movements of the two driving feet without a phase difference) and opposite-phase drive (elliptical movements of the two driving feet with a half-cycle difference) increased, as shown in Fig. 5-16(a). The voltage region in which the actuator fails to function is called the dead zone. In this study, the measured dead zone for the in-phase and opposite-phase drives was 0-12 and 0-6 V_{pp}, respectively. The results show that the dead zone was reduced with the opposite-phase drive. In other words, the actuator was able to operate with a smaller normal acceleration of the driving foot with the opposite-phase drive. This is because when one driving foot drives the slider, the other can be effectively separated from the slider. Fig. 5-16(b) shows a comparison between the experimental and simulation results for the velocity and normal acceleration of the driving foot with the opposite-phase drive. The experimental values are higher than the simulation results. This was due to the resonance of the stator at a frequency of 14000 Hz during the experiment. In the future, the influence of resonance on the output characteristics of the actuator will be considered in the dynamic model.

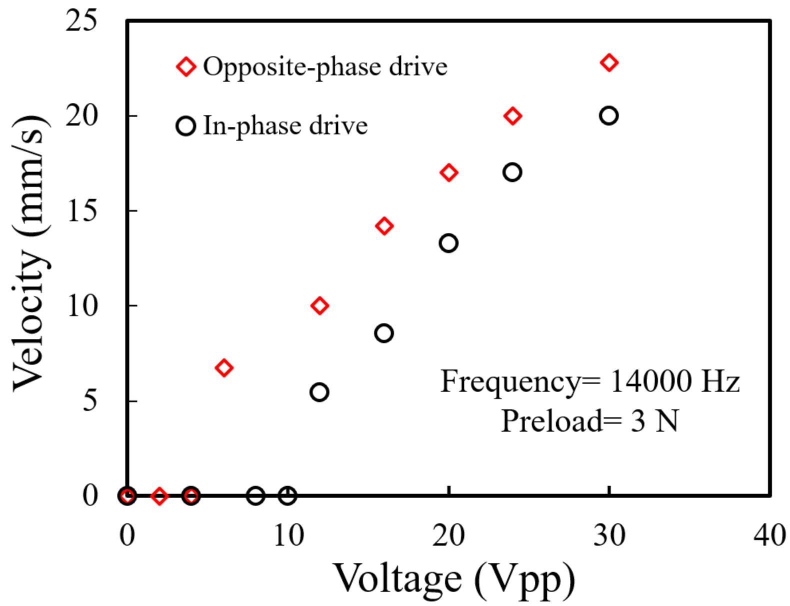

(a)

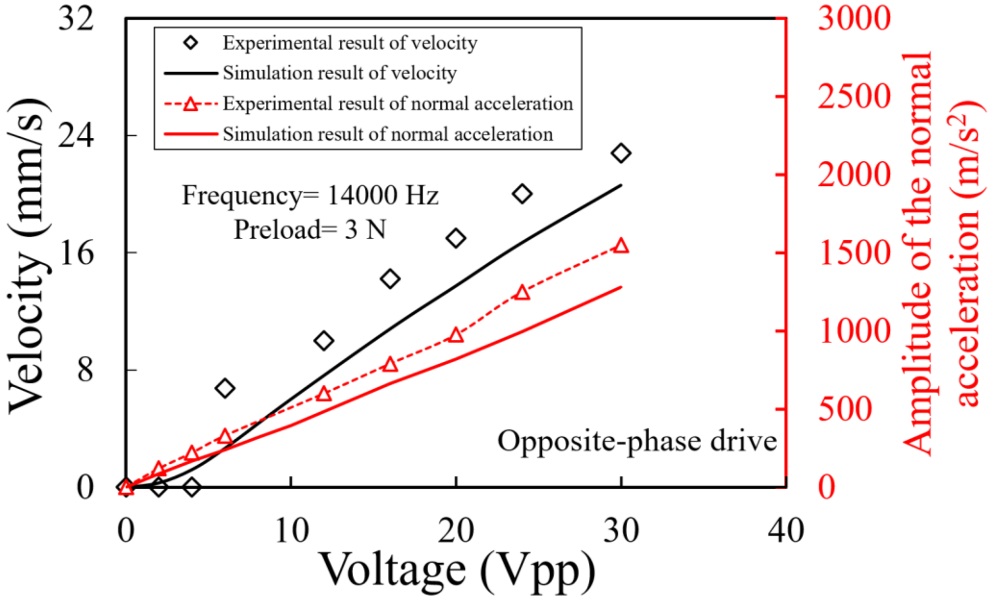

(b)

Fig. 5-16. (a) Dead zone of proposed actuator under in-phase and opposite-phase drives and (b) comparison between experimental and simulation results.

Further experiments were conducted on the dead zone using the opposite-phase drive at non-resonant frequencies; the results are shown in Fig. 5-17. Here, frequencies of 100, 500, 1000, 1500, and 2000 Hz were selected and a preload of 3 N was applied. Fig. 5-17(a) indicates that with increasing the voltage, both the normal acceleration and displacement of the driving foot increased. Moreover, at a given voltage, the normal displacement was almost independent of frequency, while the normal acceleration increased with increasing frequency. Fig. 5-17(b) shows the dead zone for various frequencies. The actuator had a small dead zone of 7.2 V_{pp} at non-resonant frequencies; the corresponding normal displacement of the driving foot in the dead zone was 0.12 μm. In addition, the measurement results of the corresponding normal acceleration indicate that the actuator works stably even under a low acceleration. Therefore, compared with the traditional single-stator motor, which cannot work or adjust velocity in the low-voltage region, the proposed actuator has the advantages of low-voltage operation and speed control.

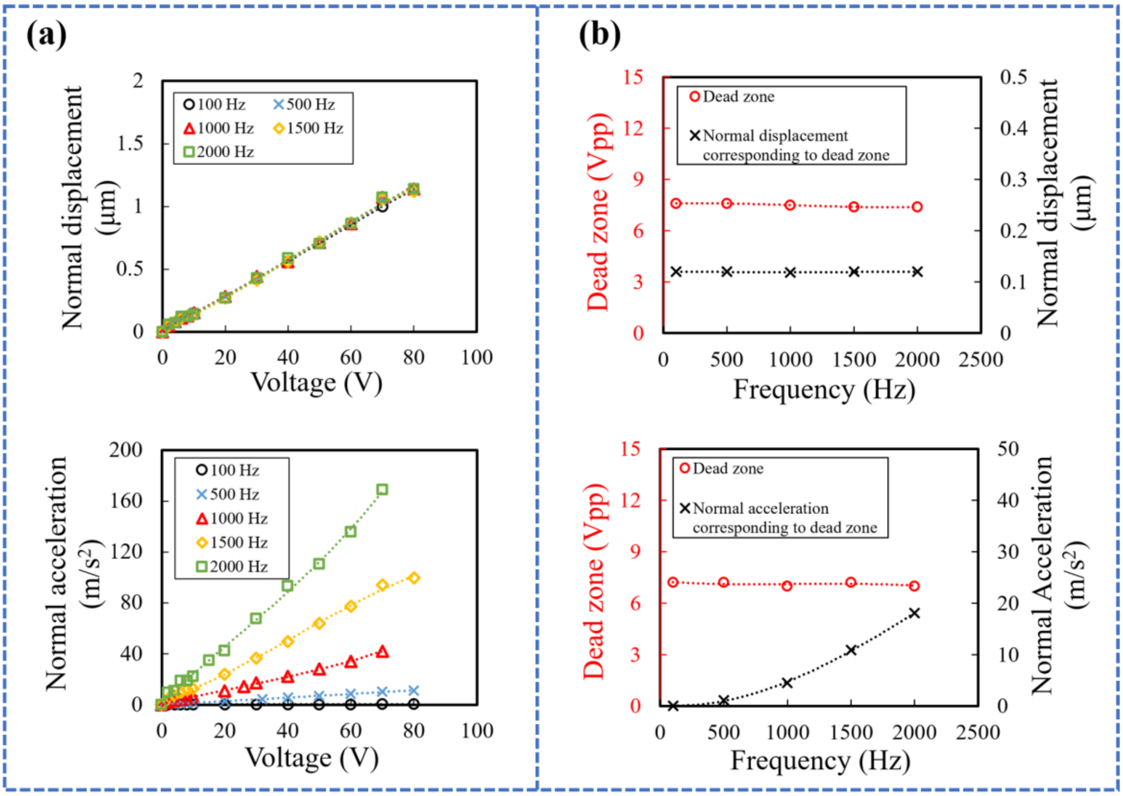

Fig. 5-17. (a) Normal accelerations and displacements of driving foot under various voltages and (b) dead zones under non-resonant frequencies.

5.3.2.3 Stepping characteristic

The micrometer step characteristics of the proposed actuator were tested and compared with the simulation results of the dynamic model; the results are shown in Fig. 5-18. The experimental results were in good agreement with the simulation results. Under a driving voltage of 72 V_{pp} and a frequency of 1 Hz, a step displacement of 2.25 μm was achieved. With increasing the driving voltage, the step displacement increased. With reference to Fig. 5-19, it can be seen that there was no backward displacement during the step process under the voltage of 72 V_{pp} and frequencies of 1, 2, and 5 Hz. This not only increases positioning accuracy and operation efficiency but also reduces wear.

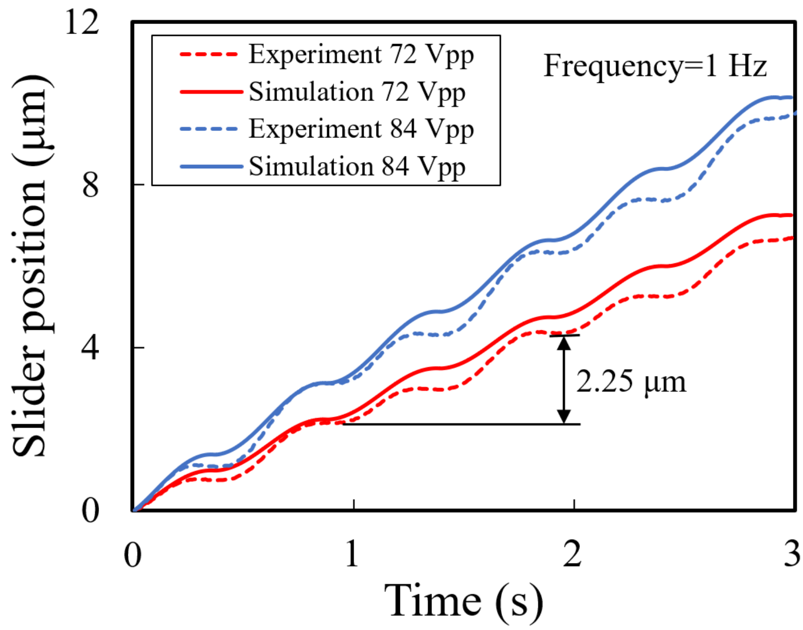

Fig. 5-18. Micrometer step characteristics of proposed actuator.

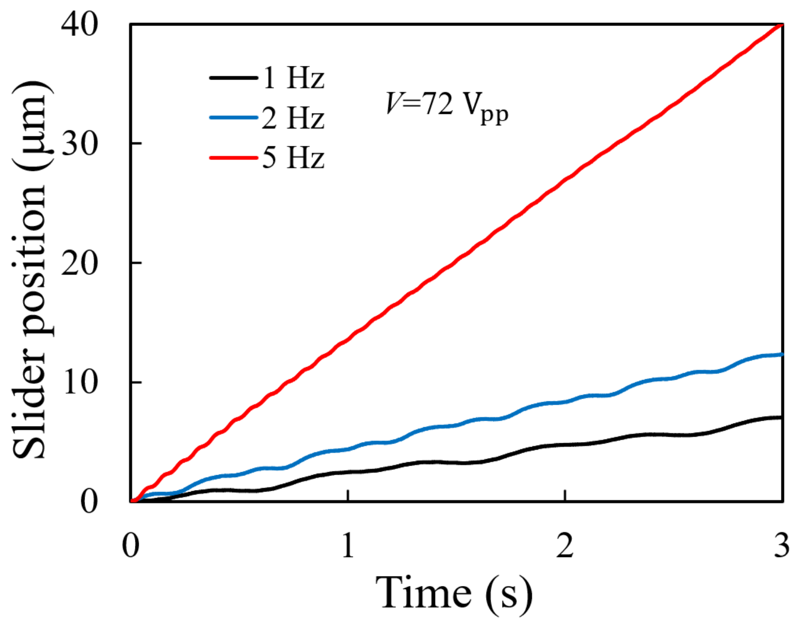

Fig. 5-19. Step curves at different frequencies.

5.3.2.4 Load characteristic

The load characteristics were measured when the single-side drive actuator was alternately driven by a dual stator. A comparison between the experimental and simulation results under the same driving conditions is shown in Fig. 5-20. Since a pulley was utilized to measure the load characteristics of the actuator during the experiment, there was mechanical loss associated with the pulley, which led to a discrepancy between the experimental and simulation results. Nevertheless, the proposed dynamic model effectively simulates the trend of the variations in the performance of the actuator.

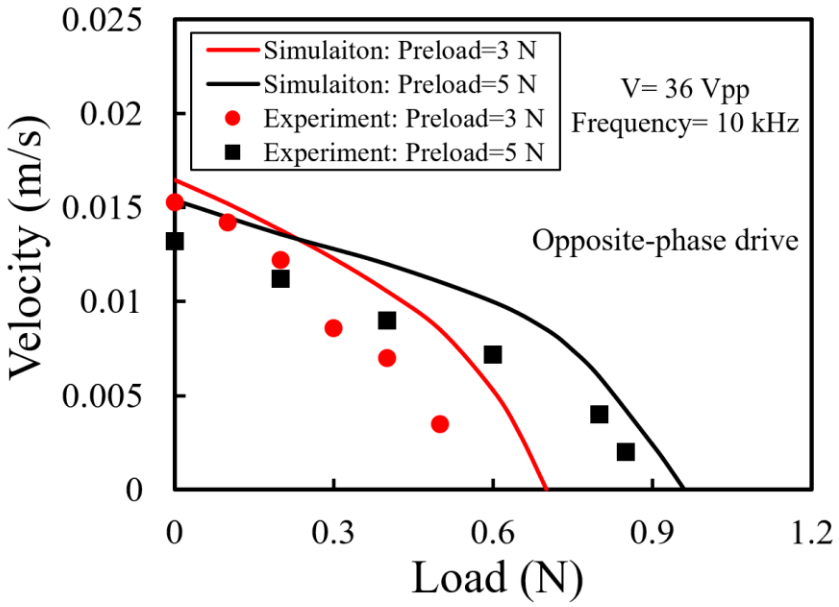

Fig. 5-20. Comparison between experimental and simulation results.

5.3.2.5 Precision positioning characteristic

To realize precision positioning, the step voltage signals V_1, V_3 (forward motion) and V_2, V_4 (reverse motion) shown in Fig. 5-21(a) were applied to the actuator. At each increasing stage of voltage, the slider can be pushed by the driving foot to move by a displacement d_1 due to the deformation of the triangular compliant mechanism, as shown in Fig. 5-21(b).

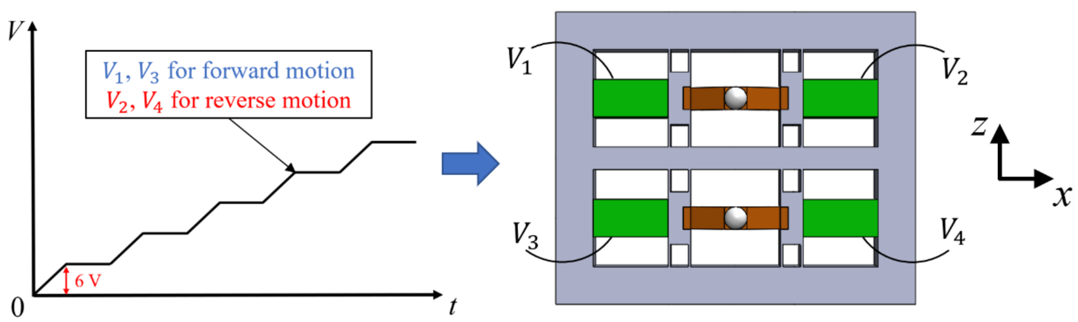

(a)

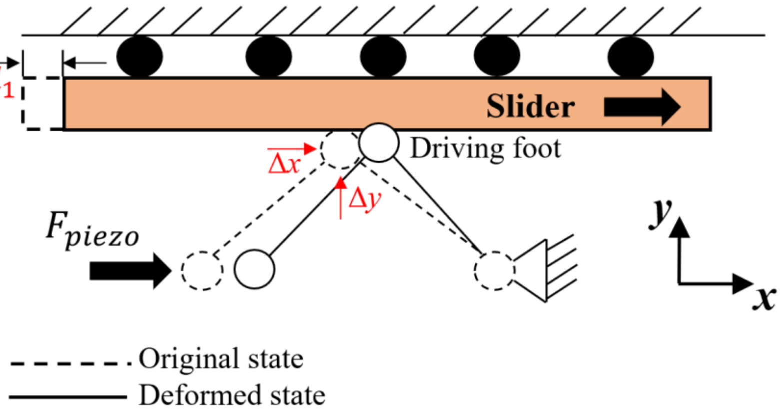

(b)

Fig. 5-21. (a) Voltage signal and (b) principle for precision positioning.

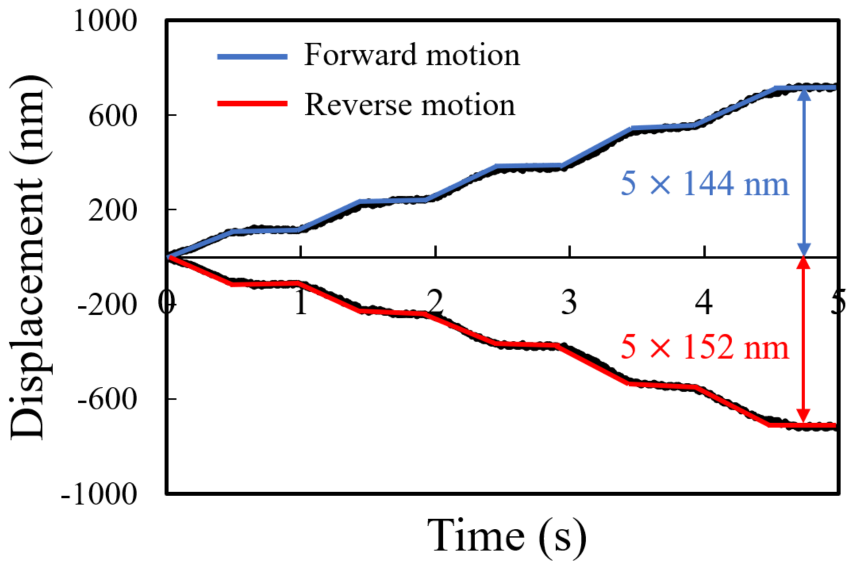

Fig. 5-22. Submicrometer positioning resolution of forward and reverse motions.

The experimental results show that the minimum step voltage that could move the slider was 6 V. Thus, the step displacement of the slider under a 6 V stepping voltage was regarded as the positioning resolution of the proposed actuator. As shown in Fig. 5-22, the positioning resolution of the forward and reverse motions was 144 and 152 nm, respectively. This indicates that the proposed actuator could realize submicrometer-scale positioning.

Repeatability is an important evaluation indicator for the precision positioning of an actuator. It can be obtained using the following steps: (1) repeat positioning from the same direction at any point to measure the stop position based on a target position; (2) find the maximum difference in the measured values. Repeatability is defined as ±1/2 of the maximum difference. In this study, the repeatability of the proposed actuator was tested based on the target positions 325, 425, 625, and 725 nm. The measurement results are shown in Fig. 22. For each target position, ten repeat positioning tests were carried out. The repeatability for the four target positions was ±25, ±35, ±40, and ±50 nm, respectively.

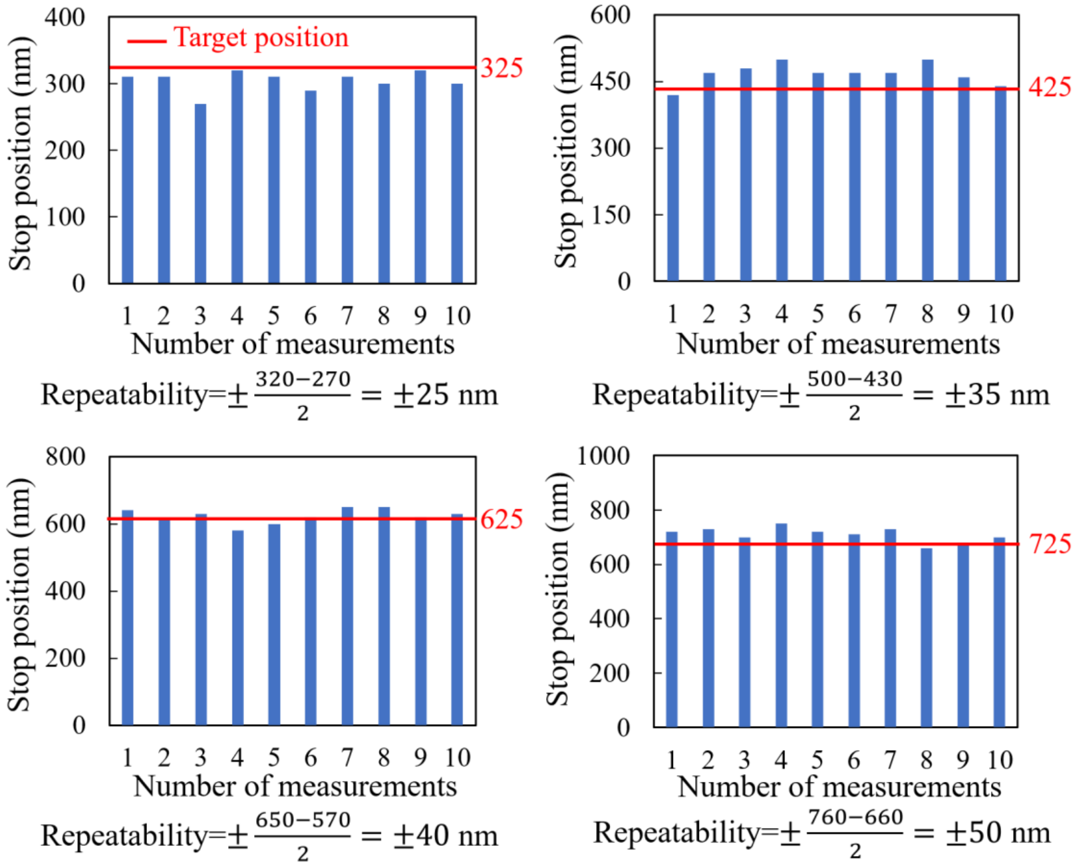

Fig. 5-23. Repeatability of the proposed actuator.

5.3.2.6 Performance comparison with previous study

To further validate the performance of the single-side drive actuator, a comparison was first made between the output characteristics of the single-side drive actuator and that of the dual-side drive actuator, as shown in Fig. 5-24. It can be seen that the single-side drive actuator effectively solved the backward motion problem that existed in the dual-side drive actuator. Mover, the single-side drive actuator shows better thrust, velocity, step displacement, and precision positioning characteristics.

Then, the performance of the single-side drive actuator was further compared with previously reported actuators with multiple driving units, as listed in Table 5-1. Compared with the previous actuators [85-88], the proposed actuator works under a wide range of driving frequencies and achieves a higher speed at a low driving voltage. Moreover, the positioning resolution of the proposed actuator is higher than the actuators [85, 87, 88]. Although a previously reported actuator [86] realized a positioning resolution of 110 nm, it exhibited backward motion, whereas the proposed actuator achieves step displacement without backward motion. The comparison results indicate that the proposed actuator has a wide operating velocity range, high speed, high positioning resolution, and no backward motion.

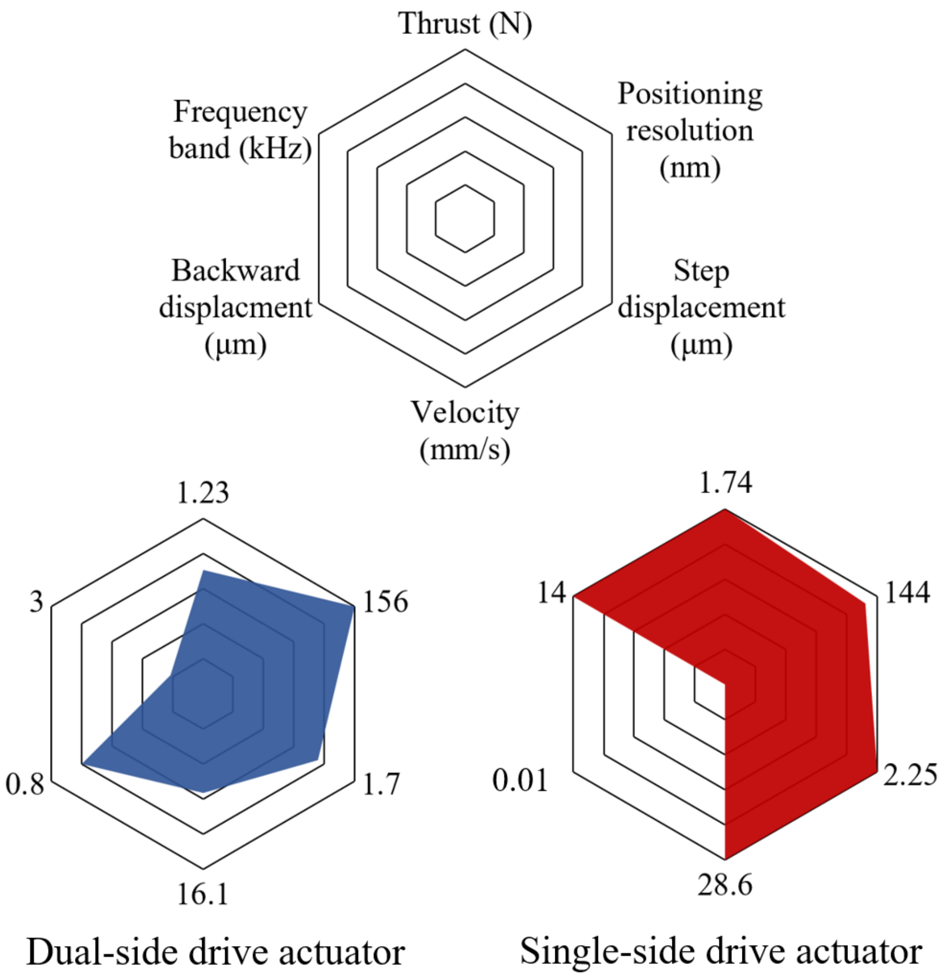

Fig. 5-24. Performance comparison between the single-side drive and dual-side drive actuator.

Table 5-1. Comparison between some previous actuators and this work.

Reference	[85]	[86]	[87]	[88]	This work
Driving voltage (V)	120	100	100	100	36
Frequency domain (Hz)	900	1200	6000	800	15 k
Maximum Speed (mm/s)	2.5	16.67	6	3.2	24.6
Resolution (nm)	158	110	170	290	144
Backward motion	with	with	with	with	without

5.4 Application

To verify the precision positioning performance of the proposed actuator, the movement of the slider was observed with a microscope. The observation method is shown in Fig. 5-25. An object was glued to the slider of the actuator and could move in the *x*-direction. A black dot with a diameter of 60 μm on the object was used to observe the position change of the object. A PC was used for imaging and recording.

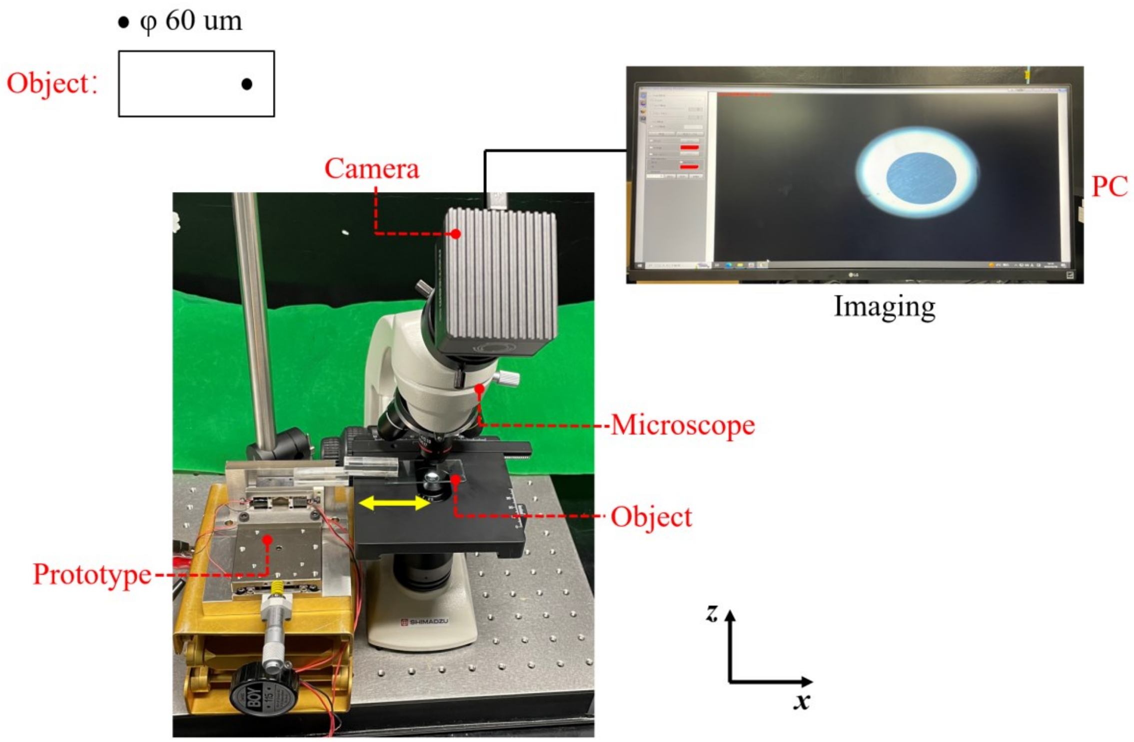

Fig. 5-25. Observation method for precision positioning of the actuator.

The observation results are shown in Fig. 5-26. We assumed that a target position was 50 μm away from the edge of the dot on the object. It can be seen that the dot reached the target position around 10 seconds after the actuator was started. This demonstrates that the proposed actuator can be used for precision positioning.

The actuator was flipped so that the object can be driven to move along in the *z*-direction for the optical focusing test, as shown in Fig. 5-27. The test results shown in Fig. 5-28 indicate that the proposed actuator is able to precisely drive the object to achieve a focus of the dot from blurred to clear.

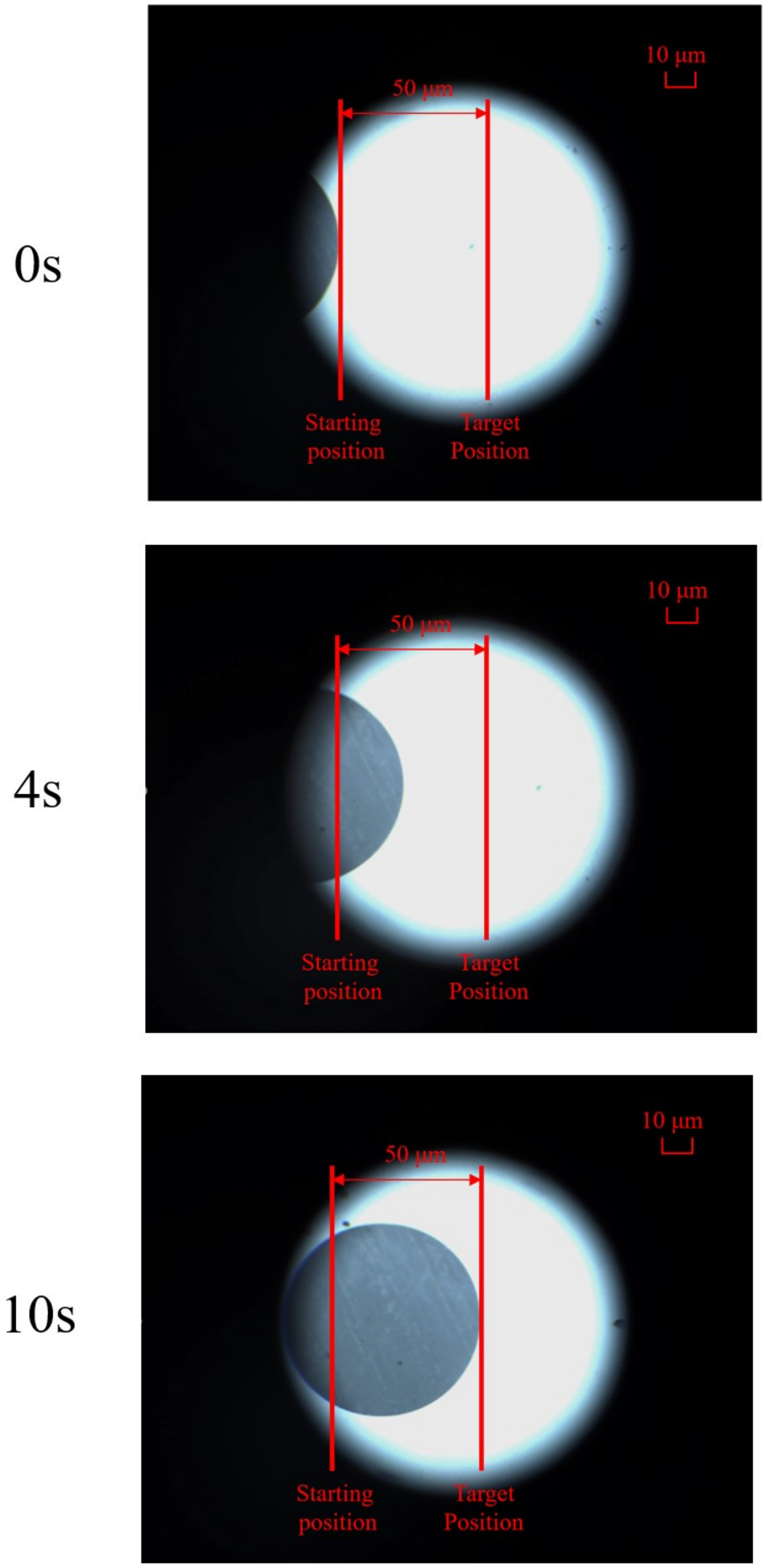

Fig. 5-26. Observation results.

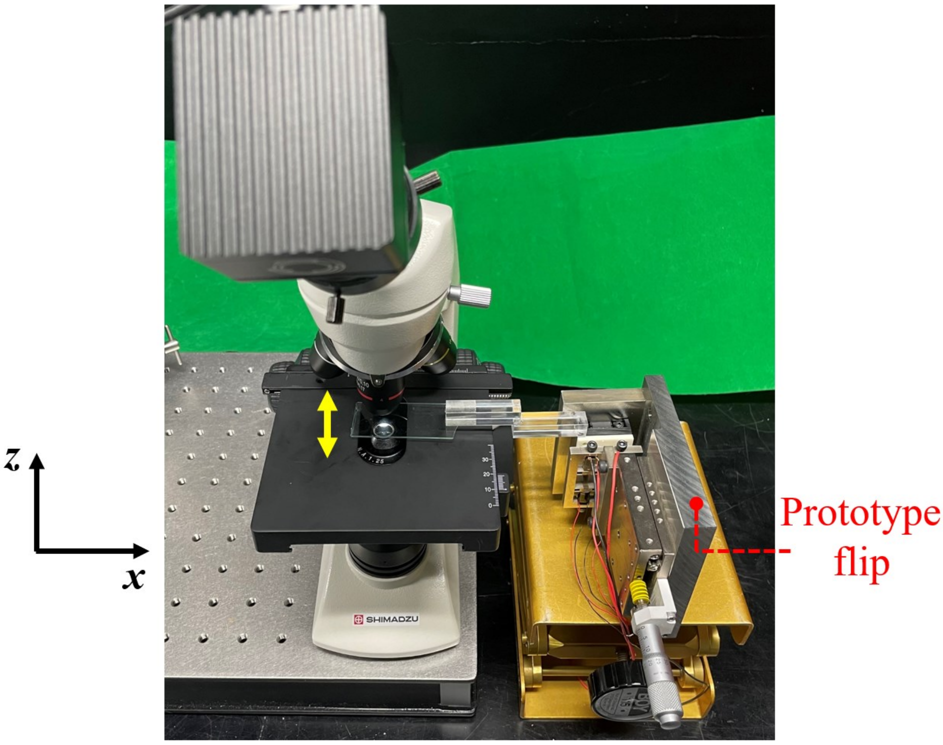

Fig. 5-27. Optical focusing test by the proposed actuator.

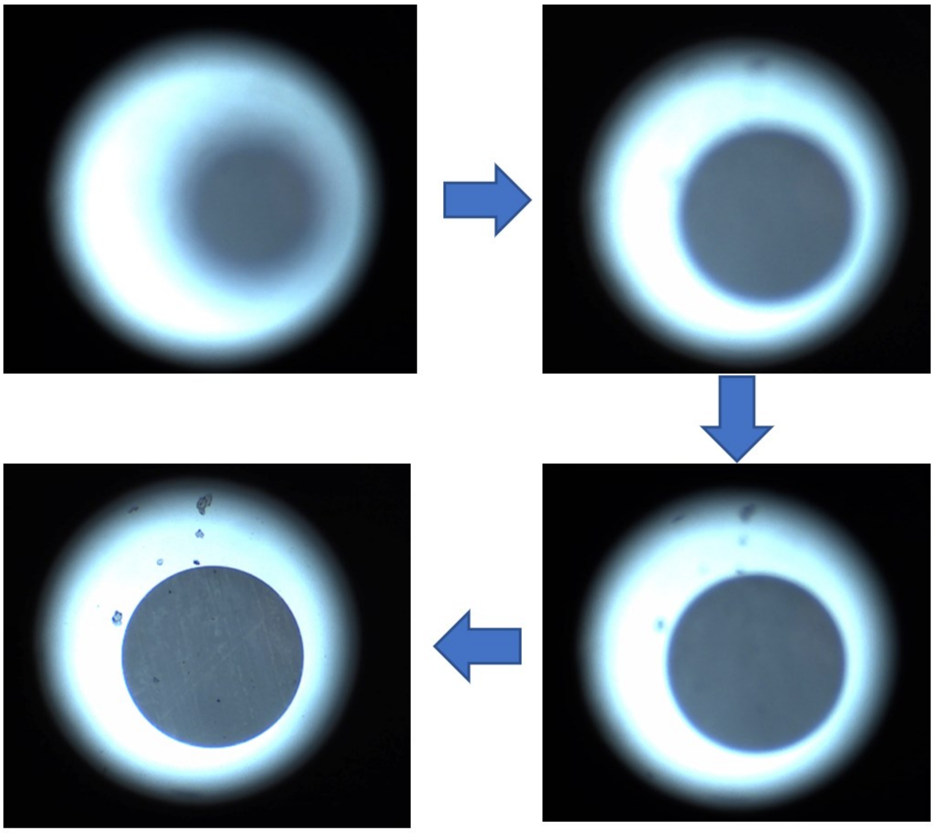
Fig. 5-28. Optical focusing test results.

Thus, the proposed actuator is suitable for being used in the precision positioning platform or optical system of the microscope after further optimization and miniaturization.

5.5 Dual-mode control strategy

The proposed actuator can be open-mode controlled for positioning applications by controlling the frequency and amplitude of the input sinusoidal voltage signals. However, the open-mode control is only suitable for micrometer-scale positioning. Thus, to improve the positioning accuracy, a dual-mode control strategy that combines the stepping and precision modes of the actuator is proposed, as shown in Fig. 5-29. We define x_t and x_m as the target position and measured position, respectively. Δd is the one-step displacement of the actuator. e represents the error between the target and measured position. u is the output value calculated by PI program. First, when the $|e|$ exceeds one-step displacement Δd, the actuator is electrified with sinusoidal voltage signals to achieve a step displacement. Under the stepping mode, if the $e > 0$, the target position is in front of the measured position. Four sinusoidal voltage signals $V_1 - V_4$ with 90° phase difference are applied to the stator to drive the slider forward. On the contrary, if $e < 0$, the target position is behind of measured position. In this case, sinusoidal voltage signals $V_1 - V_4$ with -90° phase difference are applied to drive the slider backward.

Then, as the slider approaches the target position within one cycle step displacement, the $|e|$ becomes less than Δd. The sinusoidal voltage signal is switched to a continuously increasing voltage signal controlled by the PI program automatically. The values for PI parameters are set to 10 and 10, respectively, after several attempts. The sign function of $'e'$ is used to determine which piezoelectric stacks will be excited. If $sign(e) = 1$, continuously increasing voltage signals V_1 and V_3 are applied to two piezo stacks on the left side of the stator for precision positioning in the forward direction until the slider reaches the target position. On the contrary, if $sign(e) = -1$, voltage signals V_2 and V_4 will be applied to two piezo stacks on the right side to position the slider backward.

In this study, a target position of 50 μm was selected for the precision positioning test, as shown in Fig. 5-30. The results indicate that the actuator can achieve positioning accuracy as high as 30 nm. The fluctuation in the target position can be considered to be caused by the vibration of the experimental setup.

Thus, the proposed actuator can realize large working stroke and high accuracy simultaneously with the dual-mode control strategy.

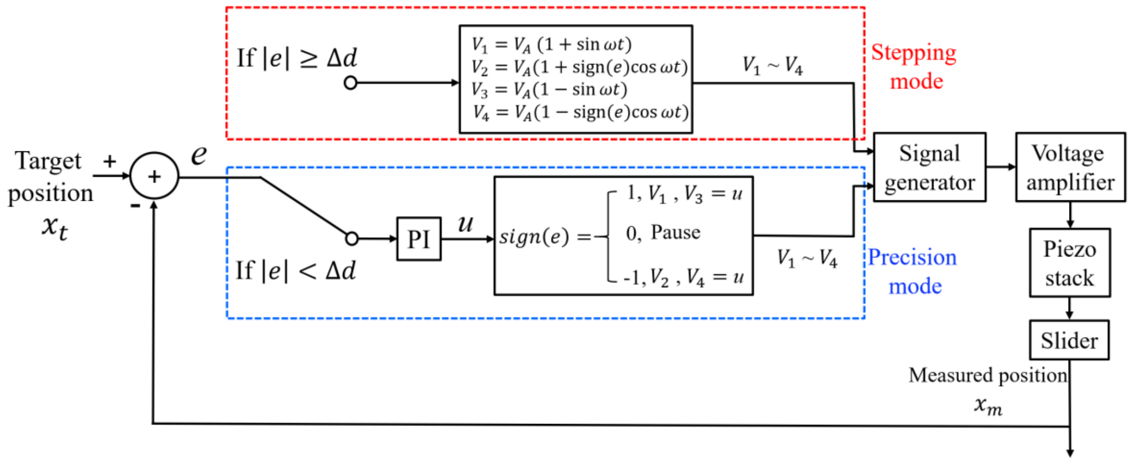

Fig. 5-29. Dual-mode control strategy.

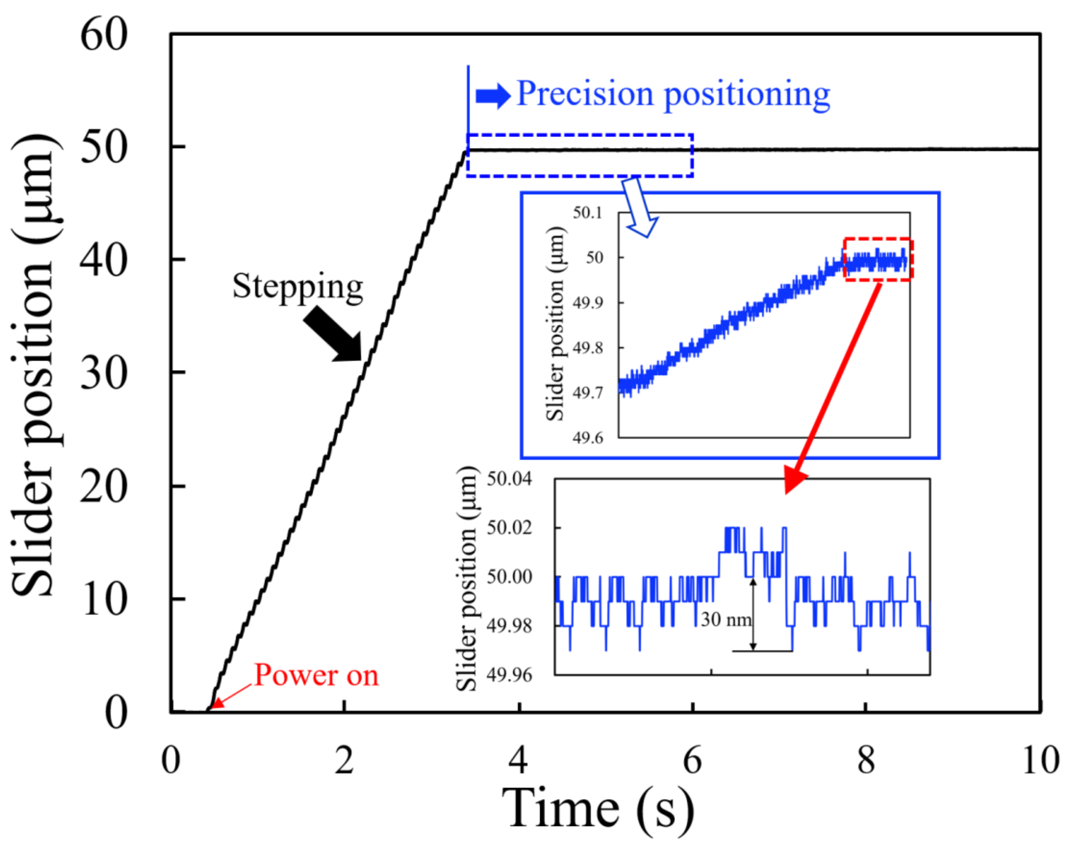

Fig. 5-30. Precision positioning test of 50 μm.

5.6 Conclusion

1. An actuator prototype was fabricated and experimentally evaluated. Experimental results indicate that the single-side drive actuator effectively eliminates the backward motion that existed in the both-side drive actuator. Under the opposite-phase drive, a wide range of velocity in the frequency range of 1-15000 Hz, a maximum velocity of 24.6 mm/s, a small dead zone of 0-6 V_{pp}, and a step displacement of 2.25 μm were achieved. Moreover, the proposed actuator demonstrates high-precision positioning, with resolutions of 144 and 152 nm in the forward and reverse directions, respectively. The actuator has a repeatability of ±25, ±35, ±40, and ±50 nm for strokes of 325, 425, 625, and 725 nm, respectively.

Thus, the single-side drive realizes superior multiple performances of a wide range of velocity, stepping without backward motion, and high-precise positioning, and it is promising for future applications in working scenarios such as scanning and optical system driving in SEM.

2. The experimental results were compared with the simulation results. They are in good agreement, demonstrating the feasibility of the proposed dynamic models in Chapter 4.

3. The precision positioning performance of the actuator was verified with a microscope.

4. A dual-mode control strategy that combines the stepping and precision modes was proposed to improve the positioning accuracy.

6. Conclusion

To meet the driving requirements of the objective lens in scanning electron microscopes used to monitor the lithography process in semiconductor manufacturing, two kinds of walking-type piezoelectric actuators were developed in this study. Working principles and structure design were explained in detail. Dynamic models were established and actuator porotypes were fabricated for the performance simulation and experimental evaluation.

6.1 Main works

1. A dual-side drive walking-type piezoelectric linear actuator with the parallel-arrangement dual stator was proposed. The operating principles and elliptical trajectory of the driving feet of a single-stator design were analyzed. A prototype was fabricated, and a series of experiments were tested to evaluate its output performance; the experimental results indicated that, under the alternate-drive mode, a no-load speed of 0.06 to 1.2 mm/s at driving frequencies of 10 to 500 Hz and a stepping displacement of 1.8 μm at 1 Hz were achieved. A maximum thrust of 7.3 N at 100 Hz and a maximum no-load speed of 16.1 mm/s at 3000 Hz were obtained. Moreover, the positioning resolutions of forward and reverse motions were 156 and 172 nm, respectively. However, this dual-side drive actuator has a complex structure and a serious backward motion and still needs to be improved.

2. To eliminate the backward motion of the dual-side drive actuator, a single-side drive stator structure with triangular-compliant mechanisms was further developed. Dynamic models in the *x*- and *y*-directions were established to evaluate the output characteristics of the single-side drive actuator when using dual stator alternating drive and single stator drive; the simulation results indicated that whether at low or high frequencies, the performance of the actuator is superior when alternately driven by dual stator than by a single stator. Specifically, the step displacement without backward motion at 1 Hz and a better load capacity at 10 kHz were realized when the actuator was driven alternately by the dual stator.

3. Prototype of the single-side drive actuator was fabricated and a series of experiments were carried out for comparison with simulation results. The feasibility of the dynamic

models was verified. Experimental results indicate that the single-side drive actuator effectively eliminates the backward motion that existed in the both-side drive actuator. A wide range of velocity in the frequency range of 1-15000 Hz, a maximum velocity of 24.6 mm/s, a small dead zone of 0-6 V_{pp}, and a step displacement of 2.25 μm were achieved. Moreover, the proposed actuator demonstrates high-precision positioning, with resolutions of 144 and 152 nm in the forward and reverse directions, respectively. The actuator has a repeatability of ±25, ±35, ±40, and ±50 nm for strokes of 325, 425, 625, and 725 nm, respectively.

Therefore, it is possible for driving the objective lens aperture plate in scanning electron microscopes.

6.2 Future works

1. The control system of the actuator will be further studied to reduce the positioning time.

2. The dynamic models will be improved for structural design, optimization, and simulation of the best driving conditions of the actuator.

3. The test equipment of the actuator proposed in this study are only for the experimental evaluation. They cannot yet be used in industrial applications. Thus, miniaturization and productization research of the actuator will be carried out.

Acknowledgement

Time flies, my doctoral career is coming to an end. Looking back on the past three years in the Ultrasonic System Laboratory of Muroran Institute of Technology, there are hardships and joys, and my heart is filled with many gratitude.

First and foremost, I would like to express my sincere gratitude to my supervisor, Professor Manabu Aoyagi for his guidance, support, and encouragement. Without the help and guidance of Prof. Aoyagi, I would not have been able to complete my doctoral research. Since I came to Muroran Institute of Technology as an exchange student in 2019, to the end of my three-year doctoral course, Prof. Aoyagi has helped me a lot both in my academic pursuits and daily life. His expertise, constructive criticism, and unwavering commitment to excellence have been invaluable to me.

I would like to express my gratitude to Assistant Professor Deqing Kong, who has provided me with so much helpful advice on my research and paper writing.

I'm extremely grateful to the members of my dissertation committee, Professor Hidekazu Kajiwara and Professor Kota Watanabe for their time, expertise, and thoughtful feedback. Their constructive comments and insightful suggestions have greatly improved the quality of my dissertation.

I would also like to thank the members of our lab who have helped me a lot in my research and life. In addition, I am very grateful to the Manufacturing and Engineering Design Center (cremo) of Muroran Institute of Technology for manufacturing the experimental equipment used in the research.

I would like to thank Dr. Kogi Kosaka and Mr. Takashi Ohe of TCK Inc. for supporting my research.

Thanks to Muroran Institute of Technology for providing me with the scholarship and to all staff of the Centre for International Relations for their support.

Last but not least, I would like to express my deepest appreciation to my family for their support and encouragement. Their love, understanding, and patience have sustained me through the past three years.

References

[1] Q. Michael, and S. Julian, Semiconductor manufacturing technology, Upper Saddle River, NJ: Prentice Hall. 2001.

[2] A. Elif, K. Nemoto, and R. Uzsoy, Cycle-time improvements for photolithography process in semiconductor manufacturing, IEEE Trans. Semicond. Manuf. 14 (1) (2001) 48-56.

[3] D.H. M. et al, Improving the accuracy of walking piezo motors, Rev. Sci. Instrum. 85 (5) (2014) 055007.

[4] J.K. Liu, Y.X. Liu, L.L. Zhao, and D.M. Xu, Design and experiments of a single-foot linear piezoelectric actuator operated in stepping mode, IEEE Trans. Ind. Electron. 65 (10) (2018) 8063-8071.

[5] C.X. Li, Y. Ding, G.Y. Gu, and L.M. Zhu, Damping control of piezo-actuated nanopositioning stages with recursive delayed position feedback. IEEE-ASME Trans. Mechatron. 22 (2) (2016) 855-864.

[6] D. Mazeika, G. Kulvietis, I. Tumasoniene, and R. Bansevicius, New cylindrical piezoelectric actuator based on traveling wave, Mech. Syst. Signal Proc. 36 (1) (2013) 127-135.

[7] L. Wang, W.S. Chen, J.K. Liu, J. Deng, and Y.X. Liu, A review of recent studies on non-resonant piezoelectric actuators, Mech. Syst. Signal Proc. 133 (2019) 106254.

[8] K. Uchino, Piezoelectric actuator renaissance, Energy Harvest Syst. 1 (1-2) (2014) 45–56.

[9] H Marth, B. Lula, Development of a compact high-load PZT-ceramic long-travel linear actuator with picometer resolution for active optical alignment application, Optomech Technol Astron. 6273 (2006) 493-497.

[10] P.B. Liu, Y. Peng, Ozbay Hitay. Design and trajectory tracking control of a piezoelectric nano-manipulator with actuator saturation, Mech. Syst. Signal Proc. 111 (2018) 529–44.

[11] W. Chen, X. Zhang, H. Li, J. Wei, and S. Fatikow, Nonlinear analysis and optimal design of a novel piezoelectric-driven compliant microgripper, Mech. Mach. Theory. 11 (2017) 32–52.

[12] F.J. Wang, C.M Liang, Y.L. Tian, X.Y. Zhao, and D.W. Zhang, Design and control of

a compliant microgripper with a large amplification ratio for high-speed micro manipulation, IEEE-ASME Trans. Mechatron. 21 (3) (2016) 1262–1271.

[13] Y.L. Tian, D. Zhang, B.J. Shirinzadeh, Dynamic modelling of a flexure-based mechanism for ultra-precision grinding operation, Precis Eng. 35 (4) (2011) 554–565.

[14] T. Morita, Miniature piezoelectric motors, Sens. Actuator A-Phys. 103 (3) (2003) 291-300.

[15] L. Wang, Y.X. Liu, K. Li, S. Chen, X.Q. Tian, Development of a resonant type piezoelectric stepping motor using longitudinal and bending hybrid bolt-clamped transducer, Sens. Actuator A-Phys. 285 (2019) 182-189.

[16] P. Hareesh, and D.L. DeVoe, Miniature bulk PZT traveling wave ultrasonic motors for low-speed high-torque rotary actuation, J. Microelectromech. Syst. 27 (3) (2018) 547-554.

[17] J. Deng, Y.X, Liu, W.S. Chen, H.P. Yu, A XY transporting and nanopositioning piezoelectric robot operated by leg rowing mechanism, IEEE-ASME Trans. Mechatron. 24 (1) (2019) 207-217.

[18] G.Y. Gu, et al, Modeling and control of piezo-actuated nanopositioning stages: A survey, IEEE Trans. Autom. Sci. Eng. 13 (1) (2014) 313-332.

[19] L. Wang, J.K. Liu, S. Chen, K. Li, and Y.X. Liu, Design and fabrication of a high-speed linear piezoelectric actuator with nanometer resolution using a cantilever transduce, Smart Mater. Struct. 28 (5) (2019) 055035.

[20] T. Sashida, Japanese Patent disclosure 58-148682, 1983.

[21] Z.P. Dong, M. Yang, Z.Q. Chen, L. Xu, F. Meng, and W.C. Ou, Design and performance analysis of a rotary traveling wave ultrasonic motor with double vibrators, Ultrasonics. 71 (2016) 134-141.

[22] W.S. Chen, Y.X. Liu, X.H. Yang, and J.K. Liu, Ring-type traveling wave ultrasonic motor using a radial bending mode, IEEE Trans. Ultrason. Ferroelectr. Freq. Control. 61 (1) (2014) 197-202.

[23] S. Ueha, Y. Tomikawa, M. Kurosawa, et al, Ultrasonic motors: theory and applications. USA: Oxford University Press; Clarendon Press, 1993.

[24] M. Kurosawa, S. Ueha, High speed ultrasonic linear motor with high transmission efficiency, Ultrasonics. 27 (1989) 39-44.

[25] K. Murai, D.Q. Kong, H. Tamura, and M. Aoyagi, Hollow cylindrical linear stator

vibrator using a traveling wave of longitudinal axisymmetric vibration mode, Ultrasonics. 129 (2023) 106910.
[26] M. kurosawa, M. Takahashi, and T. Higuchi, Ultrasonic Linear Motor Using Surface Acoustic Waves, IEEE Trans. Ultrason. Ferroelectr. Freq. Control. 43 (5) (1996) 901-906.
[27] Y. Tomikawa, T. Takano, and H. Umeda, Thin rotary and linear ultrasonic motors using a double-mode piezoelectric vibrator of the first longitudinal and second bending modes, Japanese Journal of Applied Physics. 31 (9S) (1992) 3073.
[28] Y.X Liu, et al, Development of a bi-directional standing wave linear piezoelectric actuator with four driving feet, Ultrasonics. 84 (2018) 81-86.
[29] Y. Jian, Z.Y. Yao, and V.V. Silberschmidt, Linear ultrasonic motor for absolute gravimeter, Ultrasonics. 77 (2017) 88-94.
[30] X. Li, Z.Y. Yao, and R.C. Wu, Modeling and analysis of stick-slip motion in a linear piezoelectric ultrasonic motor considering ultrasonic oscillation effect, Int. J. Mech. Sci. 107 (2016) 215-224.
[31] M.X. Ling, J.Y. Cao, Z. Jiang, M.H. Zeng and Q.S. Li, Optimal design of a piezo-actuated 2-DOF millimeter-range monolithic flexure mechanism with a pseudo-static model, Mech. Syst. Signal Proc. 115 (15) (2019) 120-131.
[32] H. Tang, and Y.M. Li, Development and active disturbance rejection control of a compliant micro-/nanopositioning piezostage with dual mode, IEEE Trans. Ind. Electron. 61 (3) (2013) 1475-1492.
[33] W. L. Zhu, et al, Design, modeling, analysis and testing of a novel piezo-actuated XY compliant mechanism for large workspace nano-positionin, Smart Mater. Struct. 25 (11) (2016) 115033.
[34] X.Q. Tian, B.R. Zhang, Y.X. Liu, S. Chen, and H.P. Yu, A novel U-shaped stepping linear piezoelectric actuator with two driving feet and low motion coupling: Design, modeling and experiments, Mech. Syst. Signal Proc. 124 (2019) 679-695.
[35] J.P. Li, H.W. Zhao, X.T. Qu, H. Qu, X.Q Zhou, Z.Q Fan, and H.S. Fu, Development of a compact 2-DOF precision piezoelectric positioning platform based on inchworm principle, Sens. Actuator A-Phys. 222 (2015) 87-95.
[36] T. Mohammad, and S.P. Salisbury, Design and assessment of a Z-axis precision positioning stage with centimeter range based on a piezoworm motor, IEEE-ASME Trans. Mechatron. 20 (5) (2014) 2021-2030.

[37] J.L. Ha, et al, Effects of frictional models on the dynamic response of the impact drive mechanism, J. Vib. Acoust.-Trans. 128 (1) (2006) 88-96.
[38] R.F. Fung, C.F. Han, and J.L. Ha, Dynamic responses of the impact drive mechanism modeled by the distributed parameter system, Appl. Math. Model. 32 (9) (2008) 1734-1743.
[39] M. Hunstig, T. Hemsel, and W. Sextro, Modelling the friction contact in an inertia motor, J. Intell. Mater. Syst. Struct. 24 (11) (2013) 1380-1391.
[40] H. Xia, et al, Simulation of motion interactions of a 2-DOF linear piezoelectric impact drive mechanism with a single friction interface, Applied Sciences. 8 (8) (2018) 1400.
[41] M. Boudaoud, T. Lu, S. Liang, R. Oubellil, and S. Régnier, A voltage/frequency modeling for a multi-dofs serial nanorobotic system based on piezoelectric inertial actuators, IEEE-ASME Trans. Mechatron. 23 (6) (2018) 2814-2824.
[42] Y. Zhang, Y. Peng, Z. Sun, and H. Yu, A novel stick–slip piezoelectric actuator based on a triangular compliant driving mechanism, IEEE Trans. Ind. Electron. 66 (7) (2018) 5374-5382.
[43] T.G. Cheng, M. He, H.T. Li, X.H. Lu, and H. Gao, A novel trapezoid-type stick–slip piezoelectric linear actuator using right circular flexure hinge mechanism. IEEE Trans. Ind. Electron. 64 (7) (2017) 5545-5552.
[44] Z.C. Huo, et al, A dual-driven high precision rotary platform based on stick-slip principle, IEEE-ASME Trans. Mechatron. 27 (5) (2021) 3053-3064.
[45] J.P. Li, et al, A walking type piezoelectric actuator based on the parasitic motion of obliquely assembled PZT stacks, Smart Mater. Struct. 30 (8) (2021) 085030.
[46] P.Z. Li, et al, Dynamic linear modeling, identification and precise control of a walking piezo-actuated stage, Mech. Syst. Signal Proc. 128 (2019) 141-152.
[47] https://www.physikinstrumente.com/en/technology/piezoelectric-drives/piezowalk-piezo-motors/.
[48] https://www.physikinstrumente.com/en/
[49] http://www.aml.t.u-tokyo.ac.jp/research/manipulator/manipulator_e.html. 2013.
[50] T. Tanikawa, and T. Arai, Development of a micro-manipulation system having a two-fingered micro-hand, IEEE Trans. Robot. Autom. 15 (1) (1999) 152-162.
[51] http://www.newscaletech.com/doc_downloads/CMU-Heartlander.

[52] http://www.piezo-tech.com/solution/
[53] Q.B. Lv, Z.Y. Yao, and X. Li, Contact analysis and experimental investigation of a linear ultrasonic motor, Ultrasonics, 81 (2017) 32-38.
[54] X.N. Li, Z.Y. Yao, and M.J. Yang, A novel large thrust-weight ratio V-shaped linear ultrasonic motor with a flexible joint, Rev. Sci. Instrum. 88 (6) (2017) 065003.
[55] Y.L. Shi, et al, A new type butterfly-shaped transducer linear ultrasonic motor, J. Intell. Mater. Syst. Struct. 22 (6) (2011) 567-575.
[56] L. Wang, W.S. Chen, J.K. Liu, J. Deng, and Y.X. Liu, A review of recent studies on non-resonant piezoelectric actuators, Mech. Syst. Signal Proc. 133 (2019) 106254.
[57] Design and computational optimization of a decoupled 2-DOF monolithic mechanism
[58] J.P. Li, H. Liu, and H.W. Zhao, A compact 2-DOF piezoelectric-driven platform based on "z-shaped" flexure hinges, Micromachines. 8 (8) (2017) 245.
[59] C.Tang, M.Y. Zhang, and G.H. Cao, Design and testing of a novel flexure-based 3-degree-of-freedom elliptical micro/nano-positioning motion stage, Adv. Mech. Eng. 9 (10) (2017) 1687814017725248.
[60] C.X. Li, et al, Design, analysis and testing of a parallel-kinematic high-bandwidth XY nanopositioning stage, Rev. Sci. Instrum. 84 (12) (2013) 125111.
[61] Q. Wang, and Q.Y. Lu, A simple, compact, and rigid piezoelectric step motor with large step size, Rev. Sci. Instrum. 80 (8) (2009) 085104.
[62] S.P. Wang, W.B. Rong, L.F. Wang, Z.C. Pei, and L.N. Sun, A novel inchworm type piezoelectric rotary actuator with large output torque: design, analysis and experimental performance, Precis. Eng. 51 (2018) 545-551.
[63] X.Y. Xue, X. Tian, D. Zhang, and X.D. Liu, Design of a piezo-driven inchworm flexure stage for precision positionin, Int. J. Appl. Electromagn. Mech. 50 (4) (2016) 569-581.
[64] L. Ma, J.Y. Xiao, S.S. Zhou, and L.N. Sun, A piezoelectric inchworm actuator of linear type using symmetrical lever amplification, Proceedings of the Institution of Mechanical Engineers, Part N: Journal of Nanoengineering and Nanosystems. 229 (4) (2014) 172-179.
[65] H.P. Yu, Y.X. Liu, J. Deng, S.J. Zhang, and W. Chen, A collaborative excitation method for piezoelectric stick-slip actuator to eliminate rollback and generate precise

smooth motion, Mech. Syst. Signal Proc. 170 (2022) 108815.
[66] J.P. Li, X.Q. Zhou, H.W. Zhao, M.K. Shao, N. Li, S.Z. Zhang, and Y.M. Du, Development of a novel parasitic-type piezoelectric actuator, IEEE-ASME Trans. Mechatron. 22 (1) (2016) 541-550.
[67] B.C. Shi, et al, Design of a rhombus-type stick-slip actuator with two driving modes for micropositioning, Mech. Syst. Signal Proc. 166 (2022) 108421.
[68] J.P. Li, et al, Design and experimental performances of a piezoelectric linear actuator by means of lateral motion, Smart Mater. Struct. 24 (6) (2015) 065007.
[69] C. Yoo, Semiconductor manufacturing technology, IBM J Res Dev. 26 (2015) 528–531.
[70] J. Le Flohic, F. Paccot, N. Bouton, and H. Chanal, Application of hybrid force/position control on parallel machine for mechanical test, Mechatronics. 49 (2018) 168-176.
[71] IEEE Standard definition of primary ferroelectric terms. 1985
[72] J.H. Zheng, et al, Heat generation in multilayer piezoelectric actuators, J. Am. Ceram. Soc. 79 (12) (1996) 3193-3198.
[73] M. Aoyagi, R. Nakayasu, and H. Kajiwara, Non-resonant type linear ultrasonic motor using multilayer piezoelectric actuators with parallel beams, Int J Autom Tech. 10 (2016) 557-563.
[74] H. Huang, Z. Xu, J.R. Wang, and J.S. Dong, A low frequency operation high speed stick-slip piezoelectric actuator achieved by using a L-shape flexure hinge, Smart Mater. Struct. 29 (6) (2020) 065007.
[75] J.P. Li, J.J. Cai, J.M. Wen, J.F. Yao, J.S. Huang, T. Zhao, and N. Wan, A walking type piezoelectric actuator with two umbrella-shaped flexure mechanisms, Smart Mater. Struct. 29 (8) (2020) 085014.
[76] J.P. Li, H. Huang, H.W. Zhao, A piezoelectric-driven linear actuator by means of coupling motion, IEEE Trans. Ind. Electron. 65 (3) (2017) 2458-2466.
[77] F. Qin, et al, Design and stepping characteristics of novel stick–slip piezo-driven linear actuator, Smart Mater. Struct. 28 (7) (2019) 075026.
[78] A. Altan, and, R. Hacıoğlu, Model predictive control of load transporting system on unmanned aerial vehicle (UAV), In Fifth international conference on advances in mechanical and robotics engineering. 2017.

[79] A. Altan, and R. Hacioğlu, Modeling of three-axis gimbal system on unmanned air vehicle (UAV) under external disturbances, In 2017 25th Signal Processing and Communications Applications Conference (SIU). 2017.
[80] A. Altan, and R. Hacioğlu, Hammerstein model performance of three axes gimbal system on unmanned aerial vehicle (UAV) for route tracking, In 2018 26th Signal Processing and Communications Applications Conference (SIU). 2018.
[81] J.P. Li, et al, Development of a novel parasitic-type piezoelectric actuator, IEEE-ASME Trans. Mechatron. 22 (1) (2016) 541-550.
[82] J.R. Wang, et al, Design, analysis, experiments and kinetic model of a high step efficiency piezoelectric actuator, Mechatronics, 59 (2019) 61-68.
[83] Y. Deng, G. Zhao, X.Y. Yi, and W.L. Xiao, Contact modeling and input-voltage-region based parametric identification for speed control of a standing wave linear ultrasonic motor, Sens. Actuator A-Phys. 295 (2019) 456-468.
[84] H. Yun, D.Q. Kong, and M. Aoyagi, Development of a multi-drive-mode piezoelectric linear actuator with parallel-arrangement dual stator, Precis. Eng. 77 (2022) 127-140.
[85] J.P. Li, L.D. He, J.J. Cai, Y.L. Hu, J.M. Wen, J.J. Ma, and N. Wan, A walking type piezoelectric actuator based on the parasitic motion of obliquely assembled PZT stacks, Smart Mater. Struct. 30 (8) (2021) 085030.
[86] H. Huang, Z. Xu, J.R. Wang, and J.S. Dong, A low frequency operation high speed stick-slip piezoelectric actuator achieved by using a L-shape flexure hinge, Smart Mater. Struct. 29 (6) (2020) 065007.
[87] J.P. Li, H. Huang, and H.W. Zhao, A piezoelectric-driven linear actuator by means of coupling motion, IEEE Trans. Ind. Electron. 65 (3) (2017) 2458-2466.
[88] M.X. Zhou, Z.Q. Fan, Z.C. Ma, H.W. Zhao, Y. Guo, K. Hong, and D. Wu, Design and experimental research of a novel stick-slip type piezoelectric actuator, Micromachines. 8 (5) (2017) 150.

Publications

1. Journals

[1] **Hao Yun**, Deqing Kong, and Manabu Aoyagi. Development of a multi-drive-mode piezoelectric linear actuator with parallel-arrangement dual stator. Precision Engineering, 2022, 77: 127-140.

[2] **Hao Yun**, and Manabu Aoyagi. Modeling and performance evaluation of piezoelectric actuator with triangular compliant mechanisms for wide-range speed driving and high-precision positioning. Precision Engineering. Major change.

2. International conference

[1] **Hao Yun**, Deqing Kong, and Manabu Aoyagi. Performance test and backward motion suppression of a walking type piezoelectric actuator. *The 19th International Conference on Precision Engineering (ICPE).* C049. (2022.11)

[2] **Hao Yun**, Deqing Kong, and Manabu Aoyagi. Modeling and experimental evaluation of the stepping characteristics in a walking-type piezoelectric actuator. *International Workshop on Piezoelectric Materials and Applications in Actuators 2022 (IWPMA 2022)*. 11006. (2022.10, Online)

[3] **Hao Yun**, Deqing Kong, and Manabu Aoyagi. A double-stator piezoelectric actuator with two driving modes: design and experiments. *International Workshop on Piezoelectric Materials and Applications in Actuators 2021 (IWPMA 2021)*. (2021.10, Online)

3. Domestic conference

[1] **Hao Yun**, Deqing Kong, and Manabu Aoyagi. Development of dual-stator piezoelectric actuator with multi-drive mode, 日本機械学会/第 34 回「電磁力関連のダイナミクス」シンポジウム . 11B1-4. (2022.5)

[2] **Hao Yun**, Deqing Kong, and Manabu Aoyagi. Piezoelectric actuator with comprehensive performance of high-speed and high-precision positioning, 2023 年度精密工学会春季大会学術講演会. E22. (2023.3)

[3] **Hao Yun**, Deqing Kong, and Manabu Aoyagi. Design and experimental evaluation of a piezoelectric actuator with a wide driving frequency domain and high positioning

resolution, 2023 年度春季日本音響学会研究発表会. 2-7-4. (2023.3)

4. Awards

[1] 2023 年度精密工学会春季大会学術講演会において研究奨励賞を受賞 (2023.3)

Appendix A

RSM usually includes three steps: (1) design and experiments (or FEM) (2) response surface modeling through regression (3) optimization [37-38].

In this paper, three variables, Diameter D, thickness L_5 of the hinges and the length L_3 in the range of 0.4-1.2 mm, 1-1.8 mm and 2.6-3.4 mm are selected for the optimization of the parallel compliant mechanism, as shown in table A.1. In Design-Expert 8.0.6, 17 groups of parallel compliant mechanism structures with different sizes of D, L_5, and L_3 are designed according to the Box-Behnken design (BBD), and the y-directional displacement y and maximum equivalent stress σ of designed structures are evaluated by FEM as the response results, as summarized in table A.2. Then, the quadratic regression models of y and σ relating the three variables were obtained by least squares analysis as follows:

$$\begin{aligned} y = {} & 20.82888 - 0.21563L_3 + 0.6975D - 14.26375L_5 - 0.54687L_3D \\ & + 0.67187L_3L_5 + 0.59375DL_5 - 0.19375{L_3}^2 - 0.89687D^2 \\ & + 2.66562{L_5}^2\,, \end{aligned} \tag{A.1}$$

$$\begin{aligned} \sigma = {} & 558.61 - 16.84375L_3 - 299.45D - 325.88125L_5 - 18.75L_3D \\ & - 5.46875L_3L_5 + 58.125DL_5 + 0.35938{L_3}^2 - 61.14063D^2 \\ & + 77.23437{L_5}^2. \end{aligned} \tag{A.2}$$

Analysis of variance (ANOVA) results of the quadratic regression models were given in tables A.3 and A.4. The associated Prob. > F value of two models is lower than 0.05 indicated that two models are statistically significant. Both Prob. > F value of the lack of fit is more than 0.05 (non-significant) investigated that the two models were valid for this study [39]. Therefore, the quadratic regression models of y and σ can be used for further optimization.

Table A.1. Factor and range selection for parallel compliant mechanism.

Factor	Range (mm)
Diameter D	0.4-1.2
Thickness L_5	1-1.8
Length L_3	2.6-3.4

Table A.2. Structure design of parallel compliant mechanism and response results.

Number	L_3 (mm)	D (mm)	L_5 (mm)	Response 1 y (μm)	Response 2 σ (MPa)
1	3.00	0.80	1.40	5.85	93
2	3.40	0.80	1.00	7.52	139
3	2.60	0.40	1.40	6.5	135
4	2.60	1.20	1.40	5.48	80
5	3.00	0.80	1.40	5.85	93
6	3.00	0.80	1.40	5.85	93
7	3.40	1.20	1.40	4.68	77
8	3.00	0.40	1.00	8.55	181
9	3.00	0.80	1.40	5.85	93
10	3.00	0.80	1.40	5.85	93
11	3.00	1.20	1.00	7.08	109
12	3.00	0.40	1.80	5	103
13	3.40	0.80	1.80	4.2	69.4
14	3.40	0.40	1.40	6.05	120
15	2.60	0.80	1.80	4.76	73.9
16	2.60	0.80	1.00	8.51	140
17	3.00	1.20	1.80	3.91	68.2

Table A.3 ANOVA analysis results of regression model of y.

Sources of variation	Sum of squares	Degree of freedom	Mean square	F-value	Probability > F
Model	28.76	9	3.2	581.59	<0.0001 (S)
Residual	0.038	7	5.494E-3		
Lack of fit	0.03	3	0.01	4.86	0.0804 (NS)
Pure error	8.28E-3	4	2.07E-3		

Table A.4 ANOVA analysis results of regression model of σ.

Sources of variation	Sum of squares	Degree of freedom	Mean square	F-value	Probability > F
Model	14902.78	9	1655.86	138.28	<0.0001 (S)
Residual	83.82	7	11.97		
Lack of fit	64.91	3	21.64	4.58	0.0879 (NS)
Pure error	18.91	4	4.73		

Based on the above regression models, we set the optimization criterion is to achieve y as large as possible and keep σ lower than permissible stress (136.7 MPa, two-thirds of the yield strength) meanwhile, as presented in table A.5. The optimized sizes and predicted values of y and σ can be obtained as illustrated in table A.6.

Table A.5. Optimization criterion of y and σ by regression models.

	Optimization criterion
y	Maximize
σ	In range of 0-136.7 MPa

Table A.6. Optimized results.

	L_3 (mm)	L_5 (mm)	D (mm)	y (μm)	σ (MPa)
Value	2.6	1	0.84	8.38	136